UNIVERSITÀ
DI PAVIA

Dipartimento di Fisica

Corso di laurea magistrale in Scienze fisiche

Transient Absorption Spectroscopy of ligand-coated $CsPbBr_3$ nanoparticle supracrystals

Tesi per la laurea di:
Antonio Emanuele Mazzarone

Relatore:
Prof. Giulia Fulvia Mancini

Correlatore:
Dott. Simone Restelli

Anno accademico 2023 – 2024

Transient Absorption Spectroscopy of ligand-coated $CsPbBr_3$ nanoparticle supracrystals

Antonio Emanuele Mazzarone

Abstract

This thesis focuses on the study of two-dimensional (2D) superlattices created by self-assembly of ligand-coated $CsPbBr_3$ nanoparticles (NPs). These nanoparticles are characterized by different core sizes: 9 nm and 15 nm and identical organic ligand capping agent: 2-Ammonioethyl (hydroxypolypropyleneglycolyl, Mn=725) phosphate (PPG-PEA). In these $CsPbBr_3$@PPG-PEA 2D supracrystals, mesoscale crystalline order is primarily affected by ligand-ligand and ligand-core interactions.

These systems offer a flexible approach to engineering novel functional materials with tailored *ad hoc* functional responses activated by light pulses, useful for applications in nanotechnology and materials science. From a fundamental standpoint, they exhibit collective optical and electronic properties, providing an exciting way to study collective phenomena in soft condensed matter systems. While significant progress has been made in tailoring functionality through NP size, shape and chemical composition, the link between microscopic electronic and lattice structure, and macroscopic physical properties is still unclear. This thesis work aims to address this challenge through the study of core-core, ligand-core interactions and supramolecular electron-phonon coupling in these systems. The investigation is conducted using Transient Absorption Spectroscopy (TAS), complemented by *at-equilibrium* characterization techniques of Photoluminescence (PL) and Raman spectroscopy. PL and Raman spectroscopy provide valuable insights into the electronic and vibrational properties in the ground state. TAS investigates the out-of-equilibrium dynamics of charge carriers following light-matter interaction.

In this thesis, I experimentally characterized the optical properties and photoinduced responses and observed that they are strongly influenced by both the heterogeneous morphological distribution and the core size of the fundamental NP units. TAS measurements show spectral shifts in the photoinduced response based on the packing arrangements of the NPs, offering initial insights into how heterogeneity and confinement effects play a crucial role in influencing carrier dynamics. Variations in core size affect the timescales of the photoinduced response, with significant changes in signal shape. As the system transitions from larger NPs to smaller ones, the decay constants slow down due to a reduction in the number of available phonons, and ultrafast excitonic effects disappear. These results provide valuable insights into the recovery processes of these systems back to the ground state, across timescales ranging from femtoseconds (fs) to nanoseconds (ns).

Photoluminescence (PL) and Raman spectroscopy results further support these findings, demonstrating a blue shift in photoluminescence emission as core size de-

creases, along with the detection of a longitudinal optical phonon at 18.5 meV, which helps to understand the mechanisms of carrier relaxation through the formation of phonon-activated polarons.

In the following pages of this thesis, I will first provide a general introduction and overview of the systems studied. Next, in Chapter 1, I shall present the state of the art in this field, highlighting key advancements and the remaining challenges in understanding the optical and electronic properties of these systems. In Chapter 2 I shall provide a detailed description of the samples under investigation and the experimental techniques used, with a particular focus on the experimental strategies adopted for their characterization. In Chapter 3, I shall discuss the data analysis and the main experimental results, followed by an in-depth discussion to critically analyze the data and explore the potential implications of the findings. Finally, in the conclusion and perspectives, I shall summarize the results and outline future directions for improving and continuing this research aimed to achieve a deeper understanding of the behaviour of these systems at the nano-to-meso scales.

Spettroscopia di Assorbimento Transiente di Supracristalli di Nanoparticelle di $CsPbBr_3$ Rivestite da Ligandi

Antonio Emanuele Mazzarone

Riassunto

Questa tesi si concentra sullo studio di supracristalli bidimensionali (2D) ottenuti mediante auto-assemblaggio di nanoparticelle (NP) di $CsPbBr_3$ rivestite con ligandi organici. Queste nanoparticelle sono caratterizzate da dimensioni del nucleo diverse: 9 nm e 15 nm, e lo stesso agente di capping organico: 2-etilammonio (idrossipolipropilenglicol, Mn=725) fosfato (PPG-PEA). In questi supracristalli bidimensionali di $CsPbBr_3$@PPG-PEA, l'ordine cristallino alla mesoscala è principalmente influenzato dalle interazioni ligando-ligando e ligando-nanoparticella.

Questi sistemi offrono un approccio flessibile per l'ingegnerizzazione di nuovi materiali funzionali con risposte funzionali *ad hoc*, attivate da impulsi luminosi, utili per applicazioni in nanotecnologia e scienza dei materiali. Dal punto di vista fondamentale, essi mostrano proprietà ottiche ed elettroniche collettive, offrendo una piattaforma interessante per studiare fenomeni collettivi in sistemi di materia soffice condensata. Sebbene siano stati fatti progressi significativi nel modulare la funzionalità attraverso dimensioni, forma e composizione chimica delle nanoparticelle, il collegamento tra struttura elettronica e reticolare e le proprietà fisiche macroscopiche è ancora poco chiaro. Questo lavoro di tesi si propone di affrontare questa sfida attraverso lo studio delle interazioni nanoparticella-nanoparticella, ligando-nanoparticella e dell'accoppiamento elettrone-fonone supramolecolare in questi sistemi.

L'indagine è condotta utilizzando la Spettroscopia di Assorbimento Transiente (TAS), integrata da tecniche di caratterizzazione all'equilibrio come la Fotoluminescenza (PL) e la spettroscopia Raman. La PL e la spettroscopia Raman forniscono informazioni sulle proprietà elettroniche e vibrazionali nello stato fondamentale, mentre la TAS indaga le dinamiche fuori dell'equilibrio dei portatori di carica a seguito dell'interazione radiazione-materia.

In questa tesi, ho caratterizzato sperimentalmente le proprietà ottiche e le risposte fotoindotte, osservando che esse sono fortemente influenzate sia dalla distribuzione morfologica eterogenea sia dalla dimensione delle nanoparticelle come singola subunit fondamentale. Le misure TAS mostrano spostamenti spettrali nella risposta fotoindotta in base agli arrangiamenti delle nanoparticelle, offrendo prime indicazioni su come eterogeneità ed effetti di confinamento giocano un ruolo cruciale nell'influenzare le dinamiche dei portatori. Le variazioni nella dimensione delle nanoparticelle influenzano le scale temporali della risposta fotoindotta, con cam-

biamenti significativi nella forma del segnale. Quando il sistema passa da nanoparticelle più grandi a quelle più piccole, le costanti di decadimento rallentano a causa della riduzione del numero di fononi disponibili, e gli effetti eccitonici ultraveloci scompaiono. Questi risultati forniscono preziose informazioni sui processi di recupero di questi sistemi verso lo stato fondamentale, su scale temporali che vanno dai femtosecondi (fs) ai nanosecondi (ns).

I risultati della fotoluminescenza (PL) e della spettroscopia Raman confermano ulteriormente questi risultati, mostrando uno spostamento verso il blu nell'emissione di fotoluminescenza a seguito della diminuzione delle dimensioni del nucleo, insieme alla rilevazione di un fonone ottico longitudinale a 18.5 meV, che aiuta a comprendere i meccanismi di rilassamento dei portatori attraverso la formazione di polaroni attivati dai fononi.

Nelle pagine seguenti di questa tesi, fornirò prima una introduzione generale e una panoramica dei sistemi studiati. Successivamente, nel Capitolo 1, presenterò lo stato dell'arte in questo campo, evidenziando i principali progressi e le sfide rimanenti nella comprensione delle proprietà ottiche ed elettroniche di questi sistemi. Nel Capitolo 2, offrirò una descrizione dettagliata dei campioni in esame e delle tecniche sperimentali utilizzate, con particolare attenzione alle strategie sperimentali adottate per la loro caratterizzazione. Nel Capitolo 3, discuterò l'analisi dei dati e i principali risultati sperimentali, seguiti da una discussione approfondita per analizzare criticamente i dati ed esplorare le possibili implicazioni delle scoperte. Infine, nelle conclusioni e prospettive, riassumerò i risultati e delineerò le future direzioni per migliorare e proseguire questa ricerca finalizzata a ottenere una comprensione più profonda del comportamento di questi sistemi su scala nano- e mesoscopica.

Contents

List of Acronyms

2D Two-Dimensional.

3D Three-Dimensional.

FWHM Full-Width Half Maximum.

GLA Global Lifetime Anlysis.

HC Hot Carrier.

LHP Lead Halide Perovskite.

LWD Long Working Distance.

NC Nanocrystal.

NP Nanoparticle.

PB Photobleach.

PIA Photoinduced Absorption.

PL Photoluminescence.

PLQY Photoluminescence Quantum Yield.

PPG-PEA 2-Ammonioethyl (hydroxypolypropyleneglycolyl, Mn=725) phosphate.

QC Quantum-confined.

SC Supracrystal.

TA Transient Absorption.

TAS Transient Absorption Spectroscopy.

TEM Transmission Electron Microscope.

Introduction

2D superlattices created by self-assembly of functionalized nanoparticles (NPs) and nanocrystals (NCs) offer an efficient and flexible route toward engineering materials, with functional responses that can be activated by external light triggers for realistic applications photocatalysis, photothermal therapy and optoelectronics. Access to NP/NC building blocks with precisely controlled size, shape and composition, and advances in synthetic control over inter-NP/NC coupling and ligand chemistry, have created a fertile opportunity towards programmable, bio-compatible, sustainable, cost-effective materials [1]. Heterogeneity plays a key role in the overall description of these systems, where macroscopic electronic, mechanical and thermal performances directly stem from structure-property relationships and order/disorder correlations at the nanoscale [2, 3]. The possibility to predictably tune structure-property relationships and light-activated functions in heterogeneous nanostructures paves the way to a revolutionary class of new functional photonic materials, where bottom-up synthetic routes lead to reconfigurable light-matter interactions across multiple spatial (nano-to-meso) and temporal (femtoseconds to nanoseconds) scales [4]. To date, however, the role of heterogeneity in energy conversion from light to energetic carriers, and then into lattice heating, still remains elusive. The missing information is: what is the interplay, in the light-activated dynamics, of ligand-ligand, ligand-core, and core-core interactions, at the nearest-neighbours and overall superlattice levels? How can we tailor intra- and inter-structural interactions to tune predictably light-triggered functional properties in hybrid superlattices? To address these open questions, new methods are required, capable of looking at ligands and core dynamics, in the same measurement and upon photo-excitation, with high spatio-temporal resolutions.

Perovskites are widely recognized for their unique optical and electronic properties, which make them particularly relevant for applications in areas such as optoelectronics, photovoltaics and light-emitting devices [5–7]. Over the years, it has been demonstrated that these properties can be enhanced and modified by tailoring a wide range of parameters, such as particle size and chemical functionalization [5, 6]. However, a key challenge that has emerged over the years is the inherent instability of perovskites, which has limited their application in technology due to their degradation caused by changes in surface chemistry. For years, numerous attempts have been made to find the right passivating chemical agents that could increase the stability of these materials while preserving their intriguing properties

[2]. The choice of the system under investigation in this thesis was motivated by recent demonstrations of $CsPbBr_3$ nanoparticles functionalized with 2-Ammonioethyl (hydroxypolypropyleneglycolyl, Mn=725) phosphate (PPG-PEA) organic ligands, which exhibit high levels of stability [2]. Moreover, they preserve excellent optical properties, such as photoluminescence quantum yields near unity, which are essential for their use in technological applications and materials science.

To date, perovskite systems have been extensively studied at the core level, and progress in this field has accelerated significantly with the use of new characterisation techniques such as pump-probe spectroscopy [8–10]. Indeed, knowledge about core chemical and physical properties is nowadays wide, but what happens when these systems are functionalised with organic ligands and assembled into larger structures? Pioneering works [11, 12] have demonstrated that pump-probe approaches can also be used to look at what happens outside the core. Specifically, it has been shown that the functional properties and structure-property relationships of ligand-coated nanoparticle supracrystals strongly depend on the degree of heterogeneity in these systems, which is influenced by the level of ligand interdigitation at the single nanoparticle scale. However, these studies have been mostly conducted on functionalized metallic nanoparticle supracrystals [11, 12]. Only in recent years, it has been shown that, even in perovskite cores, variations in ligands induce order/disorder correlations that can alter the heterogeneous morphological distribution of the supracrystal. This, in turn, affects functional properties such as electron-phonon coupling. To date, while this has been extensively demonstrated in metallic nanoparticle supracrystals, no studies have been conducted on the order/disorder dynamics and the role of heterogeneity in the functional properties of perovskite nanoparticles functionalized with organic ligands [11, 12].

This thesis aims to fill this gap, by studying two different samples of ligand-coated $CsPbBr_3$ nanoparticle supracrystals, where the capping ligand is PPG-PEA. The two samples differ in core size: respectively 15 nm, and 9 nm. Morphological pre-characterizations of the samples show a significant heterogeneous distribution within each sample, even with the same core size. Novel out-of-equilibrium characterization techniques such as Transient Absorption Spectroscopy (TAS), complemented by ground-state techniques like Raman and PL, were employed to explore both ground-state and out-equilibrium properties of $CsPbBr_3$@PPG-PEA superlattices, primarily focusing on the electronic and vibrational degrees of freedom.

Using a comparative measurement strategy, the effects of mesoscale heterogeneity and core-size reduction were investigated, with the aim of characterizing electron-phonon coupling as these two parameters vary.

Chapter 1

State of the Art

This chapter provides an overview of the current research landscape concerning nanostructured functional materials. In section 1.1, the discussion starts by discussing the broad class of functional materials and then narrows the field to hybrid colloidal Nanoparticles (NPs) in section 1.2. These represent one of the most interesting and versatile building blocks for the realization of self-assembled nanostructures, such as nanoparticle Supracrystal (SC)s. Among these, ligand-coated Lead Halide Perovskite (LHP) nanoparticles have emerged as materials of great interest due to their unique optical and electronic properties [6]. In section 1.3, a detailed review of the optical and structural properties of LHPs, both in bulk and at the nanoscale, will be provided. The chapter concludes by highlighting the knowledge gaps in the photophysics of self-assembled supracrystals of these systems and the need for new experimental techniques to address them.

1.1 Functional materials and self-assembly

Functional materials are a class of engineered materials with a target-oriented approach [13]. Their chemical composition, structure and physicochemical properties are selectively optimised to achieve the appropriate functionality for subsequent desired applications. By tailoring these properties, functional materials play a key role in advanced technologies, such as catalysts or catalytic supports for energy storage, electrodes in the semiconductor industry, applications in medicine, data storage and optoelectronics, including photovoltaic and light-emitting devices [1, 11, 13, 14]. Interest in functional materials has grown in recent years, as it was realized that organized structures can be spontaneously obtained from "building blocks" beyond the atomic and molecular scales. For example, just as atoms combine to form molecules with radically different properties as the atomic constituents vary, nanoparticles can create Supracrystals (SCs) through a process called "self-assembly" [1]. Self-assembly is the process by which individual components arrange themselves into an ordered structure [15]. This allows the concepts of bottom-up synthesis of functional materials to be expanded and generalized. It is therefore possible to achieve a hierarchical design for nanoparticleline solids that can be engineered at the level of

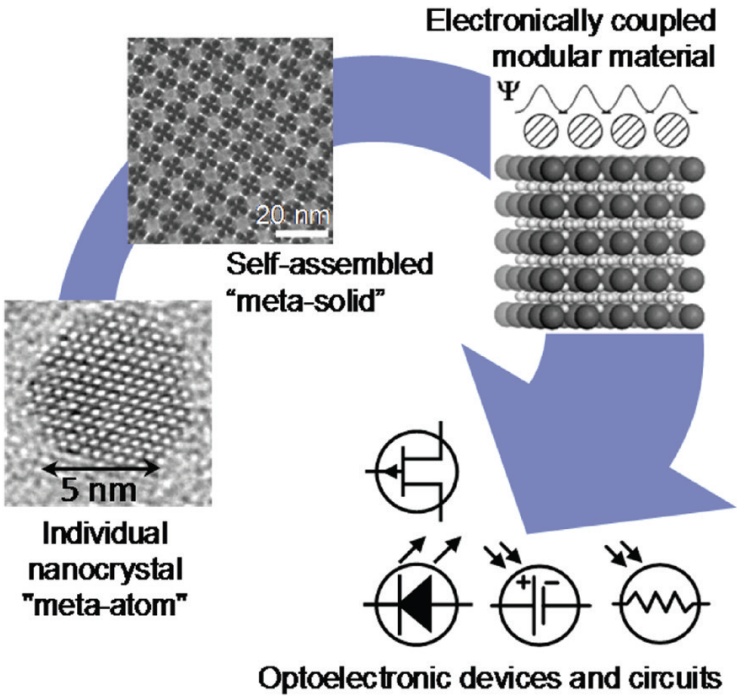

Figure 1.1: Self-assembly enables the transition from precisely engineered nanoscale building blocks to macroscopic functional materials used for devices and applications. Image adapted from [1].

individual nanoparticles and then self-assembled into superlattices with the structure of the crystalline solid. This gives a wide range of opportunities to develop new paradigms for chemistry and materials science, in which various nanometer-sized objects with engineered sizes, shapes, compositions, and properties serve as meta-atoms for hierarchically assembled functional materials and devices. Figure 1.1 shows the self-assembly transition as depicted by [1].

Several building blocks such as co-polymers, DNA, and opals [1] are known in nature to exhibit self-assembly. They can be classified according to the degree of complexity of the interactions governing the assembly, as shown in Figure 1.2, [1]. Self-assembly processes are normally described by theories of nucleation and growth, calling into play noncovalent interactions such as Van Der Waals forces, electrostatic and magnetic interactions, and hydrogen bonds [16]. For larger building blocks, interactions become more complex and classification is needed. The first category includes binary like-dislike interactions, such as those between hydrophobic and hydrophilic domains in a polymer backbone [17]. The next level of complexity occurs when building blocks have highly specific interactions. Biological examples such as DNA are known for their site-specific recognition, which is also found in metal-organic structures [18] and colloidal systems [19, 20]. Finally, ordered complex structures can form spontaneously without local attractive or repulsive forces. For example, hard colloidal spheres in concentrated solutions self-organize into long-range ordered domains due to entropy, forming a face-centred cubic crystal [15].

Colloidally synthesized inorganic NPs with organic capping ligands are among the

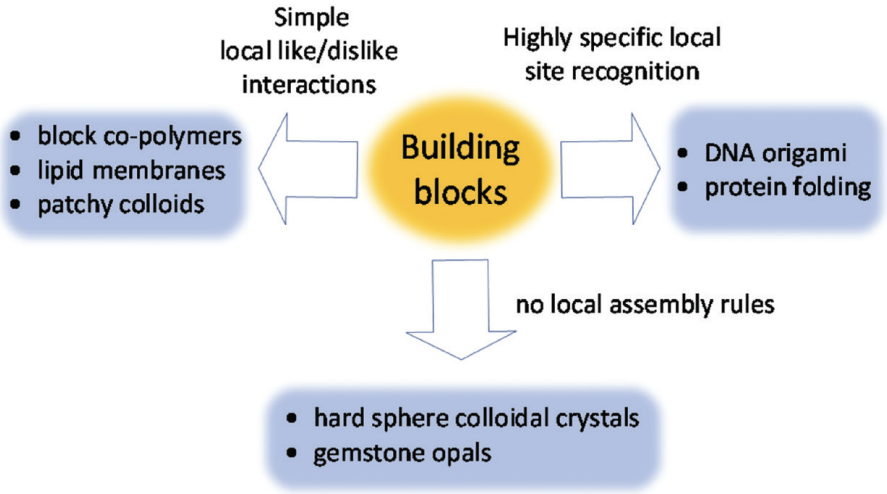

Figure 1.2: Classifications of interactions between building blocks utilized in self-assembly of functional materials. Image adapted from [1].

most important, interesting, and complex building blocks [15]. These systems are referred to as hybrid because they incorporate both hard components, represented by the individual NPs, and soft components, represented by the organic ligands. Hybrid colloidal NPs combine interactions typical of hard condensed matter systems [21], as well as those of soft condensed matter systems [17, 22–24]. This unique combination makes them promising materials, as they exploit the advantages of hard and soft components within a single material.

1.2 Hybrid Colloidal Nanoparticles

Colloidal NPs bridge the gap between molecules and bulk materials and enable researchers to probe the fundamentals of nanomaterials, surfaces, and size-dependent physics [25]. Most colloidal NPs consist of an inorganic core and an organic ligand shell, and we usually refer to them as hybrid colloidal NPs. Organic ligands are functional groups that bind to the nanoparticle core like a surfactant. As shown in Figure Figure 1.3, they consist of a group that binds to the nanoparticle surface, called the *head group*, while the rest of the ligand is referred to as the *tail group* [26–28]. The head groups are more strongly coupled to the nanoparticle and, being in direct contact with the inorganic surface atoms, are properly chosen for their influence on the electronic properties [25]. The tail groups have mainly weak interactions and entropic effects that offer significant power to control the stability and colloidal assembly. This contrast between strong and weak interactions is characteristic of nanoscale work in general. The strong interactions of the head group offer local-scale design control, while the many weak interactions of the tail group allow long-range design control [25]. Therefore, as functional materials, both the head group and tail groups of the capping ligand can be varied to achieve different objectives and a wide range of properties that result from the combination of interactions between individual components.

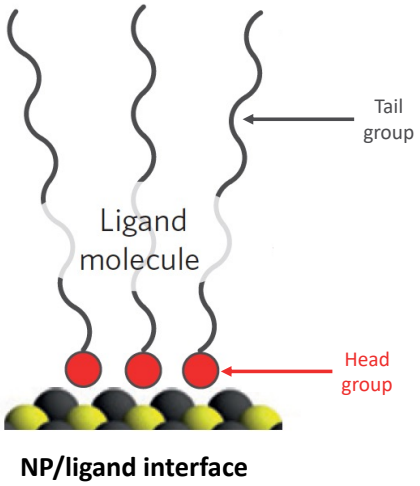

Figure 1.3: Schematic of NP/ligand interface. Black and yellow spheres represent NP surface while red spheres represent ligand headgroup atoms. Image adapted from [26].

The study of these interactions contributes to the conceptualization of new NPs syntheses, as they affect the surface energy of the colloid. These interactions also influence the subsequent assembly strategies used to create nanoparticle superlattices driven by interparticle forces. In general, ligand-ligand interactions influence the morphological, thermodynamic, and kinetic properties of NPs, as well as modify their colloidal stability. For this reason, they have found a variety of applications, from quantum dot emitters in displays [29, 30] to photovoltaics [31, 32]. In addition to this, their colloidal nature also allows them to be dispersed in solvents for optical studies, which include both single-particle measurements [33, 34] and the creation of assemblies of these materials to study collective effects, using them as artificial atoms [35, 36].

Colloidal Size and Shape control

The tail groups in the ligand shell also play a critical role during the synthesis process of colloidal NPs. When a nanoparticle cluster is formed, the organic tails face outwards, and for the cluster to grow, other monomers must be able to reach the nanoparticle surface. Therefore, if longer organic tails create a greater steric hindrance, they will reduce the diffusion rate of monomers towards the surface, resulting in generally smaller NPs [37]. The length of the ligand is the controlling parameter on nanoparticle size, as it alters the diffusion coefficient and solubility of the monomers [37]. Although it is now well-established that longer chains produce smaller NPs [25], the impact on the overall size distribution is less well-known. In addition to size distribution, the structure of the organic ligand can also affect shape distribution, as short-chain ligands, having a smaller steric size, allow for faster nucleation and growth due to the easier diffusion of monomers in solution and through the ligand shell. It is now known that in lead bromide and caesium halide NPs, the size of the cubic structure can be controlled by varying the chain length of the ligand used in the synthesis [25, 38].

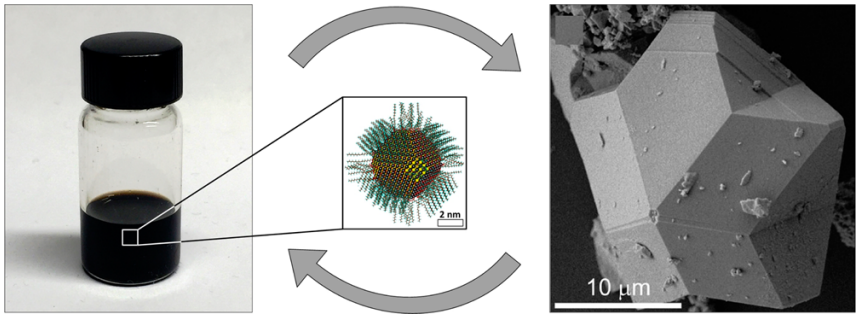

Figure 1.4: Self-assembly of colloidal NPs. Individual nanoparticle building blocks (left) are integrated into ordered arrays, or superlattices (right) by the process of self-assembly. These superlattices, held together by weak forces, can be disassembled into their constituent nanoparticles upon exposure to solvent. Shown here: 7-nm-diameter PbS NPs capped with oleic acid surface ligands self-assemble into a close-packed superlattice array. Image adapted from [15].

Colloidal Nanoparticle self-assembly into supramolecular systems

An ensemble of colloidal NPs can be induced to self-assemble into an ordered nanostructure by, for example, evaporation of carrier solvent [15]. As shown in Figure 1.4, this transition moves a collection of particles from a dilute state to one in which they are in contact with their nearest neighbours. To study the mechanisms of self-assembly, it is therefore crucial to consider the various contributions to nanoparticle-nanoparticle interactions during this process. These interactions, generally governed by non-covalent forces such as Van der Waals forces, electrostatic interactions and hydrogen bonds [16], form the basis of the description of self-assembly at equilibrium via nucleation and growth theories [15]. However, as discussed in section 1.1, these interactions become more complex for larger building blocks, such as functionalised colloidal nanoparticles, necessitating a classification based on interaction complexity.

The self-assembly of unfunctionalized nanoparticles is often described using the hard-sphere model, which assumes no attractive interparticle forces. At high-volume fractions, the disordered packing during the assembly process leads to a loss of translational entropy. As a result, even without favourable interactions, it becomes entropically favorable for hard spheres to form ordered structures. In contrast to hard spheres, colloidal functionalized nanoparticles have an easily deformable organic ligand shell with favourable interparticle interactions [39]. Therefore, the treatment of NPs as soft spheres is needed. This treatment also accounts for the variety of superlattice shapes formed at lower densities than those predicted by the hard-sphere model [39]. The shell of the organic ligand is thus crucial for the formation and final morphology of the superlattice. Furthermore, different superlattices are formed by evaporating different solvents, indicating that solvent-ligand interactions are also crucial in superlattice formation [40]. This also highlights the important interplay between solvent-ligand and ligand-ligand interactions, creating a direct link between colloidal stability and the morphology of the self-assembled superlattice.

Ligand-dependent Structure-Property Relationships

The shell structure of the organic ligand dictates the stability and overall structure of the SC while the nature of the ligand influences the short-range interactions and chemical-physical properties [25]. Organic ligands like Alkylammonium ion, oleic acid or 1-hexadecanethiol cause stress at the inorganic-organic interface, inducing changes in optical properties and influencing self-assembly and potential applications [41, 42]. For example, other organic ligands made by aliphatic chains can lead to electron trapping due to insufficient passivation of atoms on the surface [43]. Therefore, for more unstable NPs, it is logical that the organic ligand envelope may contribute to their instability, and fine-tuning the ligand envelope structure could potentially reduce this effect or even reverse it. Particularly with small NPs, where the organic component forms a substantial part of the overall structure, it is expected that stabilisation of the envelope structure could lead to more durable materials. This is a behaviour particularly observed in inorganic LHP NPs [31, 32, 38, 42, 44, 45].

The high level of control over structure-property relations makes these systems highly tunable in terms of collective responses when activated by external light excitation. An elusive topic in the field of self-assembly of colloidal NPs is the formation of mini-band structures using colloidal NPs as artificial atoms and using them to investigate transport phenomena. To obtain these systems, a very high degree of crystallinity is required [46]. Long-range transport phenomena can transiently occur in NPs capped with long ligands. At high optical excitation densities, due to multi-electronic Auger effects, the tunnelling barrier posed by organic ligands generally prevents self-assemblies from achieving the couplings necessary to guarantee long-range phenomena [47]. However, recent research has shown that this obstacle can be overcome by using aliphatic chains as organic capping ligands [46]. Therefore, the engineering of organic ligand shells could play a crucial role in the development of new electrically active nanoparticleline solids.

Ligand-coated nanoparticle supracrystals also provide a model system in experimental condensed matter physics to study critical phenomena, including phase transitions in solid 2D systems [48]. It has been demonstrated that increasing the length of alkanethiol ligands in 2D supracrystals of uniformly sized gold nanoparticles induces a ligand-dependent liquid-solid phase transition, with a hexatic phase observed at intermediate ligand lengths. The hexatic phase is a state of matter that is between the solid and the isotropic liquid phases in two-dimensional systems of particles. This suggests that the phase behavior of 2D nanoparticle supracrystals is analogous to a classical 2D melting process, where ligand chain length plays a role similar to temperature in driving the phase transition. This system serves as an effective model for investigating 2D melting in nanoparticle systems, where the phase change is driven by entropy and linked it is linked to steric constraints between ligand shells. The scaling in defect density with ligand length further supports the equivalence between ligand length and temperature in influencing the melting process, providing insights into strategies for controlling the self-assembly of nanoparticles.

Two pioneering studies [11, 12], explored the functional properties and the structure-property relationships of ligand-coated nanoparticle supracrystals. In the first study, it was investigated how dodecanethiol ligand chains, coating gold NP cores, arrange on the NP surface and throughout the supracrystal. Initial analyses showed that ligand chains adopt a preferential orientation while time-resolved studies revealed that upon light excitation, positional disorder in the supracrystal increases, while its overall homogeneity transiently improves [11]. These experiments clarified the dynamics of light-induced disorder in the system. After photo-excitation, these supracrystals reach a transient ordered state before relaxing into a more stable configuration, where some nanoparticles and ligands remain disordered. In disordered elastic media, elastic forces from chemical origin provide the binding necessary for ordering. However, since ordering and disordering are dynamic phenomena, time-resolved techniques with spatial and temporal resolution are required to capture the motions of individual microscopic constituents in real-time. Moreover, it was demonstrated that variations in chemical functionalization with different ligand lengths provide *ad hoc* functional properties, including tunable supramolecular electron-phonon coupling, high Young's moduli, and tailored collective order/disorder responses to femtosecond light pulses, as well as tunable interactions with biological matter [12]. Further dynamic studies, where ligand length was used as a tuning parameter, revealed an interdependence between ligand size, electron-phonon coupling strength, and which is the role of the system heterogeneity in nanoparticle supracrystals. Ultrafast diffraction-based methods showed that the light-induced decay of the diffraction intensity, associated with the local hexagonal arrangement of gold nanoparticles, depends on the capping ligand length. In particular, ligands with shorter lengths exhibit a higher degree of ordering, which decreases as the ligand length increases. Furthermore, the local mechanical stiffness in supramolecular assemblies of nanoparticles covered with short ligands reaches levels comparable to those observed in systems with strong covalent bonds. These covalent systems are also characterized by strong coupling between the electronic and a small subset of lattice degrees of freedom. By comparing this coupling to that in supracrystals with nanoparticles functionalized by ligands of different lengths, it was found that the local symmetry of nanoparticles at the supracrystal level affects the short-range coupling between electronic and lattice degrees of freedom. This coupling results stronger in more ordered systems, that are those with shorter ligands [12].

These works illustrate the high adaptability of these materials, making them valuable not only for advanced applications in nanotechnology and materials science but also from a fundamental perspective. Understanding and engineering the structure of the ligand envelope is essential for advancing the design and development of more energy-efficient materials.

1.3 Lead Halide Perovskites

Among colloidal semiconductor Nanoparticles (NPs), Lead Halide Perovskites (LHPs) have attracted considerable interest for their potential applications as narrowband emitters for displays and quantum light sources [5, 6]. However, their instability in

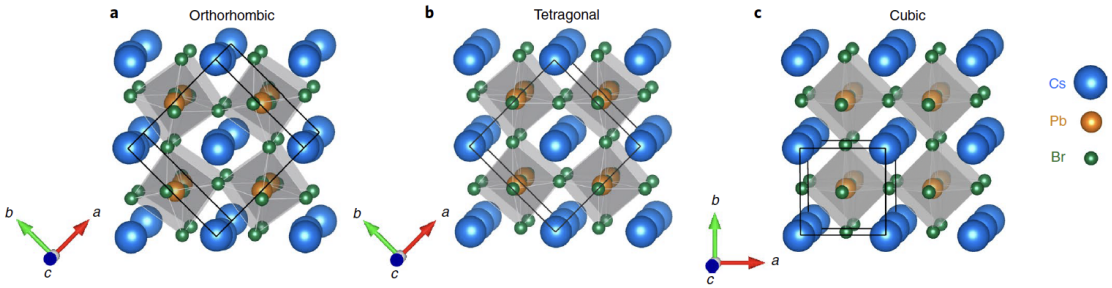

Figure 1.5: Crystal structures of $CsPbBr_3$ in the orthorhombic (a), tetragonal (b), and cubic (c) phases. Image adapted from [55].

common polar solvents has been a challenge because the functionalization of LHPs-NPs is difficult due to their structural lability [2]. Dispersing LHP NPs in polar solvents, such as acetone, alcohols, or acetylacetone, while maintaining their morphology is particularly challenging. This is due to the fact that typical anionic and cationic surfactants, which attach to the surfaces of halogenated NPs, often displace surface ions with their ligand headgroups [25]. As a result, this displacement leads to unfavourable solubilization equilibria. Over the last years, new routes have been proposed to address these issues, and it has been demonstrated that by using capping agents such as phospholipid zwitterions, robust-surface NPs of LHPs with high colloidal stability can be synthesized [2, 49–51]. This has strongly boosted the interest in the study of LHPs.

LHPs are semiconductors described by the general stoichiometric formula $APbX_3$ (where A = Cs^+, $CH_3NH_3^+$ or $CH(NH_2)_2^+$ and X = Cl^-, Br^-, or I^-).LHPs with $APbX_3$ stoichiometry have been known since the late 19^{th} century [52], although their crystal structure and semiconductive nature were not reported until the 1950s [53]. Since this work specifically focuses on $CsPbBr_3$, particular attention will be given to its structure and properties. Three-Dimensional (3D) crystal $CsPbBr_3$ consists of corner-sharing $PbBr_6$ octahedra, with Cs^+ ions occupying cubo-octahedral voids between them. The other $APbX_3$ LHPs have the same structure. Upon cooling from the high-temperature cubic perovskite phase (Pm3m), these materials undergo a series of phase transitions associated with tilts and rotations of the octahedra, as shown in Figure 1.5. In $CsPbBr_3$, a first-order phase transition occurs at $T_{C1} \approx 403$ K to a tetragonal phase (P4/mbm), followed by a second-order transition to an orthorhombic phase (Pnma) below $T_{C2} \approx 361$ K [54] [55].

Interest in the potential of LHPs for electronic and optical devices started gaining attention in the late 1990s and early 2000s [6]. However, it was only in 2009 that *Kojima et al.* [56] demonstrated their application as visible light sensitizers in solar cells. It took another three years to fully recognise their potential for highly efficient photovoltaic and lighting devices due to their long charge carrier scattering lengths, high Photoluminescence Quantum Yield (PLQY) and strong absorption coefficients [57]. Since then, the exceptional properties of LHPs have attracted the attention of not only the device community but also chemists, physicists, and materials scientists. LHPs have emerged at the forefront of materials research, not only for their

remarkable photovoltaic efficiency but also for their intriguing optical and electronic properties [6, 57] that have been increasingly understood and explored over the past decade.

LHPs have a wide range of interesting optical properties, including tunable Photoluminescence (PL) across the visible spectrum, excellent colour purity, multicolour chromism, high PLQY and high charge-carrier scattering lengths [5, 58]. The most remarkable aspect of these materials is their versatility, as their properties can be adapted by changing their composition or size. The optical and electronic properties of LHPs have been found to depend strongly on their dimensionality [5]. In contrast to classical semiconductors such as GaAs, in LHPs, the conduction band has a p-type character due to the 6p orbitals of Pb and the np orbitals of the halides. The electronic configuration of Pb(II) is 6s26p0, while it is np6 for the halides (where n = 3−5 from Cl to I) [59]. On the other hand, the valence band of the LHP consists of 6s orbitals of the Pb and np orbitals of the halides, which gives the band a partial s-type character with dipole-allowed transitions from the valence band to the conduction band. Since the top of the valence band in LHP is dominated by the halide p-orbitals, with only minor contributions from the antibonding Pb $6s^2$ orbitals, the position of the valence band becomes sensitive to the choice of halide ions.

Figure 1.6 shows how the band structure $CsPbX_3$ changes as the halide ion changes. In particular, it decreases passing from chloride (Cl^-) to bromide (Br^-) to iodide (I^-) based LHPs, which leads to a sharp increase in the absorption spectra at the optical band edge [5]. It is important to emphasise that in all three cases, there is also an excitonic contribution that influences the absorption coefficient more significantly, moving from I^- to Br^- to Cl^- based LHPs. The excitonic transitions at the band gap in LHPs suggest significant Coulomb interactions between electrons and holes. The absorption coefficient does not follow the typical square root dependence, as observed with free electrons and holes. Instead, there is an additional contribution from Sommerfeld enhancement above the band edge and excitonic transitions below. It is essential to deconvolve the excitonic transition probabilities from those of the continuum. At room temperature, the LHP NPs show PL covering the entire visible spectrum with narrow linewidths not exceeding 100 meV Full-Width Half Maximum (FWHM). Specifically, $CsPbBr_3$ NPs emit around 520 nm with a linewidth of about 20 nm, $CsPbCl_3$ NPs emit around 420 nm with a linewidth of about 12 nm, and $CsPbCl_3$ NPs emit near 690 nm with linewidths between 40 and 45 nm [6]. As shown in Figure 1.7, PL can also be adjusted in terms of both peak position and efficiency by changing the size and shape of the NPs. While LHPs in bulk generally exhibit low PLQY due to defects at grain boundaries and surfaces, NPs LHPs have emerged as highly efficient light emitters with PLQYs almost equal to 1 [5, 61]. Furthermore, the PL emission peak blue shifts as the size of the nanoparticle decreases [5, 62]. In 2015, *Protesescu et al.* synthesised monodisperse NPs of $CsPbX_3$ using the Hot Injection method, achieving a PLQY up to 90% [7]. Further optimisations improved the LHP NPs for features such as monodispersion, near-unity PLQY and colloidal stability [5, 63]. This underlines the influence of crystal size and interface composition on the optical properties of LHPs, with a marked increase in PLQY observed when the crystal size is reduced to the nanoscale. A key consequence of reducing

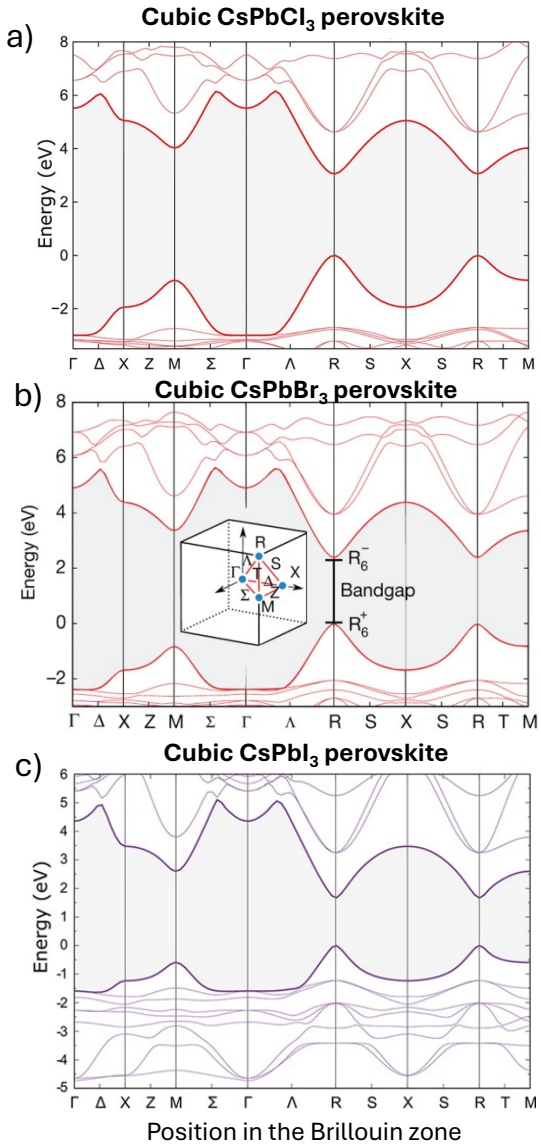

Figure 1.6: Calculated band structure of (a) $CsPbCl_3$, (b) $CsPbBr_3$, (c) $CsPbCl_3$ single crystals. The valence band maximum is set as zero. The inset in (b) shows the first Brillouin zone of the cubic crystal lattice. The electronic bandgap is indicated in the band structure at the R point. The valence (conduction) band maximum (minimum) has $R_6^+(R_6^-)$ symmetry. Image adapted from [60]

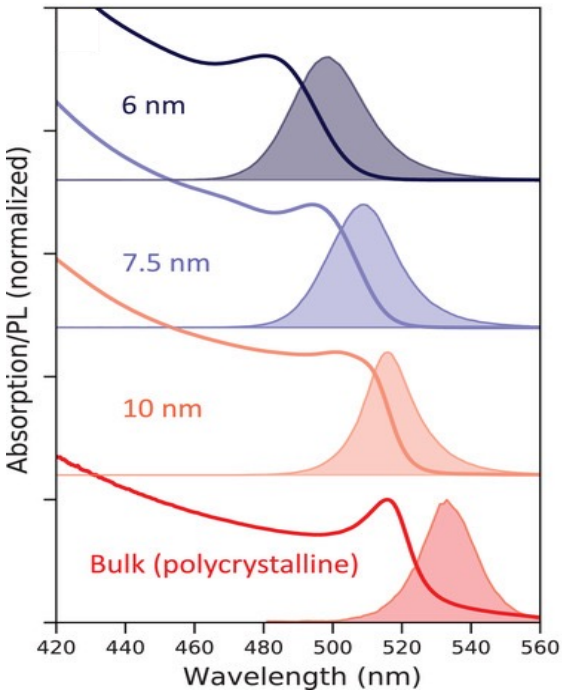

Figure 1.7: Absorption and PL spectra of $CsPbBr_3$ nanoparticles (average size 6, 7.5, and 10 nm) deposited on quartz substrates and spin-coated polycrystalline film (average grain size $\approx$ 100 nm). Image adapted from [62].

the size of LHP crystals is the appearance of quantum confinement effects. Three distinct size regimes can be identified: (i) when the size is much larger than the exciton Bohr radius ($d \gg a_B$), such that confinement effects are negligible, (ii) the weak confinement regime, where the size is comparable to the exciton Bohr radius ($d \approx a_B$), (iii) the strong confinement regime, where the exciton Bohr radius is larger than the NP ($a_B \gg d$). Quantum-confined LHP NPs exhibit blue-shifted emission compared to their 3D bulk counterparts. For example, strongly quantum-confined $CsPbBr_3$ NPs emit blue PL, whereas their 3D counterparts emit green PL.

The study of charge carrier dynamics provides further understanding of the LHP optical properties. Understanding the behavior of photoexcited charge carriers in semiconducting materials is crucial for the development of efficient optoelectronic devices and materials for photovoltaic applications. For example, let's consider the contribution of time-resolved ultrafast spectroscopy to the field of photovoltaics. This pump-probe technique (see section 2.2), enables to probe the dynamics of photoexcited carriers on femtosecond timescales, offering insights into the relaxation pathways of charge carriers right after light-matter interaction. Pioneering studies by *Grancini et al.* [9], used transient absorption spectroscopy (TAS) to reveal that in polymer solar cells, interfacial charge transfer states (CTS) and free polarons are generated within the first tens of femtoseconds after photoexcitation. These findings provide fundamental insights into the ultrafast processes triggered by light, showing how excess photon energy can be used to enhance the efficiency of charge separation. Understanding these mechanisms directly informs the design of low-

bandgap organic semiconductors, offering a pathway to improve energy conversion efficiency in photovoltaic devices, reducing recombination losses and enabling more efficient charge extraction.

Photoexcitation generates electron-hole pairs, and their energy relaxation pathways depend on various factors. In general, after the initial carrier thermalization, the hot charge carriers lose energy by emitting optical phonons and subsequently relax down to the electronic band edge. The charge carriers may then either decay radiatively, emitting light, or recombine nonradiatively. The following discussion explores the different energy relaxation dynamics in LHPs under ultrafast photoexcitation [5].

According to the Elliott model, both excitonic and interban continuum transitions contribute to the optical band gap in LHPs. Thus, their representative Transient Absorption (TA) spectra typically display two main features: a sharp Photobleach (PB) and a broad Photoinduced Absorption (PIA) [64]. PB refers to the decrease in light absorption at certain wavelengths after a material has been exposed to light. This implies that once the material absorbs photons and becomes excited, it is less prone to absorb further photons due to the absence of higher energy states that allow it. Therefore, the material in its excited state absorbs fewer photons than when it is in its fundamental state. Consequently, there is a reduction in absorption at the wavelength at which the material typically absorbs light (bleaching effect). PIA refers to an increase in the number of photons absorbed after exposure to light. In LHPs, the PB signal is attributed to both band filling and free-carrier-induced bleaching of the exciton transition while the PIA is linked to several factors such as Hot Carrier (HC) cooling, polaron formation, and free carrier absorption [64]. Figure 1.8 illustrates the thermalization and relaxation process of photoexcited electrons and holes. When excited by photons with energy exceeding the band gap, charge carriers (electrons and holes) are produced in states above the band-edge states, with a non-equilibrium energy distribution. These "HCs" thermalize through carrier-carrier scattering within 1 ps. The subsequent process, known as carrier cooling, involves the quasi-equilibrated HCs (at a temperature higher than the lattice temperature and following a Fermi-Dirac distribution) dissipating their excess energy as heat via phonon-scattering, eventually reaching the band-edge states [65, 66]. The HC cooling process can be probed using ultrafast Transient Absorption Spectroscopy (TAS). Figure 1.9 shows the time-dependent evolution of the TA spectrum (λ_{ex} = 350 nm) of $CsPbBr_3$ NP in the initial time window (0.05-0.4 ps) shows 2 PIA and 2 PB photoinduced signals. The carrier cooling time (τ_C) [67] can be derived from the kinetics of the PB signal (PB1), while the recovery of the weak secondary bleaching signal (PB2) follows the same kinetics as PB1. The lower-energy absorption band (PA2), which is related to HC cooling, has recently been linked to the formation of polarons [67–70]. The HC cooling time τ_C depends on several factors such as:

- Excitation energy: high excitation energies result in longer cooling times [67];
- Excitation fluence: HC cooling slows with increasing excitation fluence [72]. At high fluences, carrier-carrier interactions become significant, leading to the

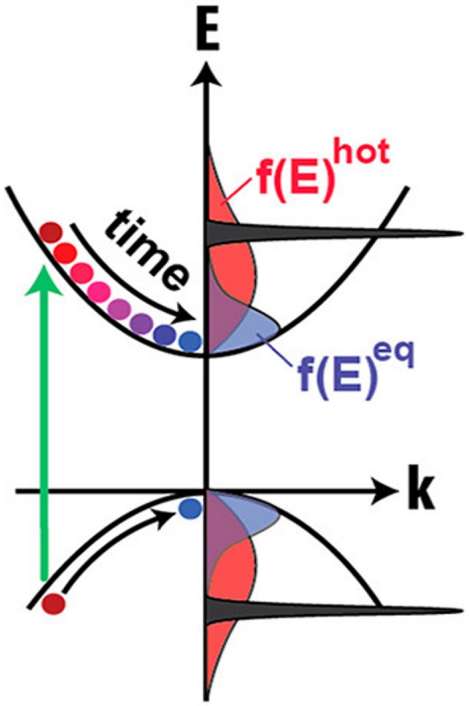

Figure 1.8: Thermalization and relaxation process of photoexcited electrons and holes in the one-particle picture. The initially δ-like distribution functions, directly after thermalization assume a (hot) thermal distribution $f(E)^{\text{hot}}$ (red). When the carriers have cooled down sufficiently to reach equilibrium with the lattice, their distribution turns to be $f(E)^{\text{eq}}$ (blue). Image adapted from [71].

re-excitation of HCs (referred to as Auger heating), which slows the overall HC cooling process;

- A-site cation composition: hybrid perovskites have faster cooling time with respect to Cs based LHP because of the stronger electron-phonon coupling that facilitated by the vibrational modes of organic cations [72];

- Size of the nanoparticle: the HC cooling time becomes faster (from 700 to 500 fs) when the size increases from approximately 4.9 to 11.3 nm [66] This acceleration in HC cooling for larger NPs is attributed to the reduced impact of the intrinsic phonon bottleneck effect, which arises from the limited availability of phonon modes in smaller NPs;

- Dimensionality of the material: HC cooling was reported to be much faster in two-dimensional (2D) nanoplatelets (NPls) compared to quasi-3D systems, [71] which is attributed to the low dielectric screening and high surface-to-volume ratio of the 2D NPls. In terms of dielectric screening, also the organic spacer used to synthesize 2D NPls influences the HC cooling dynamics [73]. A recent study has also reported a slowdown of HC cooling due to the formation of large polarons at low excitation fluence [68, 74].

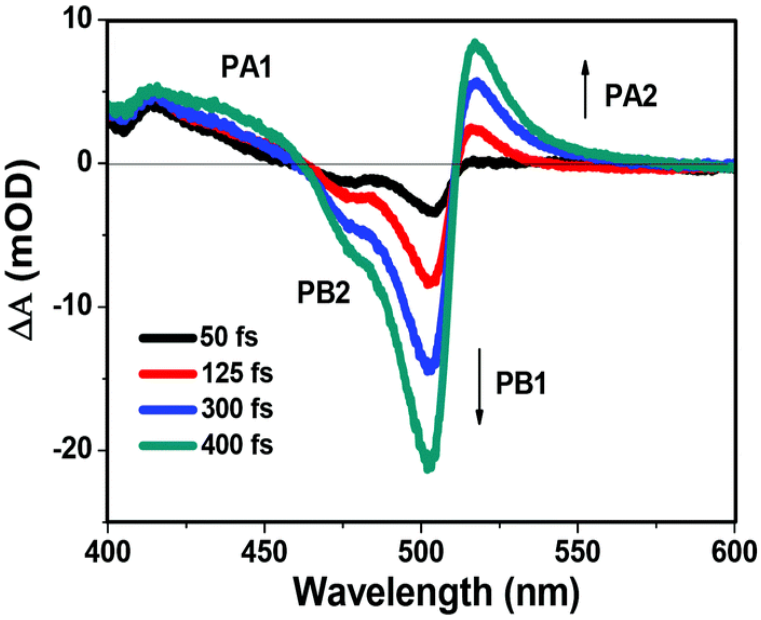

Figure 1.9: Time-dependent evolution of the TA spectrum (λ_{ex} = 350 nm) of $CsPbBr_3$ NCs in the early time window (0.05 0.4 ps). Image adapted from [67].

Radiative recombination of charge carriers in direct bandgap semiconductors significantly impacts their utility in optoelectronic devices. This radiative recombination is slower compared to exciton dephasing, spin relaxation, and HC cooling, typically occurring on the picosecond to nanosecond timescale [5]. If perovskites were perfectly defect-tolerant radiative recombination would be the main relaxation route for charge carriers [6, 75]. However, the multiexponential PL decay dynamics observed in most perovskite NPs, suggest the presence of sub-band-gap energy levels associated with defects acting as trap centers [5, 76, 77]. Therefore, minimizing nonradiative recombination is crucial for improving the optoelectronic performance of LHPs. Trapped carriers can return to the conduction or valence band and recombine radiatively if the de-trapping process is efficient but if the separation between trap states and the band-edge is high (deep trap states), charge carriers relax nonradiatively [5]. Indeed, the temporal profile of the photo bleach recovery signal in TA measurements contains a fast component due to carrier trapping, alongside a longer component due to radiative recombination [67]. A recent theoretical study indicates that halide vacancies in NPs are the primary contributors to defect energy levels, which are shallow for $CsPbBr_3$ and $CsPbCl_3$, but deep in the case of $CsPbCl_3$ [78] [79].

Although all these properties have been widely studied, especially in the last decade, the cooling of HCs in LHPs remains poorly understood and theories such as the formation of large polarons and the upconversion of acoustic to optical phonons have been proposed [32, 68, 80–83]. In 2021, *Cannelli et al.* [8] quantified for the first time the photoinduced polaronic distortions in LHP, using time-resolved X-ray absorption spectroscopy (TR-XAS) and studies of the temperature-dependent structural dynamics of the samples with static XAS. The authors demonstrated that the

lattice changes upon photoexcitation are driven by a specific polaronic distortion that occurs via the Fröhlich mechanism: charges interact with the electric field generated by the activation of specific phonons by electron-phonon coupling, in this case the optical longitudinal phonon (LO) at 18 meV. This causes localised deformation along the Br and Pb atom chains. The study, in agreement with *ab initio* simulations, excludes thermal effects as the primary source of the Pb-Br bond distortions, providing evidence that the nature of these changes is purely electronic and highlighting the significant role of polaron formation in the photoinduced response of LHP. Recently, low-energy phonons (2.5 - 12 meV) have also been involved in studies of electron-phonon coupling in lead halide perovskites (LHP) [84]. Considering multi-excitonic effects, it has been demonstrated that the number of excitons should linearly scale the strength of the coupling between charge carriers and low-energy lattice modes [84].

Supracrystals of ligand-coated $CsPbBr_3$ Nanoparticle

Having reviewed the general properties of LHPs and explored how their behaviour changes as their size decreases, we now turn our attention to the self-assembly of colloidal LHPs nanoparticles into supracrystals. One of the motivations for the superlattice assembly of $CsPbBr_3$ NPs is the opportunity to study the coupling between adjacent NPs, which can give rise to collective phenomena such as exciton delocalization and charge carrier transport [15, 85, 86]. Interesting phenomena such as electronic coupling leading to the formation of minibands, superfluorescence, and low-threshold optical gain induced by two photons, tunable anisotropic light emission, [87–90], have been also observed, making the NP superlattice $CsPbBr_3$ a promising platform for the study of collective quantum effects. An example of how coupling influences optical properties can be directly observed by looking at PL properties. Spontaneous self-assembly of single NPs retains the high PL efficiency of their NP subunits, but exhibits shifted emission relative to individual nanocubes due to inter-particle electronic coupling [88]. The electronic coupling in the SCs, which reduces the carrier scattering length and minimises trap-assisted recombination, leads to the formation of minibands in both the valence and conduction bands when the NPs are tightly packed, resulting in lower-energy optical transitions and further contributing to the observed redshift in the PL [88]. These collective properties highlight the potential of perovskite SCs for light-emitting applications.

Switching to the supracrystal framework, all these studies focused mainly on static optical properties, but to date no studies addressed the impact of ligand and core chemistry on the dynamic mesoscale properties of supracrystals. The role of heterogeneity and order/disorder dynamics, which has been explored in gold supracrystals (as discussed in section section 1.2), has not yet been addressed for LHP supracrystals. This thesis aims to fill this gap by focusing on the role of core size in mesoscale supramolecular packing and the role of heterogeneity on electron-phonon coupling. As shown in Figure 1.10, it has been recently demonstrated by [2] that zwitterionic capping ligands can be selectively tuned not only to enhance colloidal stability and preserve the emissive properties of $CsPbBr_3$ nanoparticles but also to regulate the degree of heterogeneity at the supracrystal level by adjusting

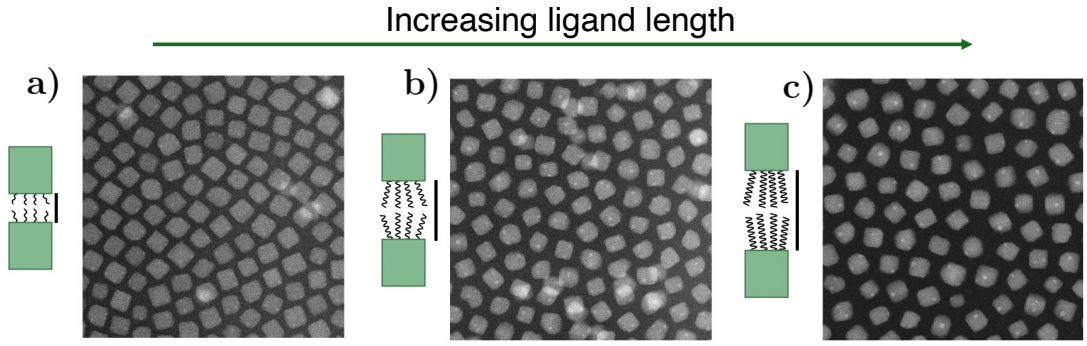

Figure 1.10: Engineering inter-NP distance in monolayers of $CsPbBr_3$ NCs capped with PEA ligands by adjusting the ligand molecular weight: Mn = 900 Da (a), 1,200 Da (b) and 5,000 Da (c). Scale bars: 20 nm. Image adapted from [2].

their length. In my work, I investigated the out-of-equilibrium dynamics related to the heterogeneity effects at the mesoscale and their connection to core size, providing new insights into the structural and functional relationships within ligand-coated $CsPbBr_3$ supracrystals.

Chapter 2

Methods and Experimental techniques

This chapter starts with an overview of the samples in section 2.1, followed by the description of the spectroscopic techniques, both out-of-equilibrium and at equilibrium, used to investigate the properties of self-assembled $CsPbBr_3$@PPG-PEA Two-Dimensional (2D) Supracrystal (SC)s. Specifically, section 2.2 provides an overview of pump-probe techniques, while Transient Absorption Spectroscopy (TAS) is discussed in detail in section 2.3.Section 2.4 and section 2.5 elaborate on the experimental techniques used to probe the steady-state sample's properties: Photoluminescence (PL) and Raman Spectroscopy.

2.1 Samples Description & Transmission Electron Microscopy

This study focuses on the analysis of two samples composed of $CsPbBr_3$ nanoparticles (NP)s, functionalized with the organic capping agent PPG-PEA-OH (Figure 2.1), which self-assemble into $CsPbBr_3$@PPG-PEA SCs. The investigation explores how differences in core size, the presence of the ligand and heterogeneity possibly affect the spectroscopic response of the samples.

The choice of capping ligand is dictated by the need to address the inherent instability problem of lead halide perovskite. It has been shown that the development of phospholipid capping ligands can significantly improve the stability and functionality of hybrid organic-inorganic Lead Halide Perovskite (LHP)s ($FAPbBr_3$ and $MAPbBr_3$ (FA, formamidinium; MA, methylammonium)) and lead-free metal halide nanoparticles. The trend in developing zwitterionic and charge-neutral phospholipid capping ligands has been motivated by recent successes with $CsPbBr_3$ Nanoparticles (NPs) [2, 49–51]. These studies show that switching from a phosphocholine (PC) headgroup to a phosphoethanolamine (PEA) headgroup increased the surface coverage and enabled robust purification through multiple precipitation cycles, all while

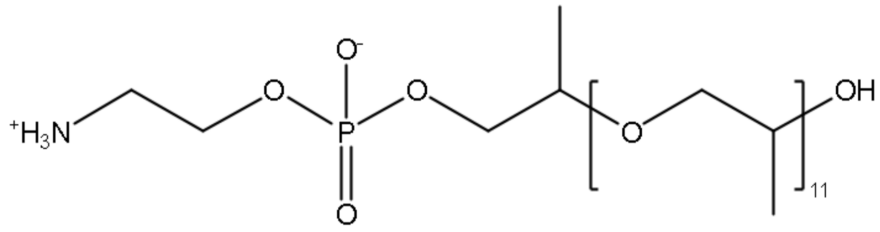

Figure 2.1: Structure of the organic capping agent PPG-PEA-OH.

maintaining the uniformity of NP[2]. Moreover, the 2-Ammonioethyl (hydroxypolypropyleneglycolyl, Mn=725) phosphate (PPG-PEA) ligand provides long-term stability in various solvents, maintaining $CsPbBr_3$ NP properties. As an example, PPG-PEA enables the dispersion of $FAPbBr_3$ and $CsPbBr_3$ in propylene glycol methyl ether acetate (PGMEA), a solvent widely used in optoelectronics. This approach made it possible to produce surface-robust and highly emissive $CsPbBr_3$ NPs.

The colloidal $CsPbBr_3$@PPG-PEA NPs were synthesized using "TOPO-DOPA" colloidal synthesis [2], yielding two distinct core sizes: 9 nm and 15 nm. This parameter is used to distinguish the two samples, which are labelled as MS0865 and MS0864, respectively. A schematic of the synthesis process is shown in Figure 2.2, where the $PbBr_2$-trioctylphosphine (TOPO) complex reacts with the diisooctylphosphinic acid (DOPA) salt of the corresponding Cs cation at room temperature, resulting in monodisperse NPs. TOPO and DOPA are considered "bad ligands" and can be readily exchanged for zwitterionic ligands such as PPG-PEA (step 2a in Figure 2.2). After synthesis, the NPs were deposited on transmission electron microscope (TEM) copper grids by drying in anti-capillary tweezers. Before deposition, the grids were cleaned with toluene to ensure cleanliness. Figure 2.3 shows the 200 mesh copper grids where the samples were placed. Additionally, a grid for substrate characterization, referred to as the "Empty Grid," was provided.

The grids [Ted Pella, Inc.] are approximately 3 mm in diameter and coated with a Formvar layer stabilized by a 5-10 nm carbon film. Moreover, since prolonged exposure to air leads to degradation of the NP layers, a custom-made sample chamber was designed and built to allow storage of the sample in a nitrogen (N_2) atmosphere. The samples were only removed from the chamber for measurements, during which they were mounted on a custom-designed sample holder. Figure 2.4 shows the sample chamber in frame (a) and a schematic of the sample holder in frame (b).

The sample chamber is connected to a nitrogen (N_2) line, allowing a regulated amount of gas to flow through the chamber. The flow is controlled by an inlet valve and measured with a flowmeter. The chamber, made of aluminium, is sealed with a plexiglass lid equipped with gaskets to ensure an airtight seal. An additional outlet valve controls the gas outflow. By closing both the inlet and outlet valves, the inert atmosphere inside the chamber can be preserved during transport.

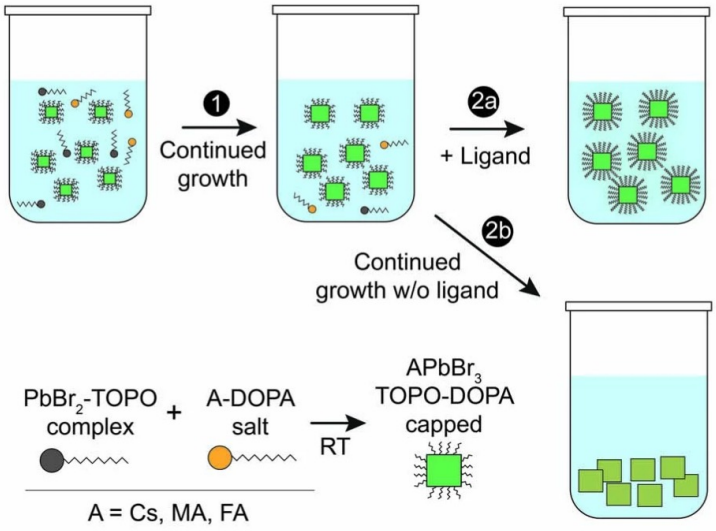

Figure 2.2: Schematic of the TOPO-DOPA colloidal synthesis process. TOPO/$PbBr_2$ nanoparticles (NPs) react with the diisooctylphosphinic acid (DOPA) salt of the corresponding Cs to form monodisperse NPs (step 1). TOPO and DOPA can then be exchanged for better ligands (step 2a), or, without further ligand addition, the NPs degrade (step 2b). Image adapted from [2].

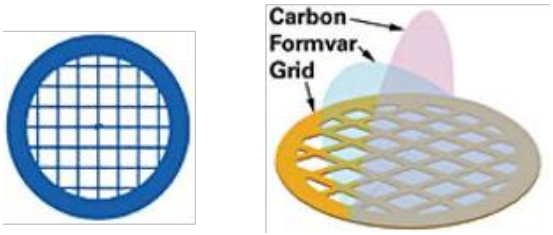

Figure 2.3: TEM grids used as a substrate for the deposition of NPs. Image adapted from Ted Pella, Inc. *Microscopy Products for Science and Industry.*

The sample holder features the copper grids, where the samples were deposited. From left to right, in Figure 2.4 b, the grids correspond to MS0864, the empty grid, and MS0865. The four pre-drilled holes accommodate M2 screws, which clamp the sample holder to its counterpart, securely sandwiching the grids and ensuring that the samples remain in place during measurements.

The morphology of the deposited NPss was assessed using the Transmission Electron Microscope (TEM). TEM is a microscopy technique in which high-resolution surface images are provided from the interaction of electrons with a sample as the beam is transmitted through the specimen and then collected to generate topographical images. This technique is particularly suited for investigating the morphology and distribution of NPs. The high surface sensitivity of TEM allows for the identification of structural details, such as particle size, shape, and packing density.

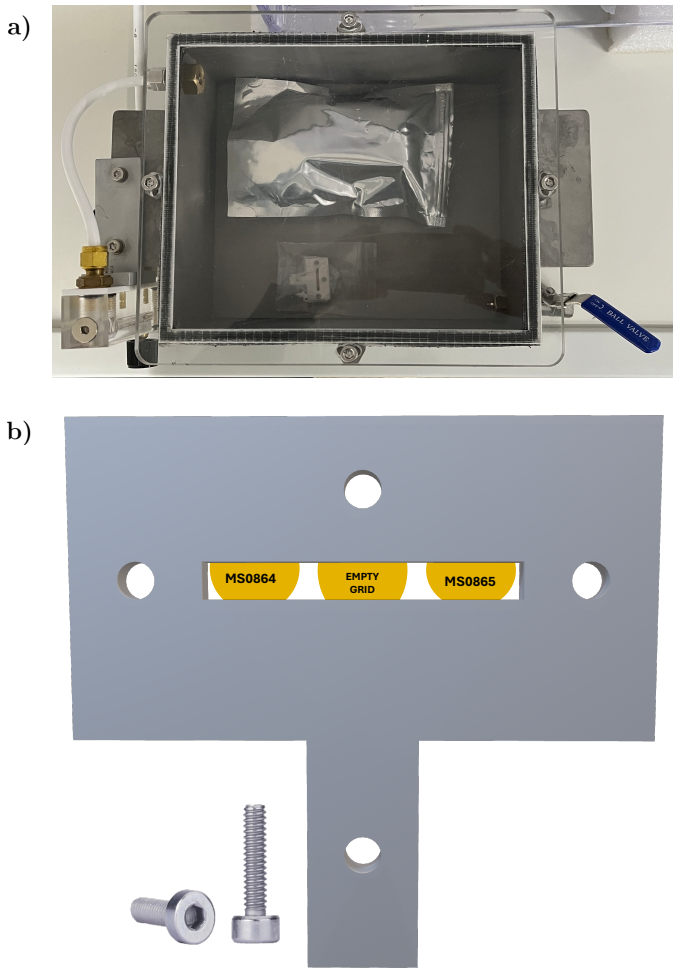

Figure 2.4: Custom-designed sample chamber (a) and sample holder (b) for preservation and copper grids mounting.

As shown in the TEM images in Figure 2.5, due to the energy of the electrons (200 keV), the cross-section interaction with the organic ligands is such that the ligands are not visible. In this figure, in addition to the TEM images of the MS0864 and MS0865 samples, the areas of interest where subsequent measurements and analyses were conducted are highlighted. From the morphological visualization, the highlighted points show that MS0864 and MS0865 display similar areas in terms of heterogeneity distribution (Figure 2.5, a-b). Moreover, when examining sample MS0865, it appears that some regions exhibit a 2D distribution (MS0865 spot 1 - Figure 2.5, b), while others show a more densely packed, bulk-like (3D) distribution (MS0865 spot 2 - Figure 2.5, c). The results and analyses that follow unfold under this framework. Based on the review of the State of The Art (chapter 1), depending on how the nanoparticles are distributed, their photoresponse is expected to change.

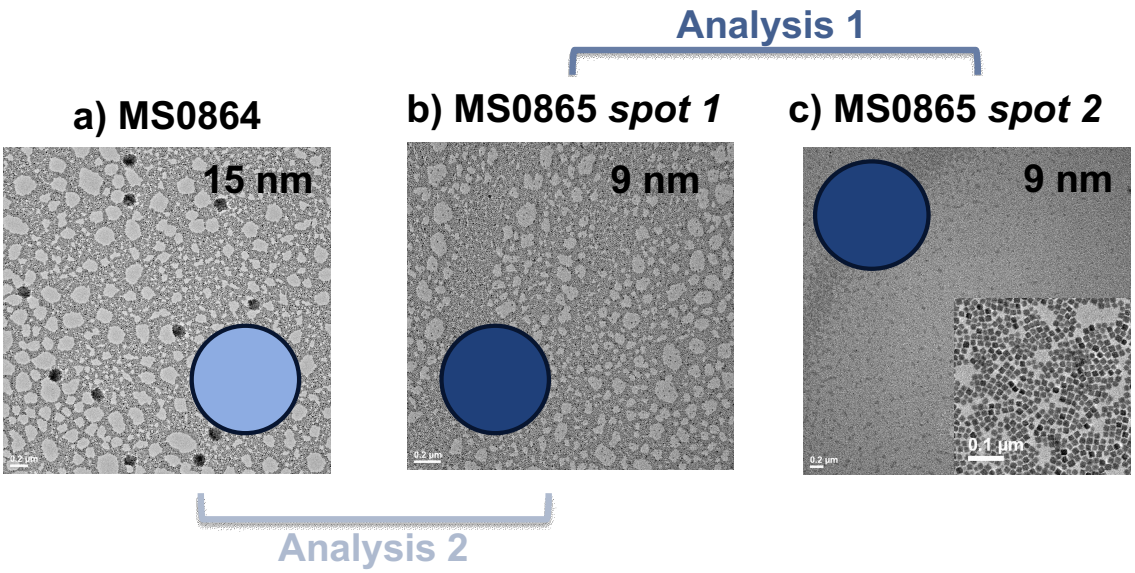

Figure 2.5: TEM images of (a) MS0864 sample (15 nm core size), and (b-c) MS0865 sample (9 nm core size). Each figure highlights the specific spot region where the measurements were performed. Two spots are selected for MS0865 to emphasize areas with different nanoparticle packing densities within the same sample, relevant to Analysis 1. Additionally, Analysis 2 compares samples based on varying nanoparticle core sizes. The scale bar for all images is 0.2 μm. The inset in (c) shows a zoom-in of individual nanoparticles with a scale bar of 0.1 μm. Images provided by courtesy of Mariia Svyrydenko (ETHZ).

The investigation that I am going to show is structured around these two comparative studies:

1. Same identical composition and core size, different mesoscale heterogeneity (Figure 2.5, b-c).

2. Same identical composition and mesoscale heterogeneity, different core size (Figure 2.5, a-b).

The focus of this work is on disentangling the effects of particle-size dependence and mesoscale heterogeneity on the photoinduced response.

2.2 Pump-probe Approach

The electronic and optical properties of materials arise from interactions between electrons and other degrees of freedom, such as lattice vibrations and spin, occurring over timescales from 10^{-18} to 10^{-9} seconds [91]. To fully understand the photophysics of complex systems, such as ligand-coated nanoparticle supracrystals, it is essential to investigate these interactions across all the interrogated time and energy scales [92]. While steady-state spectroscopy offers time-averaged insights, detailed exploration of photoinduced dynamics requires time-resolved methods with femtosecond resolution. The advent of ultrafast lasers has allowed the creation of

non-equilibrium conditions faster than energy exchanges with the lattice and magnetic excitations, revealing phenomena inaccessible to equilibrium spectroscopies [10]. This has led to the rapid growth of ultrafast time-resolved spectroscopic techniques. This growth can be attributed to the fact that they feature a single experimental scheme, referred to as Pump-probe (P-p) method [10].

The Pump-probe technique is based on stroboscopic measurements of repeatable dynamics. A pulsed laser is used as a "clock" and divided into two branches: the pump and the probe. A delay is then introduced between the pump (P), which is used to perturb matter through the photo-excitation of charge carriers, and the probe (p), a quasi-non-perturbing pulse that takes snapshots in the Fourier domain or in real space by capturing the variation of a physical observable over time. To gain access to the resulting output, a spatio-temporal overlap on the sample is required. This is achieved when the pump and probe pulses are focused in the same area of the sample and arrive on the sample surface at the same time [10]. Varying the P-p time delay allows visualization of the photoinduced response while it occurs. Tuning the pump photon energy, polarization, temporal duration, and shape is highly desirable to bring the electron system to a well-defined excited state (ES). There are several reasons for adopting this approach in the study of complex materials: i) to reveal the detailed coupling between low- and high-energy excitations [93]; ii) to explore carrier dynamics and collective effects under various excitation conditions [94]; iii) to target specific resonances involved in generating coherent collective modes [95]; and iv) to achieve light-induced control of material properties [96, 97].

This approach can be applied across different spectral regimes, including optical (UV-Vis-NIR), and hard and soft X-rays [10]. In this work, the focus is on Transient Absorption Spectroscopy (TAS), which will be discussed in detail below. This simple method can be adapted to investigate the non-equilibrium physics of solids, enabling real-time monitoring of processes like particle-hole excitations and the renormalization of high-energy collective modes, such as plasmons and excitons, providing insights into collective interactions as they unfold [95].

2.3 Transient Absorption Spectroscopy

In this work, I specifically employed Transient Absorption Spectroscopy (TAS) as the primary technique. In TAS the observed repeatable dynamics are encoded in the variations of the optical absorbance of the sample over time.

A mathematical description of the relationship between the absorption difference and the electron and lattice dynamics can be obtained by defining ΔA as the difference between the absorbance of the excited sample (A) and the absorbance of the non-excited sample (A_0),

$$\Delta A = A - A_0. \tag{2.1}$$

Since the variation in absorbance is directly related to the change in the dielectric function of the sample, $A(\epsilon)$, Equation 2.1 can be expanded using a simple first-order perturbation, under linear response assumptions:

$$A(\epsilon) \approx A(\epsilon_0) + \left.\frac{\partial A}{\partial \epsilon}\right|_{\epsilon_0} (\epsilon - \epsilon_0), \tag{2.2}$$

which implies

$$\Delta A \approx \left.\frac{\partial A}{\partial \epsilon}\right|_{\epsilon_0} (\epsilon - \epsilon_0). \tag{2.3}$$

The variation in the dielectric function, $\Delta\epsilon$, can now be expressed as a linear combination of the variations in charge carrier density n_e, electronic temperature T_e, and lattice coordinates Q_n:

$$\Delta\epsilon \approx \frac{\partial \epsilon}{\partial n_e}\Delta n_e + \frac{\partial \epsilon}{\partial T_e}\Delta T_e + \frac{\partial \epsilon}{\partial Q_n}\Delta Q_n. \tag{2.4}$$

By substituting this expression into Equation 2.3 and applying the chain rule, we can explicit the pump-induced modifications of the previous quantities in the difference absorption signal:

$$\Delta A \approx \frac{\partial A}{\partial \epsilon}\left(\frac{\partial \epsilon}{\partial n_e}\Delta n_e + \frac{\partial \epsilon}{\partial T_e}\Delta T_e + \frac{\partial \epsilon}{\partial Q_n}\Delta Q_n\right). \tag{2.5}$$

Where the first and second terms in the sum within the brackets show the dependence of ϵ from the charge carriers density n_e and the electronic temperature T_e, indicating the electron dynamics, while the third term shows the dependence of ϵ from the lattice coordinates Q_n and explicit the lattice dynamics.

Both the electronic and lattice contributions can be observed in a ΔA trace as a function of the time delay between pump and probe pulses. The electronic contribution is observed through the "incoherent response," which reflects the changes in a material's dielectric function due to band gap excitation and subsequent charge carrier relaxation. On sub-100 fs timescales, non-equilibrium charge carriers thermalize via electron-electron scattering, leading to an elevated electronic temperature T_e. This is followed by electron-phonon scattering on sub-ps timescales, where carrier and lattice temperatures equilibrate ($T_e = T_L$) [10, 98]. At high carrier densities, relaxation is dominated by non-radiative Auger recombination [99]. These relaxation dynamics are often extracted from the incoherent response using multiexponential fitting.

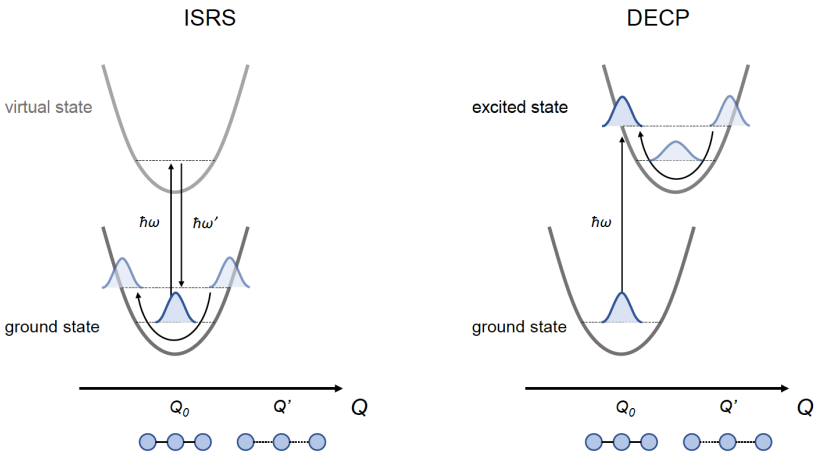

Figure 2.6: Schematic representation of the generation mechanisms of (a) ISRS and (b) DECP. In ISRS, coherent dynamics take place within the ground state electronic potential. In the DECP, the coherent response occurs in the excited state potential energy surface. Image adapted from Cannelli O. [92]

Moreover, when the duration of an ultrafast pump pulse is shorter than the period of a collective excitation, whether electronic, structural or magnetic, a coherent response arises. This response corresponds to phase-locked oscillations in the dielectric function, manifesting as oscillations in the ΔA signal over time [100]. Coherent phonons are typically generated through two mechanisms: Impulsive Stimulated Raman Scattering (ISRS) and Displacive Excitation of Coherent Phonons (DECP). The former, as illustrated in Figure 2.6 (a), occurs when the dielectric function depends on lattice displacement ($\partial\epsilon/\partial Q_n \neq 0$), leading to coherent phonon motion that starts in the electronic ground state potential, provided the phonon is Raman active [101, 102]. The latter, shown in Figure 2.6 (b), is initiated by an impulsive shift in the excited state potential surface caused by electron-phonon interactions, resulting in coherent excitation.

In conclusion, TAS captures dynamics on time scales from femtoseconds (10^{-15} s) to nanoseconds (10^{-9} s), providing insights into transient states, energy transfer, charge separation, and relaxation mechanisms following light-matter interactions. This powerful time-resolved optical technique is essential for studying ultrafast excited state dynamics in (soft)-condensed matter, offering a valuable understanding of fundamental processes in photochemistry, photophysics, and materials science.

2.3.1 TAS Setup

The TAS setup described here is designed to investigate the ultrafast dynamics of excited states in (soft) condensed matter systems. It operates in a pump-probe configuration, where a pump pulse excites the sample, and a probe pulse monitors the response at varying time delays. The key components include a PHAROS femtosecond laser system, an optical parametric amplifier (OPA) module called ORPHEUS, and the HARPIA pump-probe spectrometer, which together enable precise time res-

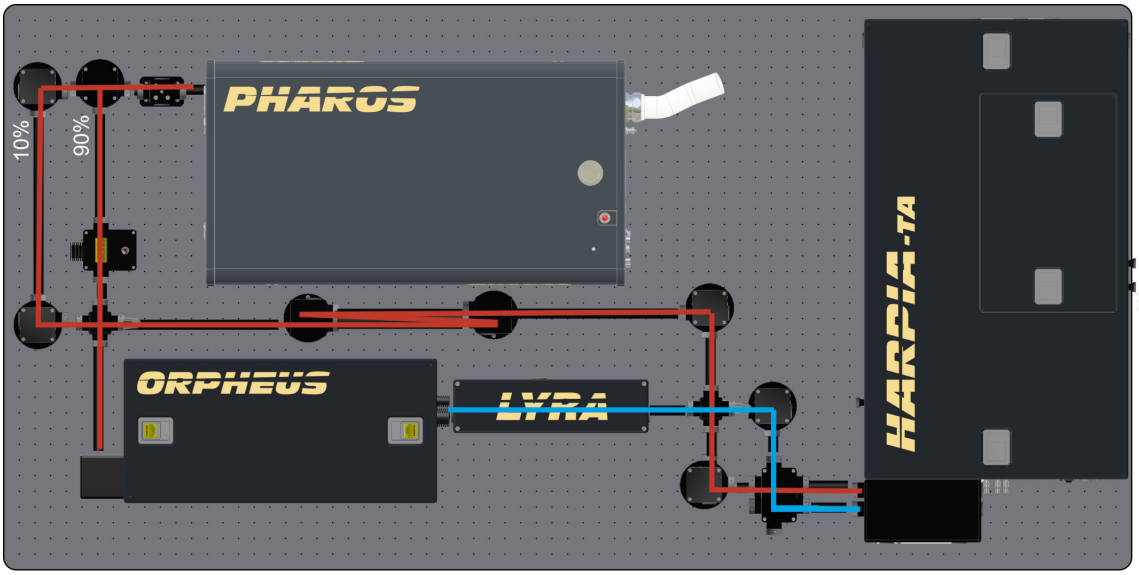

Figure 2.7: Typical external layout of HARPIA-TA system. PHAROS output is split 90 % / 10% to pump an ORPHEUS OPA and to generate the probe beam, respectively. A delay is introduced for the fundamental beam before entering HARPIA-TA in order to facilitate proper timing for both pulses. Image adapted from HARPIA Manual by Light Conversion.

olution and broad wavelength tunability. A schematic of the TAS system is shown in Figure 2.7. In this setup, both the pump and probe pulses are generated from a single laser source within the PHAROS module. The majority of the fundamental beam (E_0 = 1.23 eV), typically 90% of the total power, is directed into the ORPHEUS OPA, whose output is used as the pump light (depicted as the blue line in Figure 2.7). The remaining 10% of the beam is sent into the HARPIA-TA spectrometer to generate a white light continuum (WLC), which serves as the probe pulse.

PHAROS Laser System

The laser source for the TAS setup is the PHAROS PH2-10W laser, one of the femtosecond lasers in the PHAROS series designed by Light Conversion for industrial and scientific applications. It consists of a Yb oscillator emitting pulses with 1.23 eV central energy and 170 femtosecond (fs) pulse duration. The laser system is equipped to operate at a repetition rate of up to 50 kHz, with an average output power of 10 W before entering the Optical Parametric Amplification (OPA) stage. The pulse energy before the OPA is around 190 µJ, and the output polarization is horizontal, *i.e.* parallel to the optical table (that is p-polarized with respect to the plane of incidence identified by the direction normal to the sample holder and the beam direction).

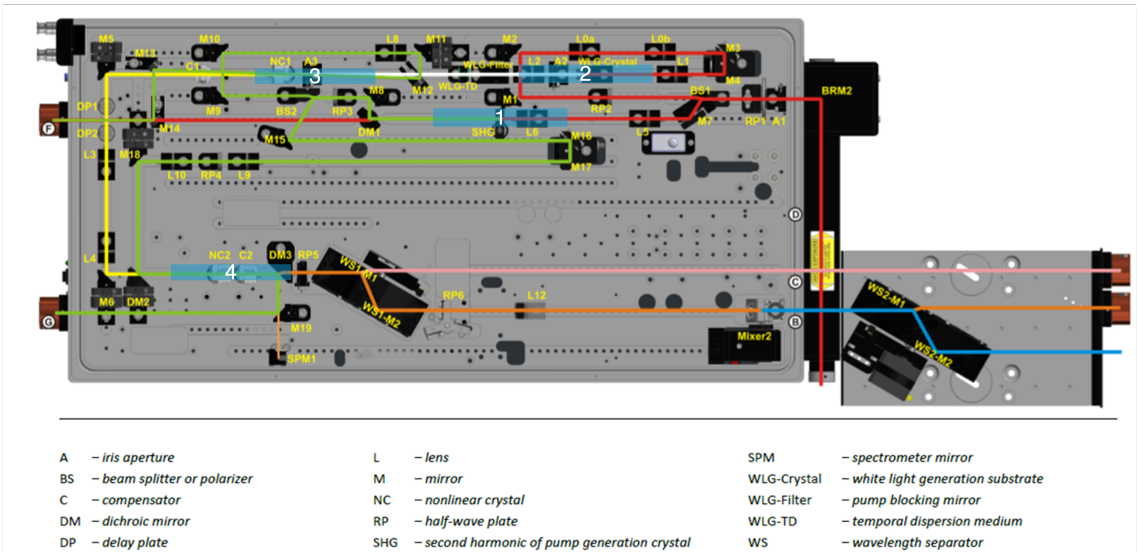

Figure 2.8: Optical layout of ORPHEUS with the main stages of non-linear optical spectral conversion shown in boxes 1 (Second Harmonic Generation), 2 (continuous White Light Generation), 3 (first Optical Parametric Amplification stage), 4 (second Optical Parametric Amplification stage). All other optical elements are labelled in yellow and the labels are listed at the bottom of the figure. Image adapted from ORPHEUS Manual by Light Conversion.

ORPHEUS Optical Parametric Amplifier (OPA)

190 µJ of the PHAROS beam (1.23 eV) are sent into an Optical Parametric Amplifier (OPA), specifically the ORPHEUS module which plays a critical role in extending the spectral tunability of the system. Optical parametric amplifiers (OPAs) exploit second-order non-linear crystals to transfer energy from a fixed frequency pump pulse to a variable frequency signal pulse. OPAs can also act as broadband amplifiers, transferring energy from a narrowband pump to a broadband signal [103].

As can be seen in Figure 2.8, inside the OPA, the first beam splitter BS1 reflects most of the pump beam energy for the Second Harmonic Generation (beam 1) that occurs at box 1 while transmitting 0.5 µJ to 1.5 µJ for White Light Continuum generation (beam 2) that occurs at the box 2. The second harmonic-generated beam 1 is firstly separated from the 1.23 eV fundamental radiation and then partially transmitted (beam 1a) through another beam splitter BS2 for the first (pre-) amplification stage, and partially reflected (beam 1b) for the second amplification stage. The first stage produces stable and sufficiently bright seed pulses for the second stage. The second stage amplifies the same pulse even further.

At the first amplification stage, box 3 in Figure 2.8, white light-generated beam 2 acts as the seed of a Broadband Optical Parametric Amplification process. In contrast, beam 1a acts as the pump. After the amplification, the amplified seed is referred to as the Signal beam, while additional photons generated in the nonlinear crystal constitute the Idler beam. The energy of the Idler depends on the pump energy, which is fixed at 2.41 eV, and the seed energy, which is tunable in the

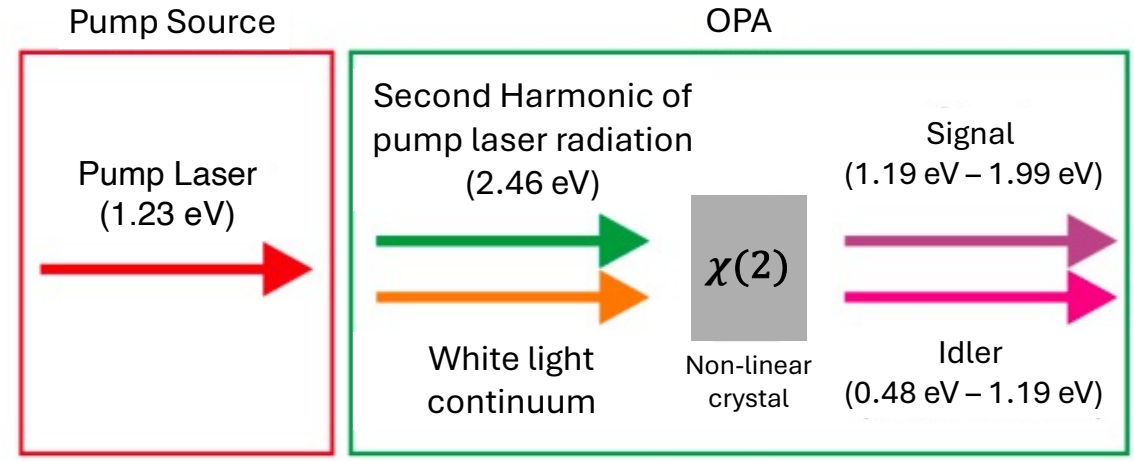

Figure 2.9: Scheme of the Optical Parametric Amplification process occurring in the first amplification stage. Image adapted from ORPHEUS Manual by Light conversion.

1.23 eV - 1.97 eV energy range. The energy of the pump photon must be equal to the sum of the Signal and Idler photon energy (0.48 eV - 1.19 eV). A schematic representation of the process occurring is illustrated in Figure 2.9.

An OPA process is efficient when, in addition to energy conservation, the phase-matching condition is satisfied $\Delta\vec{k} = \vec{k}_3 - \vec{k}_2 - \vec{k}_1 = 0$. For the non-collinear interaction between pump and signal, the phase matching condition is directly extended to the momentum conservation $\hbar\vec{k}_3 = \hbar\vec{k}_2 + \hbar\vec{k}_1$ that leads to the vectorial formulation of the non-collinear phase matching condition $\vec{k}_3 = \vec{k}_2 + \vec{k}_1$, where k_i are the wave vectors of the interacting beams. To satisfy this condition, the non-linear crystal must be rotated to a specific angle with respect to the incoming beams [103]. This angle is dependent on the input radiation energy and must be tuned accordingly with the different energies required. The phase matching angle (PMA) adjustment is performed by computer-controlled rotation stage Crystal 1.

The amplified portion of the white light continuum, beam 2 (seed in the energy range 1.23 eV - 1.97 eV), after exiting the first amplification stage, travels through two delay plates used to fine-tune the temporal overlap with the pulses of the second harmonic-generated beam 1b at Crystal 2, where the second Optical Parametric Amplification process occurs (box 4). A computer-controlled rotation stage Crystal 2 performs the phase matching angle adjustment. Both the signal and idler of the OPA process can be used as output or combined to generate output beams at further energies, and other additional frequency mixers (Different Frequency Generation DFG, Third Harmonic Generation THG, and Deep Ultraviolet Generation DUV) can also be used to emit energy from 0.06 eV - 6.70 eV. In our configuration, the OPA module allows the generation of radiation energies in a wide range, from 0.46 eV - 4.00 eV, with the output beam vertically polarized. The energy tuning is particularly important in TAS because the different excitation energies allow different photophysical processes to be initiated. The output of the Pharos then passes through the M2 mirror to the HARPIA where it is used as a pump beam.

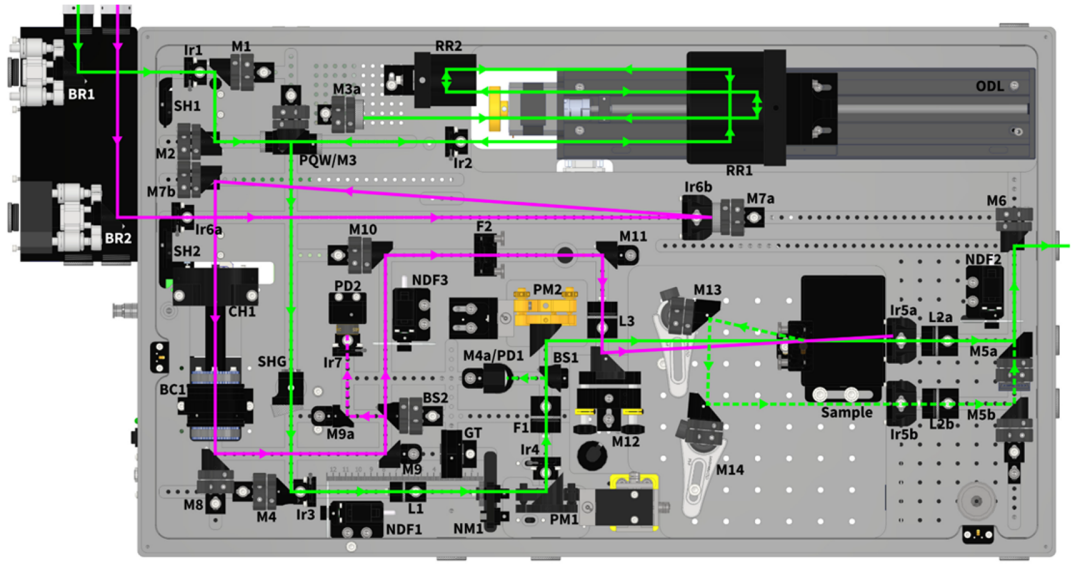

Figure 2.10: Optical layout of HARPIA-TA. The pump beam is depicted in magenta, whereas the probe beam is depicted in green. Abbreviations: Berek's compensator (BC), beamsplitter (BS), external beam routing mirrors (BR), chopper (CH1), filter (F), Glan-Taylor polarizer (GT), iris (Ir), mirror (M), lens (L), neutral density filter (NDF), nonlinear medium (NM), optical delay line (ODL), photodiode (PD), parabolic mirror (PM), polarizer/quarter-wave plate unit (PQW), retroreflector (RR), shutter (SH), 2nd harmonic generation unit (SHG). Image adapted from HARPIA Manual by Light Conversion.

HARPIA spectrometer

Once the appropriate radiation energy is selected using the OPA, the beam is directed into the HARPIA pump-probe spectrometer, which serves as the core of the TAS setup. The optical layout of HARPIA-TA is shown in Figure 2.10.

Pump path

As illustrated in Figure 2.10, the incoming pump beam is reflected by mirror M7 and directed towards the optical chopper CH1. The chopper CH1 alternately blocks and unblocks the excitation beam, allowing for the measurement of "pumped" and "not pumped" data. This modulation can occur either synchronously or asynchronously with respect to the laser pulse train, which is a series of laser pulses equally spaced in time, and so emitted at a constant frequency determined by the repetition rate of the laser. In the current setup, the chopper frequency is fixed at $f_{\text{chopper}} = 150\,\text{Hz}$, so the modulation is asynchronous.

Figure 2.11 shows how the frequency of the chopper affects the pulse train. Reducing the frequency of the chopper decreases the number of times per second the pump beam is modulated, resulting in longer intervals between "pumped" and "not pumped" states. A lower chopper frequency means longer acquisition times, as fewer pump-probe cycles are completed in 1 s. After passing through the chopper, the pump beam encounters Berek's compensator (BC1), which controls its polarization. The beam is then reflected by mirrors M8 and M9 before reaching the beamsplitter

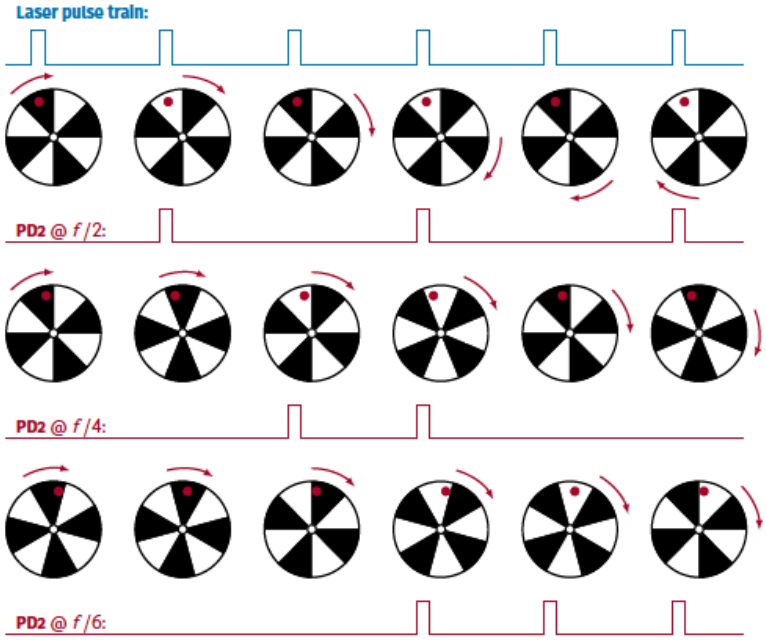

Figure 2.11: Locking the chopper frequency according to the laser pulse train. In this instance, the chopper blade synchronously enables or blocks a burst of laser pulses. The traces below the chopper illustration indicate the signals that would be observed by the PD2 pump photodiode. Image adapted from HARPIA Manual by Light Conversion.

BS2. At this point, approximately 5% of the beam is reflected toward photodiode PD2 to monitor the pump energy, while the remaining beam continues through the variable neutral density filter NDF3, which adjusts the pump power on the sample. Next, the beam is focused by lens L3 (with a focal length ranging from 200 mm to 300 mm) and directed by the fine-adjustment mirror M12 on the sample. M12 is used to optimize the overlap of the pump and probe beams at the sample plane. After interacting with the sample, the pump beam is blocked from further propagation by iris Ir5a.

Probe path

The probe beam passes through the shutter SH1, gets picked up by mirror M1 and is then directed to the optical delay line (ODL) by mirror M2. The ODL typically consists of a hollow 63 mm clear aperture gold or aluminium retro-reflector RR1 mounted on a 300 mm mm long translation stage. The probe beam path after mirror M2 may vary depending on the particular HARPIA configuration. In the "8 ns" configuration used for experiments presented in this thesis work, the mirror M3 is replaced by a thin film polarizer/quarter-wave plate unit PQW. A p-polarized (*i.e.*, horizontally) beam passes through the thin film polarizer, and a quarter-wave plate turns the polarization of the outward beam circular. This circularly polarized beam then enters the ODL, where it undergoes a total of four passes between retroreflectors RR1 and RR2, hits the mirror M3a, and goes back along its original path. After making four additional passes between the two retroreflectors, the beam passes once more through the quarter-wave plate, which now turns the circularly-polarized beam

into an s-polarized one (*i.e.*, vertical). The 45° thin film polarizer reflects this beam towards the white light supercontinuum (WLSc) generation stage.

After the ODL stage, the beam is directed into the WLSc generator by the mirror M4. WLSc generator consists of iris Ir3, a variable neutral density filter (NDF1), lens L1, and a nonlinear medium (NM1), which is either sapphire for UV/VIS Broadband WLSc or yttrium aluminium garnet (YAG) for NIR Broadband WLSc. The setup also includes a collimating 90° off-axis parabolic reflector (PM1), iris Ir4, and a band-stop filter (F1), which removes excess fundamental light from the WLSc, thereby enabling measurements around the fundamental radiation energy. PM1 is used to collimate the diverging white light beam, whereas iris Ir4, positioned right beside it, is used to reduce the spatial chirp of the WLSc beam (typically, to eliminate the outer red-coloured rings surrounding the central beam). WLSc generator produces a collimated beam of probe light that is focused onto the sample by the second 90° off-axis parabolic reflector PM2. In the visible range, the WLSc-generated beam possesses a broad band energy distribution that goes from 1.46 eV to 2.82 eV.

After passing the sample, WLSc is re-collimated by the lens L2a and steered by the mirrors M5a and M6 towards the spectrograph. NDF2 is a circular variable neutral density filter providing attenuation of the probe beam to avoid saturation of the detector. The sample is mounted on an XY translation stage, which allows precise control over the position of the beams relative to the sample. The position of the sample stage can be finely adjusted through software control. This precise positioning enables the exploration of different areas of the sample and provides insight into the material's homogeneity by observing variations in the pump-probe signal across different positions on the sample.

Andor Kymera 193i-B2 spectrograph

The spectrograph is an Andor Kymera 193i-B2 composed of the following components, enumerated as in the sketch illustrated in Figure 2.12:

1. **Mirror 1** collects light from the sample and redirects it to the second mirror.
2. **Mirror 2** directs the collected light onto a grating.
3. **Grating** disperses the light into its spectral component. It can be exchanged depending on whether measurements are made in the UV/VIS or IR region.
4. **Focusing (curved) Mirror 4** focuses the diffracted light on a motorized mirror.
5. **Motorized mirror** moves depending on whether measurements are performed in the UV/VIS or IR region.
   (a) If measurements are in the NIR region, it reflects light to an InGaAs NIR detector.

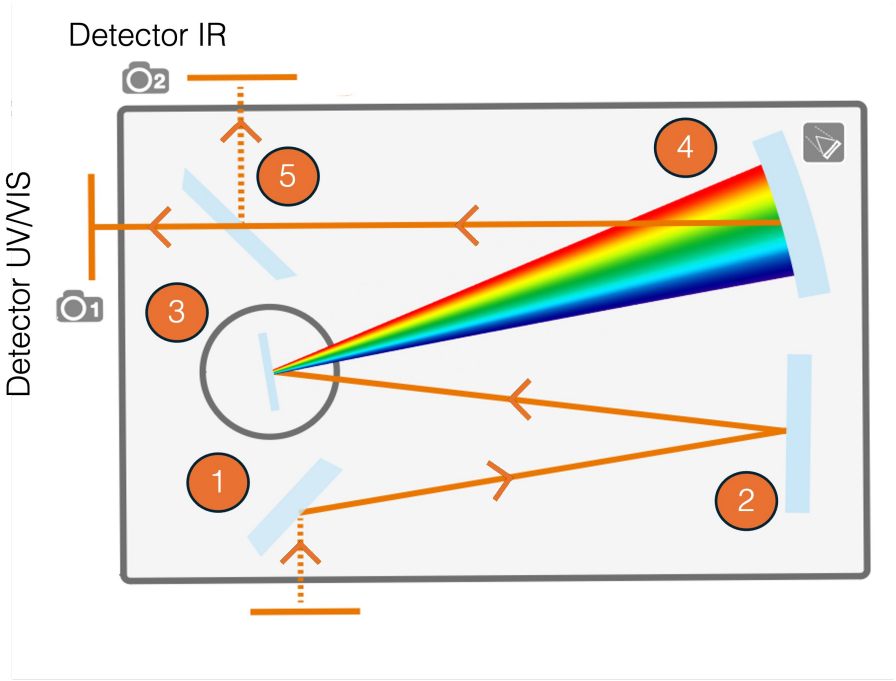

Figure 2.12: Sketch of the configuration of the Andor Kymera 193i-B2 spectrograph with its key components. Image adapted from Kymera 193i Spectrograph Manual by Oxford Instruments.

(b) If measurements are in the UV/VIS region, it moves out from the beam path, allowing the light to go straight and be transmitted toward the Silicon NMOS UV/VIS detector.

2.4 Photoluminescence Spectroscopy

Photoluminescence (PL) Spectroscopy was employed to explore the ground-state properties of $CsPbBr_3$@PPG-PEA nanoparticle SCs. This technique involves analyzing the spectrum of light spontaneously emitted from the sample after optical excitation, with the PL emission intensity measured as a function of the radiation energy.

When light is directed onto a sample imparts energy to the material in a process known as photo-excitation. One way in which the energy can be dissipated by the sample is through the emission of light, or luminescence. In the case of photo-excitation, this luminescence is specifically called Photoluminescence. Photo-excitation causes a material's electrons to move into excited states. When these electrons return to their equilibrium states, the excess energy is released and can result in the emission of light (radiative process) or not (non-radiative process). The energy of the emitted light is associated with the difference in energy levels between the two electron states involved in the transition from the excited state to the ground state. The intensity of the emitted light is related to the relative contribution of the radiative process. Therefore, PL spectroscopy constitutes a non-contact,

non-destructive method for probing the electronic structure of materials.

Figure 2.13 shows schematic energy scales representing (a) atomic and (b) semiconductor electronic transitions in a PL experiment. A monochromatic light source with peak frequency ν_p and power P_p is used to excite an electron from an atomic (or electronic) ground state to an excited state. As a result of this excitation, a non-equilibrium concentration of excited state atoms, or conduction electrons and valence holes, is created within the portion of the sample illuminated by the source. A combination of radiative and non-radiative processes de-excite the samples bringing the concentration of excited atoms or excess carriers back to the ground state.

In the case of atomic transitions (Figure 2.13, a) this process can be accurately described by discrete three-level model wherein the PL emission of interest corresponds to a transition from an excited state energy level E_2 to a ground state energy level E_1, and the optical pump photons of energy $h\nu_p$ are resonantly absorbed and excite the system from E_1 to a higher excited state E_3. The system de-excites from E_3 by a variety of competing processes: radiative and nonradiative de-excitation from $E_3 \rightarrow E_1$, or radiative and nonradiative de-excitation from $E_3 \rightarrow E_2$. In a solid or soft matter sample, vibrations correspond to a phonon density of states and $h\nu^*_{ph}$ is defined as the phonon energy with the highest density of states. If the energy of $h\nu^*_{ph}$ closely matches the energy difference $E_3 - E_2$, one (or two) phonons can easily be generated as a by-product of an $E_3 \rightarrow E_2$ nonradiative transition R_{32}. This nonradiative transition will dominate the de-excitation of the energy level E_3 and lead to an efficient populating of E_2, in turn leading to an $E_2 \rightarrow E_1$ transition and radiative PL emission. The $E_2 \rightarrow E_1$ transition is due to a combination of nonradiative processes (including phonon generation), and radiative de-excitation, quantified by the rates $1/\tau_{nr}$ and $1/\tau_r$, respectively. When the difference $E_2 - E_1 \gg h\nu^*_{ph}$, multiple phonons (a low probability many-body process) must be generated to complete the non-radiative transition. Thus, the radiative transition rate $1/\tau_r$ will dominate and PL emission will be efficiently observed. Light emission from this $E_2 \rightarrow E_1$ transition will be observed with a peak wavelength λ_{PL} (corresponding to an energy $h\nu_{PL} = E_2E_1$).

For an electronic energy transition, such as the electron-hole recombination in semiconductors, a continuum of valence and conduction band states are separated by a band gap, which is somewhat analogous to a four-level model (Figure 2.13, b). Valence electrons are excited from below the valence band E_V, to available unoccupied states above the conduction band E_C. In the conduction band, picosecond time-scale electron-electron and electron-phonon scattering events result in rapid thermalization and relaxation to energy levels close to E_C. Recombination of these excess conduction band electrons with excess valence band holes results in an $E_C \rightarrow E_V$ transition and radiative PL emission.

PL measurements were performed at room temperature (RT) using a Horiba Fluorolog spectrofluorometer. The spectrofluorometer has the following components:

1. **Light source:** A 450 W xenon arc lamp which provides radiation in the

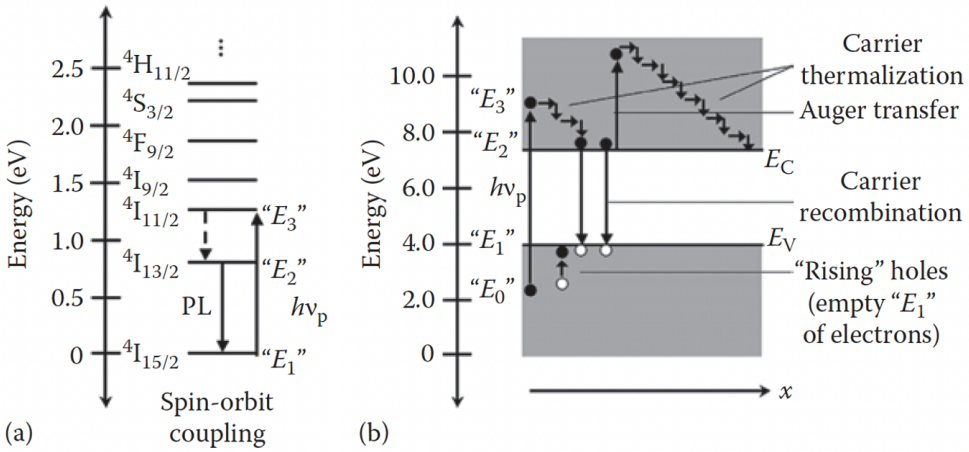

Figure 2.13: Energy scales illustrating two examples of electronic transitions. (a) Atomic transition: an electron is excited to the third energy level (E_3) and undergoes nonradiative decay to E_2, followed by radiative decay from E_2 to E_1. (b) Semiconductor transition: an electron in the valence band (E_0) absorbs a photon and is promoted to the conduction band, leaving a hole in the valence band. After thermalization, the electron at E_2 recombines through either radiative or nonradiative processes. Adapted from R. P. Prasankumar and A. J. Taylor [91].

spectral range between 250 nm to 700 nm.

2. **Excitation spectrometer:** The light is dispersed and a slit is used to select a specific wavelength to be sent on the sample.

3. **Sample chamber:** The sample interacts with the incoming radiation.

4. **Emission spectrometer:** The light emitted from the sample is filtered and directed either to a Hamamatsu R928 photomultiplier tube, optimized for the visible range, or to a CCD array, extending the detection range from UV to near-infrared.

5. **Detector:** A spectrum is generated by scanning one or both spectrometers over a wavelength range and recording the intensity variation at each wavelength.

6. **Controller (the "SpectrAcq"):** The spectrofluorometer components (spectrometers, sample chamber, accessories) are connected to a controller that communicates with the host computer.

An ideal spectrofluorometer would provide a constant photon flux across all wavelengths, have uniform sensitivity to emitted wavelengths, and eliminate stray light (*i.e.*, light unrelated to luminescence). To reduce stray light, the entrance and emission spectrometers are equipped with double diffraction gratings and variable slits

that allow only the selected wavelength to pass. Key adjustable parameters for luminescence measurements include excitation and emission wavelengths, slit widths, sampling increments, and integration time.

A PL experiment can be performed by measuring the fluorescence properties of samples either through the light emitted by the sample (emission experiments) or through absorbed light (excitation experiments). Emission measurements are performed to record the PL spectrum of a sample when it is excited at a specific radiation energy. This provided information on the energy states and relaxation processes of the sample. In this experiment, the sample is illuminated with a monochromatic light source set to a fixed excitation radiation energy. This energy is chosen based on the known or expected absorption characteristics of the sample. After excitation, the sample emits light when the electrons return to their fundamental state and emitted light is typically collected at a 90-degree angle to minimise scattered excitation light. The emitted light passes through a second spectrometer that disperses the different emission components. The intensity of the emitted light is recorded as a function of the radiation energy using a photomultiplier tube or CCD detector, producing an emission spectrum. Excitation experiments are performed to determine which radiation energy is most effective in exciting the sample to emit fluorescence at a specific pre-set energy. In this experiment, a fixed radiation energy is chosen, usually corresponding to the central energy of the observed emission peak. The excitation spectrometer scans a range of excitation energies while the emission is monitored at the fixed emission energy. The intensity of the emitted light is recorded as a function of the excitation energy, producing an excitation spectrum.

2.5 Raman Spectroscopy

Raman spectroscopy is a powerful analytical technique used to study vibrational, rotational, and other low-frequency modes in a condensed matter system. When monochromatic light is incident on a molecule, most of the light is elastically scattered, meaning the scattered photons have the same frequency as the incident photons. This is known as Rayleigh scattering. However, a small fraction of the light is inelastically scattered, resulting in photons with frequencies different from the incident light. This phenomenon is called Raman scattering and pertains to the so-called "Raman Effect". In classical electromagnetism, the Raman effect can be explained by the interaction of the incident electromagnetic wave with the molecular dipole moment induced in the molecule. When a molecule is exposed to an external electric field $\mathbf{E}(t)$, the distribution of the electron cloud in the molecule is displaced relative to the nuclei, generating an oscillating dipole moment $\mathbf{p}(t)$.

The induced dipole moment $\mathbf{p}(t)$ can be expressed as a power series expansion of the electric field $\mathbf{E}(t)$:

$$\mathbf{p}(t) = \alpha \cdot \mathbf{E}(t) + \frac{1}{2}\beta \cdot \mathbf{E}(t)\mathbf{E}(t) + \frac{1}{6}\gamma \cdot \mathbf{E}(t)\mathbf{E}(t)\mathbf{E}(t) + \cdots \tag{2.6}$$

where: α is the polarizability tensor; β is the hyperpolarizability tensor, and γ is the second-hyperpolarizability tensor.

In the theoretical description of Raman spectroscopy, typically only the first term of the expansion is considered, as contributions from the higher-order terms are assumed to be negligible and related to other effects, such as hyper-Raman scattering. Thus, the expression for the induced dipole moment simplifies to:

$$\mathbf{p}(t) = \alpha \cdot \mathbf{E}(t). \tag{2.7}$$

The induced dipole moment oscillates at the frequency of the applied electric field. However, taking into account a modulation of the molecular polarizability as a function of the normal vibrational coordinates also leads to scattered light components with different frequencies. If the polarizability α of the molecule changes, the oscillation will occur not only at the frequency of the incident light ω_1 but also at frequencies $\omega_1 \pm \omega_k$, where ω_k corresponds to the vibrational or rotational frequencies of the molecule. The component of the scattered light at the same frequency as the incident light (ω_1) is the Rayleigh scattering, while the components at shifted frequencies ($\omega_1 \pm \omega_k$) are the Raman scattered components. Indeed, considering only vibrational transitions under the assumption of electrical harmonicity, the polarizability tensor can be expanded as a first-order Taylor series in the normal coordinates. This expansion allows us to describe the induced dipole moment as the sum of three components corresponding to different scattered light frequencies:

$$\mathbf{p} = \mathbf{p}(\omega_1) + \mathbf{p}(\omega_1 - \omega_k) + \mathbf{p}(\omega_1 + \omega_k). \tag{2.8}$$

The scattered light includes:

- **Rayleigh scattering** (elastic scattering), where the scattered light retains the frequency of the incident light.
- **Stokes Raman scattering**, where the scattered light has a lower frequency than the incident light, corresponding to a transition from the ground state to a higher vibrational state.
- **Anti-Stokes Raman scattering**, where the scattered light has a higher frequency than the incident light, corresponding to a transition from a vibrationally excited state to the ground state.

Expressing the average dipole power, the intensity of the Raman-shifted light can be demonstrated to be dependent on the fourth power of the vibrational frequency and the square of the first derivative of the polarizability with respect to the normal vibrational coordinate Q_k. Therefore, a non-zero change in polarizability with respect to the vibrational coordinate is required for this effect to occur.

Both classical and quantum descriptions attribute the Raman effect to this change

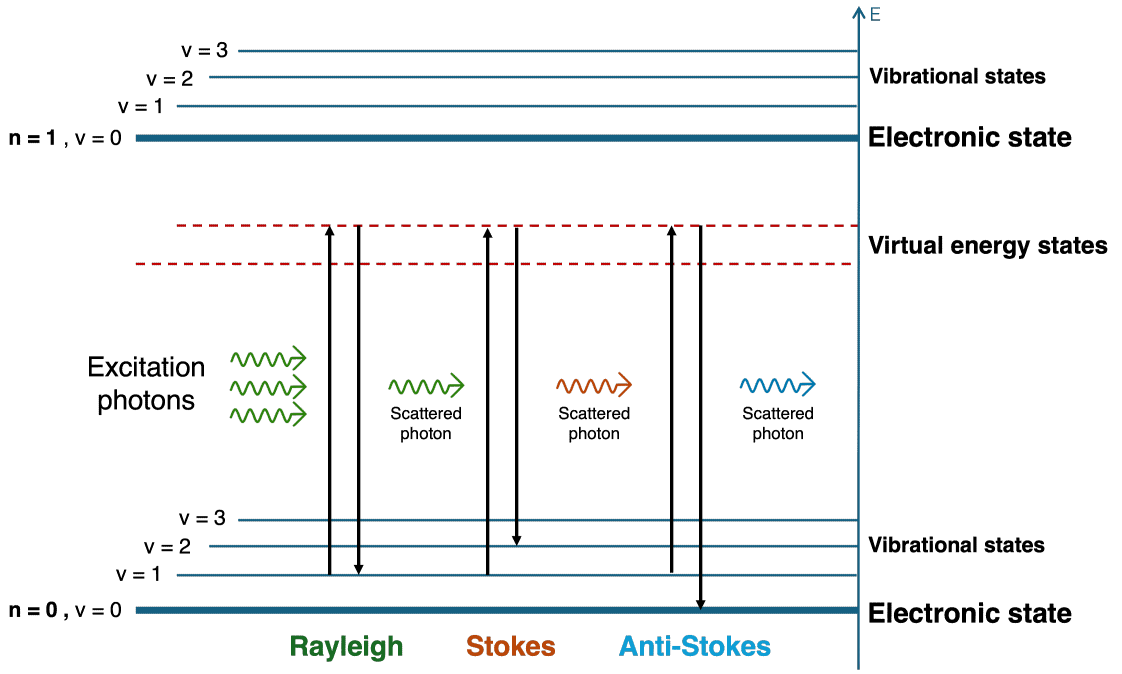

Figure 2.14: Simplified sketch of non-resonant Raman scattering mechanisms.

in polarizability. However, the classical electromagnetism approach leads to some predictions that are not observed experimentally. For example, in real-world cases, the intensity of Anti-Stokes (AS) lines is typically lower than that of Stokes (S) lines, a result not accounted for by classical theory. The quantum mechanical treatment of the Raman effect offers a more detailed understanding of the phenomenon. This approach can be explained within a single-particle framework. Figure 2.14 illustrates this for the case of nonresonant scattering, where the energy of the incident photon is lower than the energy gap between the ground state and the first excited state. When a photon with energy $\hbar\omega_1$ interacts with the system (such as a molecule or crystal), the system initially is excited from its ground state to a virtual state. This virtual state is represented by a dashed line and does not correspond to a well-defined energy level. The system then has a transition from this virtual state to a final stationary state. When the vibrational energy level of the molecule is increased during the scattering process, the final state of the molecule is in a higher vibrational state (*e.g.*, from $|n = 0, v = 1\rangle$ to $|n = 0, v = 2\rangle$). In this case, the scattered photon has less energy than the incident photon, resulting in a scattered photon with energy $\hbar\omega_S$ that is lower than the incident photon energy $\hbar\omega_1$. This type of scattering is the Stokes process, as illustrated in the middle part of Figure 2.14. If the vibrational energy level of the molecule is decreased during the scattering process, the final state of the molecule is a lower vibrational level (*e.g.*, from $|n = 0, v = 1\rangle$ to $|n = 0, v = 0\rangle$). In this situation, the scattered photon has more energy than the incident photon, resulting in a scattered photon energy $\hbar\omega_S$ that is higher than the incident photon energy $\hbar\omega_1$. This type of scattering is the Anti-Stokes process, as illustrated in the right part of Figure 2.14. The virtual absorption involved in this process is not a true energy absorption because the virtual state does not correspond

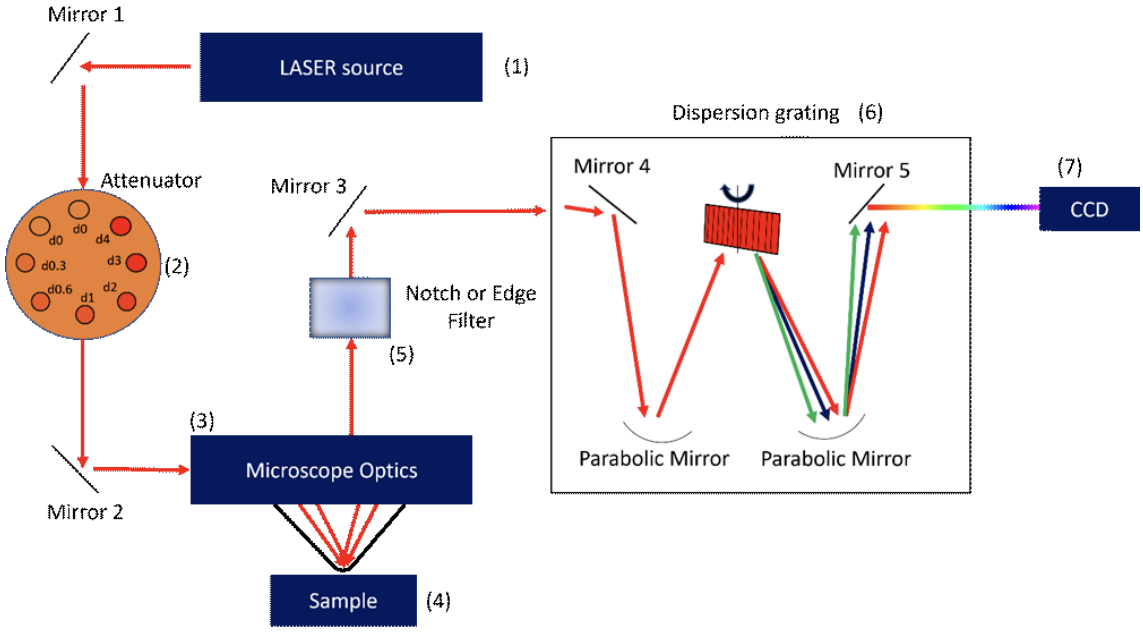

Figure 2.15: Schematic of the configuration of the Raman setup with its key components. [104]

to a stable energy level. The lifetime of this virtual, metastable state is extremely short, typically on the order of 10^{-15} to 10^{-16} seconds. The quantum mechanical approach leads to two essential conditions for observing the Raman effect: (i) at least one non-zero element in the polarizability tensor derivative, and (ii) a change in the vibrational quantum number such that $v_{f_k} = v_{i_k} \pm 1$, meaning the vibrational quantum number must differ by 1 between the initial and final states.

The Raman characterization of nanoparticle SCs was conducted at room temperature (RT) using an automated and integrated confocal microRaman spectrometer, specifically the XploRA Plus from HORIBA Scientific. This system was equipped with an Olympus microscope BX43 and featured the following components, as illustrated in the sketch reported in Figure 2.15:

1. **Laser Source:** The system employs diode lasers at 2.33 eV - 100 mW, 1.94 eV - 90 mW, and 1.58 eV - 100 mW used to excite the system.

2. **Attenuator:** Light intensity is controlled using wheels of neutral density filters with different optical densities, which scale the power logarithmically.

3. **Microscope Optics:** The laser beam is focused on the sample using objectives with different magnifications of 10x, 20x, 50x, and 100x. Two 50x objectives can be employed: standard and LWD.

4. **Sample Holder:** The sample is placed on a motorized stage that allows movement in any direction and includes coarse and fine focus adjustments.

5. **Filter:** After scattering, the light passes through a filter band-blocking (notch)

or long-pass (edge) to cut the Rayleigh line (notch filter) or the Rayleigh and Anti-Stokes lines (edge filter).

6. **Dispersion Grating:** The light is dispersed into different wavelengths by a grating with either 600 lines/mm or 1800 lines/mm, following Bragg's law.

7. **CCD Detector:** The scattered light is detected by an Open Electrode CCD camera, which was equipped with a multistage Peltier air-cooling system, allowing for simultaneous detection of dispersed wavelengths.

8. **Software:** The Horiba LabSpec software manages integration times, averaging, and post-processing of the spectra.

Chapter 3

Measurement Results & Discussion

This chapter reports on the experimental measurement conditions, the data analysis methodologies, and the obtained results of the time-resolved and steady-state optical characterization of $CsPbBr_3$@PPG-PEAsupracrystals (SC)s. Section 3.7, at the end of this chapter, focuses on the discussion of the results.

3.1 TAS Measurements

Transient Absorption Spectroscopy (TAS) measurements start with the system calibration. This involves aligning the pump and probe beams to ensure spatial overlap at the sample position, as well as determining the "time zero" point. Time zero refers to the point at which the pump and probe pulses spatio-temporally overlap and it serves as a reference for all subsequent time delay measurements. To find time zero, the time delay line is gradually adjusted while monitoring the Transient Absorption (TA) signal. Since no pump-probe signal is present at negative time delays, switching from negative to positive delays allows time zero to be identified as the point at which the TA signal first emerges. Prior to this point, the signal remains equal to zero within the noise level. Once the time zero was set in this way, software calibration was performed to ensure that all measurements were analysed under the same experimental conditions. Time zero was then set for all measurements as the point at which the signal, normalized between 0 and 1, reaches the 0.5 value with a negative derivative.

Data acquisition is controlled via the HARPIA software, which facilitates real-time monitoring and adjustment of the experimental parameters. The software allows to control key settings such as the pump-probe delay, chopper frequency, and sample position, while simultaneously displaying the pump-probe map and TA spectra. During the measurements, the HARPIA system collects a series of spectra that are used to calculate the differential absorption signal. These spectra include Background Signals (without probe pulse) and Full Signals (with probe pulse) and

are the following four:

1. Background signal with pump pulse reaching the sample $I^{\text{bckg}}_{\text{pumped}}(\lambda)$,
2. Background signal without pump pulse reaching the sample $I^{\text{bckg}}_{\text{not pumped}}(\lambda)$,
3. Full signal with pump pulse reaching the sample $I_{\text{pumped}}(\lambda)$,
4. Full signal without pump pulse reaching the sample $I_{\text{not pumped}}(\lambda)$.

After collecting them, the system computes the spectra to estimate the light-induced and time-dependent absorption changes occurring in the system. Specifically, it subtracts the background signals (1-2) from the full signals (3-4) and subsequently computes the log_10 of the ratio between the resulting unpumped spectra and the pumped spectra. The relationship between the transmitted intensity $I(\lambda)$ and the absorbance $A(\lambda)$ is given by the Lambert-Beer law, according to which the spectral intensity of the probe pulse passing through an absorbing medium can be expressed as

$$I_0(\lambda) = I(\lambda) \cdot 10^{-A_0(\lambda)}, \tag{3.1}$$

where $I_0(\lambda)$ is the light outgoing from a non-photoexcited system, $I(\lambda)$ is the intensity of the incident probe, and $A(\lambda)$ is the absorbance at wavelength λ. In a photo-excited system spectral absorbance changes (and it is likewise dependent on time). Therefore, the intensity of the probe pulse at delay t after excitation by the pump pulse can be expressed as

$$I_1(\lambda, t) = I(\lambda) \cdot 10^{-A_1(\lambda,t)}, \tag{3.2}$$

where $I_1(\lambda, t)$ is the outgoing light from a photoexcited system at the time t, $I(\lambda)$ is still the incident probe intensity and, $A_1(\lambda, t)$ is the absorbance at wavelength λ and time t. Since the interest lies in $A_1 - A_0$, using Equation 3.1 and Equation 3.2, the following expression is obtained:

$$\Delta A = A_1 - A_0 = \log_{10}\left(\frac{I_0}{I_1}\right), \tag{3.3}$$

where:

$$A_0(\lambda) = -\log_{10} I_0 + \log_{10} I(\lambda), \tag{3.4}$$
$$A_1(\lambda, t) = -\log_{10} I_1(\lambda, t) + \log_{10} I(\lambda). \tag{3.5}$$

Therefore, by measuring and collecting I_0 and I_1 over a series of temporal delays $t = t_1, t_2, \ldots, t_M$ between the two pulses, the full time-resolved TA spectrum can be obtained, providing direct access to the spectral absorbance changes over the time

t. The spectrum is calculated in terms of dimensionless optical density (OD) units as:

$$\Delta\mathrm{OD}(\lambda,t) = A_1(\lambda,t) - A_0(\lambda,t) = -\log_{10}\left(\frac{I_1(\lambda,t)}{I_0(\lambda,t)}\right), \tag{3.6}$$

where $I_0(\lambda)$ is the intensity of the probe pulse without the pump, and $I_1(\lambda,t)$ is the intensity of the probe pulse after the pump at delay t.

In the following, $I_0(\lambda,t)$ will be referred to as $I_{\text{not pumped}}(\lambda)$, and $I_1(\lambda,t)$ as $I_{\text{pumped}}(\lambda,t)$. By subtracting the appropriate background signals from the full signals, the difference absorption, is calculated in terms of difference Optical Density as

$$\Delta\mathrm{OD}(\lambda,t) = \log_{10}\left(\frac{I_{\text{not pumped}}(\lambda,t) - I^{\text{bckg}}_{\text{not pumped}}(\lambda)}{I_{\text{pumped}}(\lambda,t) - I^{\text{bckg}}_{\text{pumped}}(\lambda)}\right). \tag{3.7}$$

The resulting dimensionless difference absorption spectrum, $\Delta\mathrm{OD}(\lambda,t)$, is typically of the order of 0.001 or less. Thus, the signals are often multiplied by a factor of 1000 for better visibility. The scaled measurable is indicated as

$$\mathrm{mOD}(\lambda,t) = 1000 \times \Delta\mathrm{OD}(\lambda,t). \tag{3.8}$$

Another (complementary) way to express the differential absorbance signal is in terms of the dimensionless differential transmission:

$$\frac{\Delta T}{T}(\lambda,t) = \frac{I_{pumped}(\lambda,t) - I_{notpumped}(\lambda,t)}{I_{notpumped}(\lambda,t)} = 10^{-\Delta OD(\lambda,t)} - 1. \tag{3.9}$$

By measuring difference absorption signals at various time delays t the entire time-resolved difference absorption spectrum can be plotted as a function of both probe energy range, producing a two-dimensional (2D) map. This 2D map is a valuable tool for visualizing the temporal evolution of excited states and provides insights into excited-state lifetimes, energy transfer mechanisms, and other dynamic processes.

TAS measurements were performed with a pump energy of 3.02 eV and a probe energy distribution spanning from 1.46 eV to 2.82 eV. A representative spectrum of the probe, optimized in the visible region, is shown in Figure 3.1.

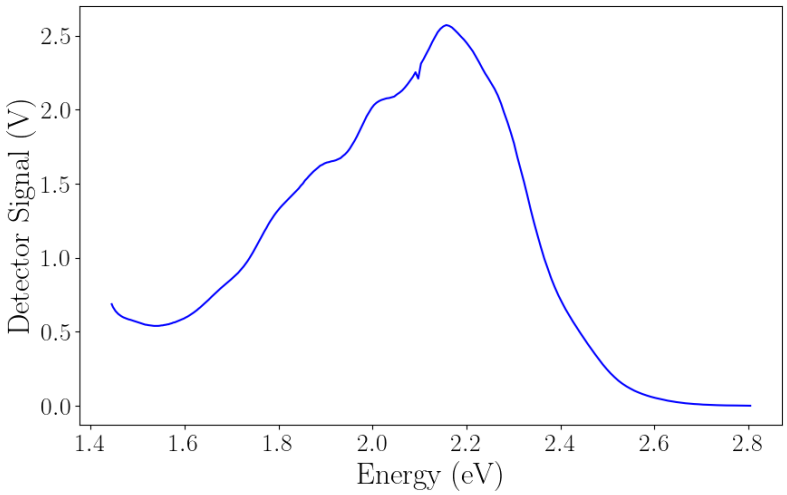

Figure 3.1: Representative probe spectrum showing the detector signal, in volts (V), as a function of energy (eV) in the visible range. The detector signal corresponds to the voltage output from the detector in relation to the light intensity at each radiation energy.

3.2 TAS Analysis & Results

This section presents the results of Transient Absorption Spectroscopy (TAS) measurements of $CsPbBr_3$@PPG-PEA Supracrystals (SCs). Specifically, two types of measurements were performed: fluence dependence, described in subsection 3.2.1, and 2D maps for the full time-resolved absorption spectra, described in subsection 3.2.2.

3.2.1 Fluence Dependence

Fluence dependence allows to understand how the transient absorption response of the samples changes as pump fluence increases. The goal of the fluence dependence measurement is to find the fluence range within which the system responds linearly to an increase in the electric field and does not exhibit photoinduced damage.

To further elaborate this concept, let's start from examining Maxwell equations. Under the influence of an electromagnetic wave, the electron within a material is brought to forced oscillations induced by the incident electromagnetic wave [105]. In the continuum framework, which is a valid approximation when the wavelength of the electromagnetic wave is much larger than the atomic scale, the material's response can be described as a superposition of the incident electric field **E** and the phase-shifted field generated by the oscillating electrons. This re-emitted field is called the induced electric polarization of the material, denoted by **P**.

Analysing the relationship between the polarization field and electric field through the susceptibility, under successive decompositions, the expansion is typically expressed as follows:

$$\mathbf{P} = \varepsilon_0 \left(\chi^{(1)}\mathbf{E} + \chi^{(2)}\mathbf{E}^2 + \chi^{(3)}\mathbf{E}^3 + \dots \right)$$

where: ε_0 is the vacuum permittivity, $\chi^{(1)}$ is the linear susceptibility, which describes the first-order response (linear polarization) of the material to the electric field, $\chi^{(2)}$ is the second-order susceptibility, corresponding to nonlinear effects such as three-wave mixing, which we harness in the TAS pump branch via Optical Parametric Amplification (OPA), $\chi^{(3)}$ is the third-order susceptibility, which governs higher-order nonlinear effects such as Self Phase Modulation (SPM) underpinning White Light Generation (TAS probe).

When investigating the physics of the samples, it is essential to ensure operations in a regime of linearity between the fluence driving the photoinduced process and the number of carriers generated. If non-linearities arise in this process, the extracted physics from the sample could be misleading. Thus, the goal of fluence dependence measurements is to ensure that we remain within this linear framework:

$$\mathbf{P} = \varepsilon_0 \chi^{(1)}\mathbf{E}$$

Fluence dependence measurements of the transient absorption signal were taken at two time delays: 1 ps and 10 ps. An average of 20 spectra were acquired for each fluence and time delay, obtained by averaging 5000 *pumped* and 5000 *unpumped* acquisitions. The laser system was operated at low fluences to avoid damaging the system. The laser operated with an average power of about 200 μW, measured at the arrival in the HARPIA sample region. Due to these low fluences, fluctuations of the laser system (approximately 10 μW over the average output power) particularly affected the reproducibility of the measurement over the 20 scans. Reductions in laser power resulted in a reduction of the signal-to-noise ratio.

The analysis was performed comparatively in two ways: first, I looked at the minimum of the signal and then I looked at the integrated area of the spectral traces in difference absorption, as a function of fluence, for both samples. The calculation of the minimum and integrated area of the signal was performed by averaging and calculating the standard deviation of only the scans with a higher signal-to-noise ratio. The error bars of these measurements are expressed as the standard deviation (σ) divided by the square root of the number of scans selected. Following this, a linear fit of the data points was performed for both the minimum and integrated area trends using a Python script in a Jupyter Notebook. In `scipy.optimize.curve_fit`, the algorithm used to determine the optimal fit parameters is based on non-linear least squares [106]. By default, `curve_fit` employs the Levenberg-Marquardt algorithm, which is an effective method for solving non-linear least squares problems [106].

With this approach we ascertain that the sample can be excited in absence of non-linear phenomena, such as multi-photon absorption, or photoinduced damage onto the sample. The fluence dependence results are presented in Figure 3.2. Data for MS0864 (panels a and b) and MS0865 (panels c and d) are reported for 1 ps and

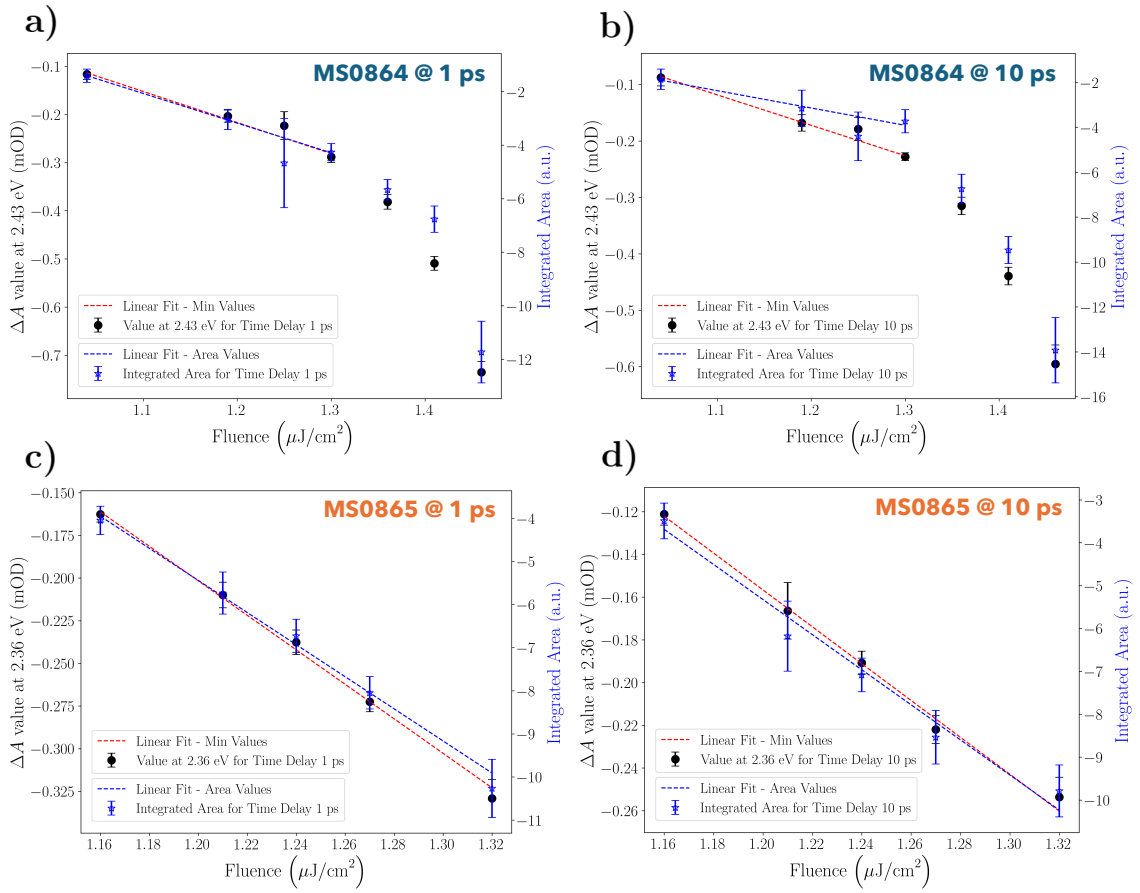

Figure 3.2: Fluence dependence results for MS0864 (panels a, b) and MS0865 (panels c, d) for the two fixed time delays: 1 ps and 10 ps, respectively. In each panel, the trends of the pump-probe signal minimum (black dots) and the integrated area (blue stars) are shown as a function of fluence in $\mu J/cm^2$. The red line represents the linear fit for the minimum values "min values"), while the blue line corresponds to the linear fit for the integrated area values "area values").

10 ps, respectively. In each panel, the trends of the pump-probe signal minimum at 2.43 eV for MS0864 and 2.36 eV for MS0865 (black dots), and the integrated area (blue stars) are shown as a function of fluence in $\mu J/cm^2$. Each trend is fitted using a linear function where the red line represents the fit for the minima values ("*min values*") and the blue line corresponds to the fit for the integrated area values ("*area values*"). Fluence dependence measurements revealed a comparable linearity ranges for both samples, spanning from 1 to 1.32 $\mu J/cm^2$. This linearity remains consistent across both samples and time delays. In this range, both the minimum values and the integrated area of the pump-probe signal show linear trends.

The two methods show strong consistency within the linearity regime. The following pump-probe measurements were conducted exclusively within the linear regime indicated in Figure 3.2. The discrepancy in the slope shown in Figure 3.2, panel b, is likely due to the low signal-to-noise ratio caused by the sample's dilution on the grid. Despite this, the linearity is preserved within the two methodologies.

3.2.2 2D maps: full time-resolved absorption spectra

After measuring the fluence dependence, the second experiment involved acquiring a complete two-dimensional (2D) map of the sample's response in terms of both radiation energy and time (see Equation 3.7). The system's photoinduced response was sampled from -1 ps to 1 ns, with smaller time steps (ranging from 20 to 70 fs) during the first few picoseconds after the pump arrival, thus focusing on the ultrafast response regime. To improve the signal-to-noise ratio, about 10 TA acquisitions per dataset were collected consecutively. The system was pumped with a pump fluence within the linearity range of fluence dependence.

Three datasets were acquired for the analysis: one for sample MS0864 and two for MS0865. Two datasets for MS0865 were necessary to quantify the morphologically dependency of the sample response. Analyzing localized differences in material properties - reflected in variations of the TA spectra at different sample locations - is essential to understanding how local arrangement, packing, and order/disorder correlations are influenced by the role of ligands. Variations in the photoinduced response at different points would suggest localized differences in material properties driven by the degree of heterogeneous morphological distribution. The analysis of TAS data was performed using Python scripts and third-party software tools like OPTIMUS. Specifically, both chirp correction and Global Lifetime Anlysis (GLA) of the pump-probe maps were conducted using OPTIMUS.

A preliminary energy calibration was performed in Python which was conducted by identifying the 1.51 eV laser line in the spectra. This line appeared because the pump energy was 3.02 eV, and it was generated in the OPA by taking the second harmonic of a 1.51 eV pulse. The laser line appeared in the spectra due to an incomplete background subtraction. Since the laser line is particularly intense in the spectral traces, it is easily detectable. If there are energy shifts caused by improper calibration of the gratings within the spectrograph, the laser line will also shift, appearing at spectral regions different from the pump pulse's generating energy (1.51 eV). Therefore, the spectral calibration error can be easily computed, and the entire spectrum can be shifted by the difference between the measured peak energy and the actual energy of the laser line (*i.e.*, 1.51 eV).

In the collected spectra, the supercontinuum probe pulse was not compensated for chirp, which refers to the temporal delay between different spectral components of an ultrafast laser pulse. This resulted in an energy-dependent time-zero shift in the recorded signals, caused by group velocity dispersion and self-phase modulation [107]. These effects result in a distortion of the signal in time, making it necessary to correct the TA maps during post-processing, a process referred to as "chirp correction" which was conducted in OPTIMUS. The software models the time-zero shift as a function of wavelength using a polynomial function [107],

$$c(\lambda) = c_0 + \sum_{i=1}^{n} c_i \left(\frac{\lambda - \lambda_c}{100} \right)^i , \tag{3.10}$$

where $c(\lambda)$ is the time-zero position at wavelength λ, c_0 is the time-zero at the central wavelength λ_c, and the polynomial terms c_i represent the wavelength dependence. Therefore, the chirp correction is performed by compensating for the time-zero shifts at each wavelength by an amount equal to $c(\lambda)$.

OPTIMUS was also employed to conduct Global Lifetime Analysis (GLA). The pump-probe time traces at each wavelength $S(t)$ in the 2D map are simultaneously fitted with a sum of exponential functions, convoluted ($\otimes$) with a Gaussian instrument response function (IRF) [107, 108], defined as cross-correlation width of the pump and probe pulses [107]. The pump-probe time traces are mathematically expressed as

$$S_\omega(t) = \sum_{i=1}^{n} A_i(\tau_i, \omega) \cdot e^{-\frac{t}{\tau_i}} \otimes \mathrm{IRF}(t). \tag{3.11}$$

In Equation 3.11, $A_i(\tau_i, \omega)$ represents the frequency-dependent amplitude of the exponential decay associated with the time constant τ_i.

The GLA method is advantageous for efficiently fitting all probe energies simultaneously, yielding global time constants for the system. However, it may not fully capture potential coherent responses, such as lattice oscillations, and may not necessarily give all the information on the exact behaviour of the electronic transitions in the probe region. For this reason, additional Jupyter notebooks containing Python scripts were developed to analyze the chirp-corrected 2D maps, as well as to examine the one-dimensional (1D) traces at specific radiation energies or time delays.

Once the 2D maps are obtained, an analysis of the possible coherent response of these systems can be performed by taking cuts along the energy axis and observing the behaviour of the TA signal over time. A coherent response typically manifests as an oscillation of the pump-probe signal over time, where the oscillation frequency corresponds to that of active Raman phonons, if present. To detect oscillations of the order of meV, very high temporal resolutions (achieved by the short pulse duration) and a good signal-to-noise ratio are required. When fitting the entire signal response with a sum of exponentials, as in Equation 3.11, only the incoherent response is captured, meaning the fit does not account for any oscillatory behavior. Therefore, if coherent oscillations are present, they should become evident by examining the residuals from the fit. These residuals will show oscillations, as the deviations are primarily caused by coherent dynamics that are not captured by the exponential fit of the incoherent trend. The frequency of the coherent response can be investigated by applying a Fast Fourier Transform (FFT) to the residuals thanks to built-in libraries such as `scipy.fftpack: rfftfreq, rfft`. To increase the Signal-to-Noise Ratio (SNR) of the monodimensional traces such as FT traces, multi-energy binning, zero-padding method and Kaiser-Bessel windowing were also applied [109, 110].

Consistently with the scope of this work, exposed in chapter 1 and with the sample layout in Figure 2.5, I will now elaborate on the data obtained experimentally.

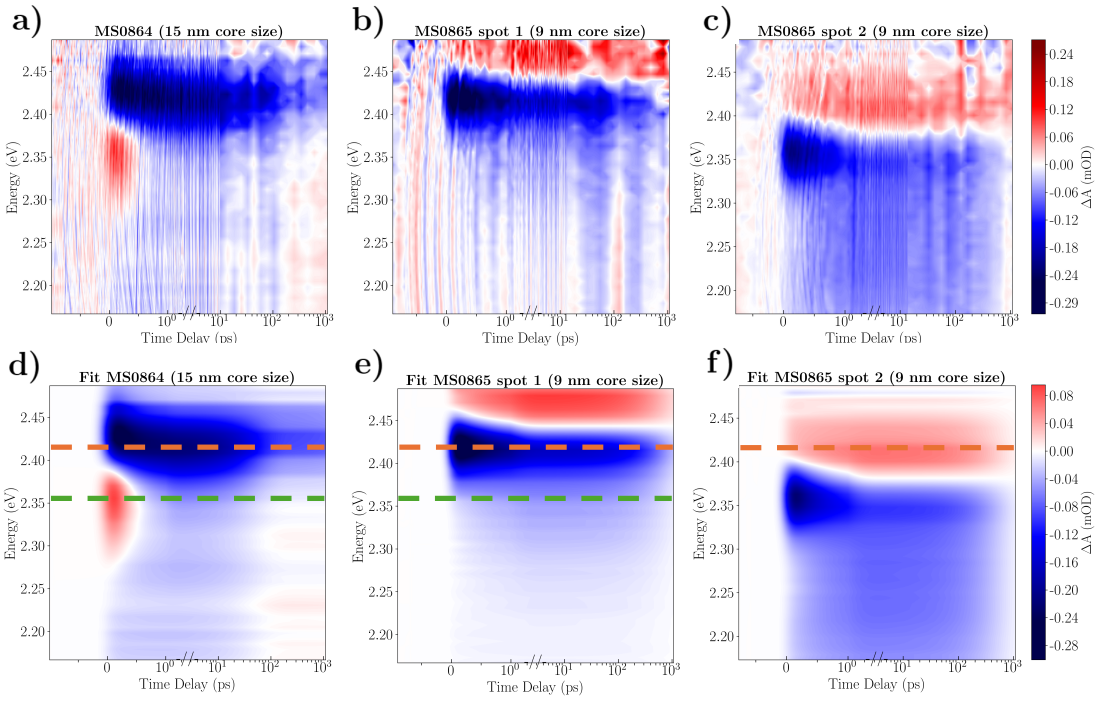

Figure 3.3: Experimental and Fitted 2D maps obtained from OPTIMUS for MS0864 (a, d), MS0865 spot 1 (b, e), and MS0865 spot 2 (c, f). Each map illustrates the transient absorption signal (ΔA) as a function of both energy (eV) and time delay (ps). The experimental 2D maps (a-c) are shown alongside the corresponding fit (d-f). All 2D are plotted in a linear-log_{10} scale, with the threshold between linear and logarithmic set at 1 ps along the time delays (x-axis). At the bottom of the figure, the legend for the dashed lines is provided. These represent the energy cuts taken at strategic points on the 2D maps to observe the time-resolved trace of the pump-probe signal, as shown in the corresponding Figure 3.6 and Figure 3.7, respectively.

Chirp-corrected 2D maps from MS0864 and MS0865 are shown in Figure 3.3 (a-c), along with their corresponding 2D fits (d-f). As discussed in section 2.1, for MS0865 data I investigated two regions: Spot 1 (Figure 3.3, b) and Spot 2 (Figure 3.3, c). The first one has a heterogenous morphological distribution similar to that of the MS0864 (Figure 3.3, a) while the second represents a bulk-like area. In the following, I shall provide a general overview of the spectral changes. My analysis will unfold in two separate instances:

1. a comparative analysis at a fixed core size, focusing on the heterogeneous morphological distribution of the sample at the supracrystal level. I will report the result of TAS through a comparison in between MS0865 spot 1 (Figure 3.3, b) and MS0865 spot 2 (Figure 3.3, c);

2. a comparison of the signals between the MS0864 (15 nm core samples) and MS0865 spot 1 (9 nm core samples), obtained by two sample regions in which the supracrystal morphology is almost equal but the core size varies.

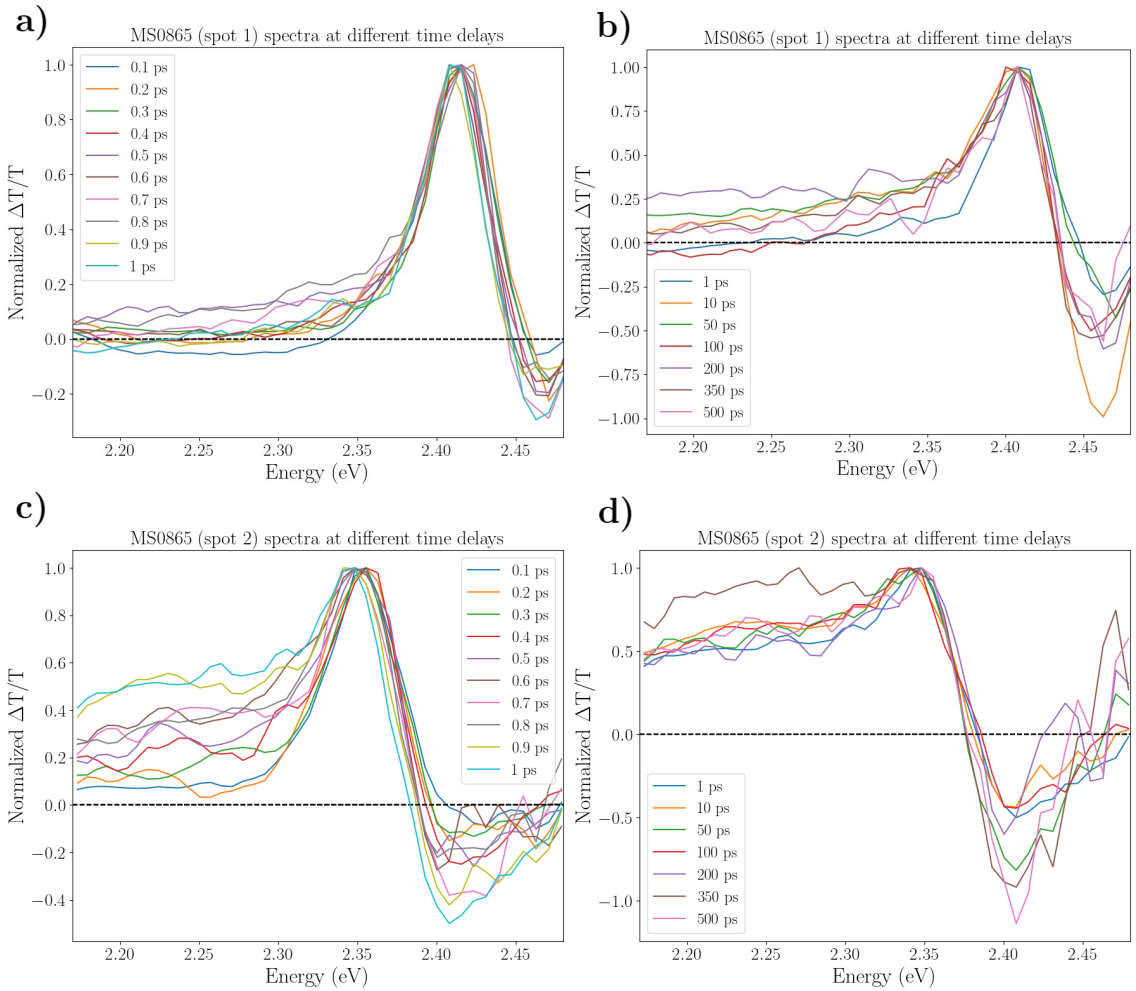

Figure 3.4: Transient absorption spectra ($\Delta T/T$) for MS0865 at different time delays. Panels (a) and (b) show the spectra for spot 1, while panels (c) and (d) show the spectra for spot 2. In panels (a) and (c), the early time delays (from 0.1 ps to 1 ps) are presented, while panels (b) and (d) display the spectra for longer time delays (from 1 ps to 500 ps).

Mesoscale heterogeneity dependence

Firstly, I report on the analysis of the spectral differences between MS0865 spot 1 and spot 2 within the same sample. To better observe such differences, cuts are taken at different time delays to examine the behaviour of the signal as a function of energy and time. Passing from difference absorption signal to normalized differential transmission (ΔT/T) with Equation 3.9, Figure 3.4 shows the evolution of the differential transmission during time for both ultrafast (< 1 ps) and longer timescales in both samples. The following key differences are observed:

1. Spot 1 shows a photoinduced bleach (Photobleach (PB)) ($\Delta A < 0$) signal confined in the 2.36 eV - 2.45 eV spectral region, with an absolute minimum value centered around 2.41 eV. Spot 2 exhibits a PB in the region between 2.32 eV and 2.38 eV, red-shifted of about 0.6 eV with respect to spot 1;

2. The PB in MS0865 spot 2 persist up to 2.17 eV while no PB feature is detected below 2.38 eV for spot 1.

Therefore, findings hint to a connection in between the signal redshift and the packing of the nanocrystals at the mesoscale level.

Core size dependence

The spectral and time-resolved response differences between MS0864 and MS0865 suggested by the data are:

1. MS0864 exhibits an ultrafast Photoinduced Absorption (PIA) in the 2.30 eV - 2.38 eV spectral region, temporally confined into the first 0.5 ps, which is not observed in MS0865;

2. MS0864 shows a recovery to the ground state out of the time range of our experiments (1 ns), while in MS0865 the recovery is almost complete.

These features can be better observed and understood by looking at the mono-dimensional traces obtained from the 2D map cuts at different time delays. Figure 3.5 presents a comparison of the normalized transmission difference between two datasets, MS0864 and MS0865 spot 1, alongside digitized TAS spectra of a crystalline $CsPbBr_3$ thin-film reported in *Butkus et al.* [111]. The $CsPbBr_3$ film (Figure 3.5, a) exhibits three clear spectral features: i) a dominant positive PB ($\Delta T/T > 0$), ii) a broad PIA_1 ($\Delta T/T < 0$) above the bandgap (2.43 eV - 2.48 eV), iii) a short-lived (less than 1 ps) PIA_2 ($\Delta T/T < 0$) at energies just below the band gap (2.30 eV - 2.38 eV). Comparing these three spectral features with our findings, we observe that the peak of the central PB signal ($\Delta T/T > 0$) is consistent with those reported in this work, for both samples. Instead, two clear and nearly complementary differences are observed regarding the PIA ($\Delta T/T < 0$) signals:

1. MS0864 shows PIA between 2.30 eV and 2.38 eV but does not show PIA between 2.43 eV and 2.48 eV;

2. MS0865 spot 1 shows PIA between 2.43 eV and 2.48 eV; but lacks PIA between 2.30 eV and 2.38 eV.

Therefore, the ultrafast photoinduced absorption signal seems to disappear as the core size of the nanocrystals decreases. This is further confirmed by the time traces presented in Figure 3.6. By taking energy cuts, such as those shown in green in Figure 3.3 at 2.37 eV, it is even more evident that in MS0864 a $\Delta A > 0$ signal is present within 1 ps after excitation, whereas in MS0865 this feature is absent.

Time scales and relaxation pathways

To investigate the time scales and relaxation pathways, and to understand how the two samples recover to the ground state along with their respective relaxation time constants, a global lifetime analysis (GLA) was performed. This means that for

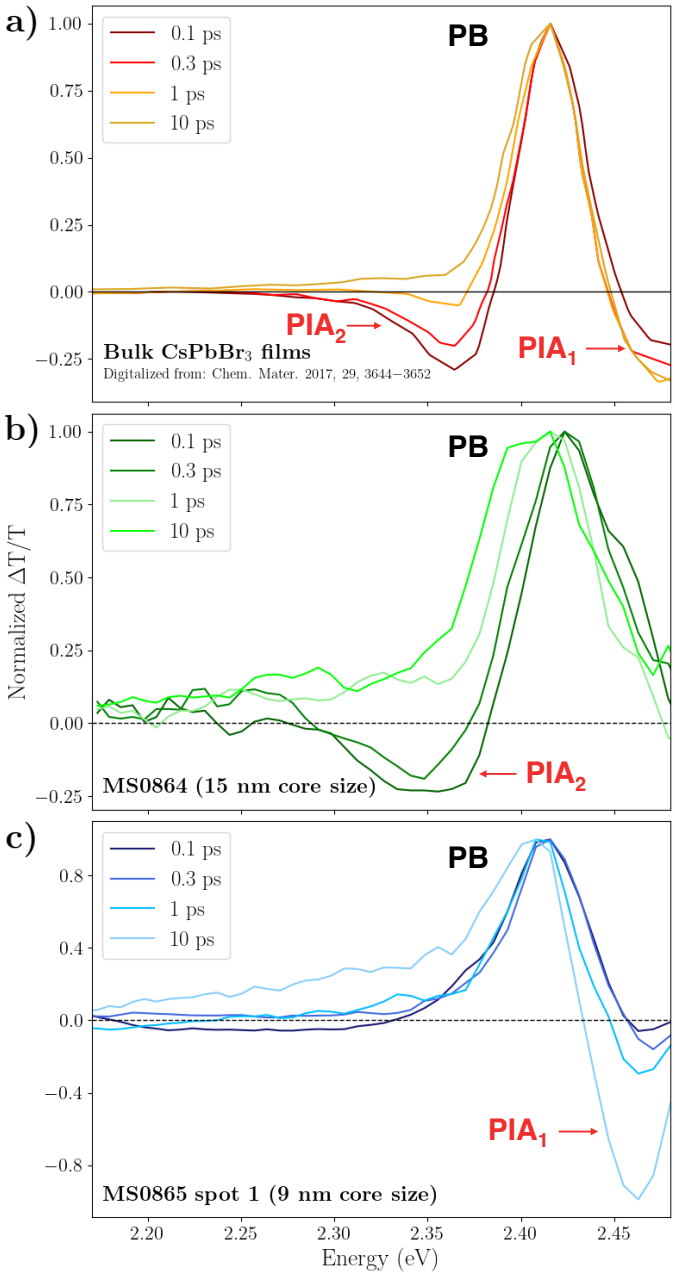

Figure 3.5: Normalized ($\Delta T/T$) transient absorption spectra for (a) bulk crystalline film (digitized from literature [111]), (b) MS0864 sample (15 nm core size), (c) MS0865 sample, spot 1 (9 nm core size). Each panel contains four spectra acquired at time delays of 0.1 ps, 0.3 ps, 1 ps, and 10 ps.

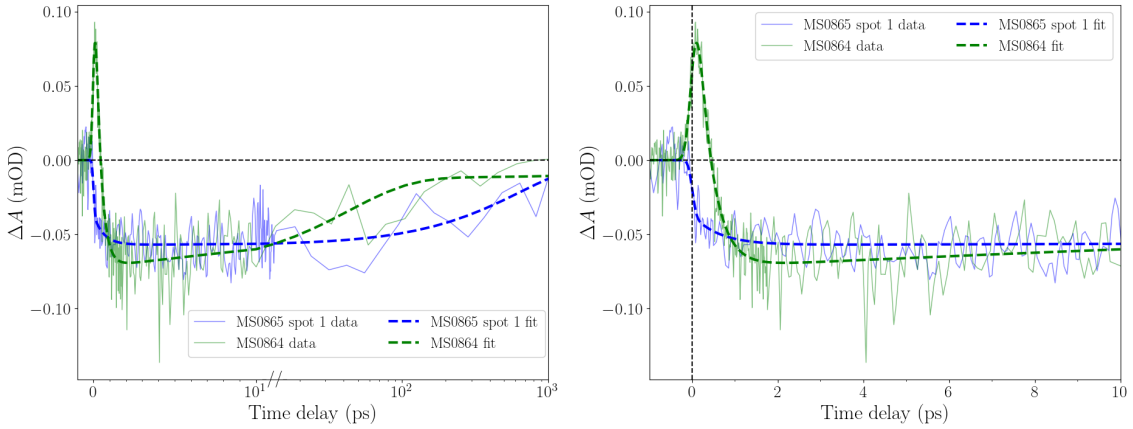

Figure 3.6: Transient absorption (ΔA) signal (mOD) as a function of time delay (ps) for the energy-binned photoinduced absorption (PIA): 2.36 eV ± 0.01 eV for both MS0864 (green) and MS0865 spot 1 (blue). These energies correspond to the PIA signal minima observed in the experimental MS0864 2D map. The experimental data is shown as solid lines, while the corresponding fits are plotted as thicker, solid lines in the same colors. In panel a), the x-axis is presented on a linear-log_{10} scale, with a threshold set at 10 ps. In panel b), the x-axis is presented on a linear scale and only the early 10 ps of the time-resolved dynamics are shown.

each physical process involved in the carrier relaxation, it is possible to associate a time constant and "follow" the photoexcited carriers during the decay. Figure 3.3 (d-f) shows the GLA fits of the Two-Dimensional (2D) experimental pump-probe maps obtained using OPTIMUS [107]. The fits were obtained in OPTIMUS using the model described in Equation 3.11 with $n = 2$, meaning two-time constants were employed to fit the data reported in Figure 3.3 (a-c). For the MS0864 sample, an additional offset was included to better capture the signal behavior at longer time delays. Table 3.1 summarizes the obtained time constants. The time constants, τ_1 and τ_2, show a clear trend: both decrease as the Nanoparticle (NP) core size increases. Time constant 1 for all three samples shares the same error bars, as the uncertainty obtained from the fit is smaller than the pulse duration. Thus, the true limiting factor for the time resolution in the decay constants should be taken as the pulse duration itself. As discussed in subsection 2.3.1, the pulse exits from the PHAROS module with a duration of 170 fs, but after passing through dispersive media in the setup, the pulse undergoes temporal broadening, resulting in a duration

Table 3.1: Time relaxation constants founded via GLA.

	τ_1 (ps)	τ_2 (ps)	offset (ps)
MS0864 (15 nm core size)	0.34 ± 0.2	43 ± 17	3000
MS0865 (9 nm core size) spot 1	0.63 ± 0.2	659 ± 79	/
MS0865 (9 nm core size) spot 2	0.53 ± 0.2	456 ± 39	/

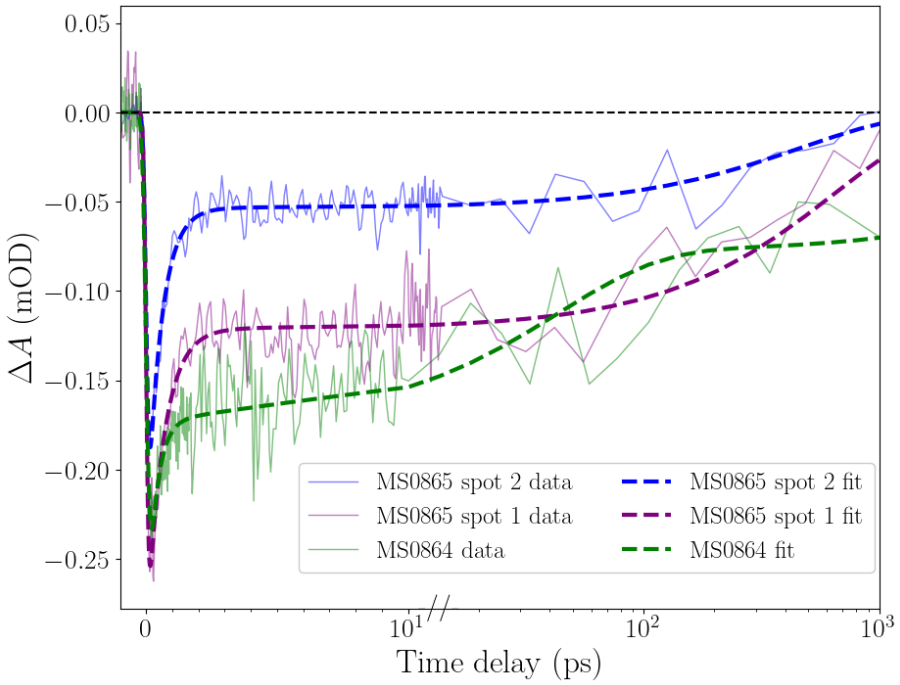

Figure 3.7: Transient absorption (ΔA) signal (mOD) as a function of time delay (ps) for the energy-binned PB maxima: 2.43 eV ± 0.01 eV for MS0864 (green), 2.42 eV ± 0.01 eV for MS0865 spot 1 (purple), and 2.36 eV ± 0.01 eV for MS0865 spot 2 (blue). These energies correspond to the PB signal maxima observed in the experimental 2D maps for each sample. The experimental data is shown as solid lines, while the corresponding fits are plotted as thicker, solid lines in the same colours. The x-axis is presented on a linear-log_{10} scale, with a threshold set at 10 ps.

of approximately 200 fs.

The fitting procedure allows one to examine time traces in specific spectral regions of interest by selecting cuts at key energies where significant features occur, like the PB signal maximum. In the experimental 2D maps (Figure 3.3 a−c), the PB maxima appear at 2.43 eV, 2.42 eV, and 2.36 for sample MS0864, MS0865 (spot 1) and MS0865 (spot 2), respectively. Figure 3.7 shows the temporal evolution of the transient absorption (TA) signal at the PB peaks for the three datasets: MS0864, MS0865 spot 1, and MS0865 spot 2, represented by green, purple, and blue traces, respectively. The plotted traces represent energy-binned data in a range of ± 0.01 eV around each energy of interest. This approach enhances the signal-to-noise ratio by averaging over a small spectral region, thereby improving data quality without losses in spectral selectivity. The thicker continuous lines represent the fitted curves, corresponding to the same energy cuts but obtained from slices of the fitted maps generated using OPTIMUS, Figure 3.3 (d-f). These fits show a good agreement with the overall trend of the TA signal over time. One point that needs to be emphasized is the justification for using an offset to adequately reproduce the behavior of MS0864, which, as mentioned, does not complete its recovery to the ground state within 1 ns. Additionally, the fit fails to capture the signal oscillations, which are primarily attributed to noise but could also be linked to the presence of coherent oscillations,

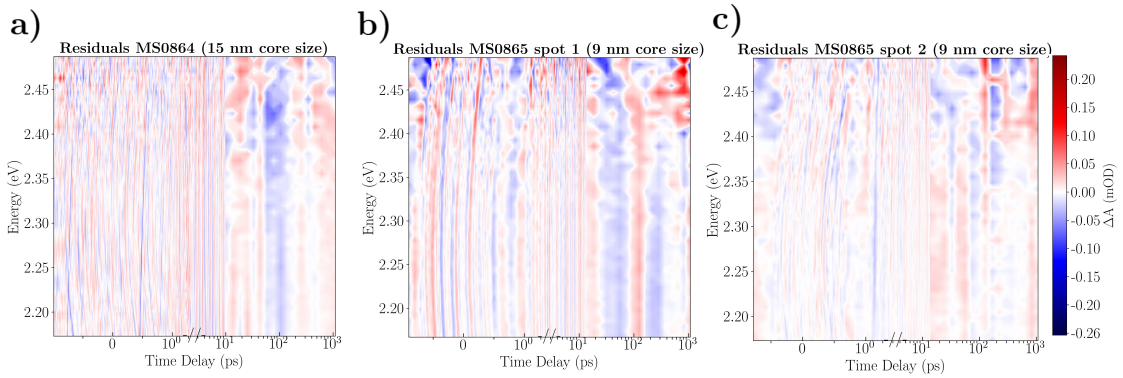

Figure 3.8: 2D maps of the Residuals obtained from the OPTIMUS fit of experimental 2D maps for MS0864 (a), MS0865 spot 1 (b), and MS0865 spot 2 (c). Each map illustrates the residuals of the transient absorption signal (ΔA) as a function of both energy (eV) and time delay (ps). All 2D maps are plotted in a linear-log_{10} scale, with the threshold between linear and logarithmic set at 1 ps along the time delay (x-axis).

as discussed in subsection 3.2.2. This latter statement requires further investigation and is included in the proposals for future research in this experimental work.

Residuals and Background

A good agreement between the 2D experimental maps Figure 3.3 (a−c) and the 2D fitted maps is shown in Figure 3.3 (d−f). Indeed, the 2D residuals maps (Figure 3.8 (a−c)) are essentially zero across all regions. As a validation that the observed signal in these results comes from the NPs and not from the empty grid, Figure 3.9 (a) shows the 2D chirp-corrected pump-probe map obtained for the empty grid. The color scale of the map indicates the magnitude of the signal, with different colors corresponding to positive (red) or negative (blue) changes in the difference absorption (ΔA). The empty grid 2D map exhibits no pump-probe signal under the experimental conditions used for the sample measurements. The map is mainly characterised by noise, with no distinguishable pump-probe signal features present. To demonstrate this, a cut of the 2D map at 2.37 eV, where a persistent negative signal up to 1 ns appears, was taken and plotted in Figure 3.9, b as a function of the time delay. The data in Figure 3.9, b are constant negative with an average of around -0.04 mOD. This behaviour is present even for negative time delays, confirming the absence of any multi-exponential trend in the empty grid signal. This behavior may arise from instrumental response or potential issues with detector calibration.

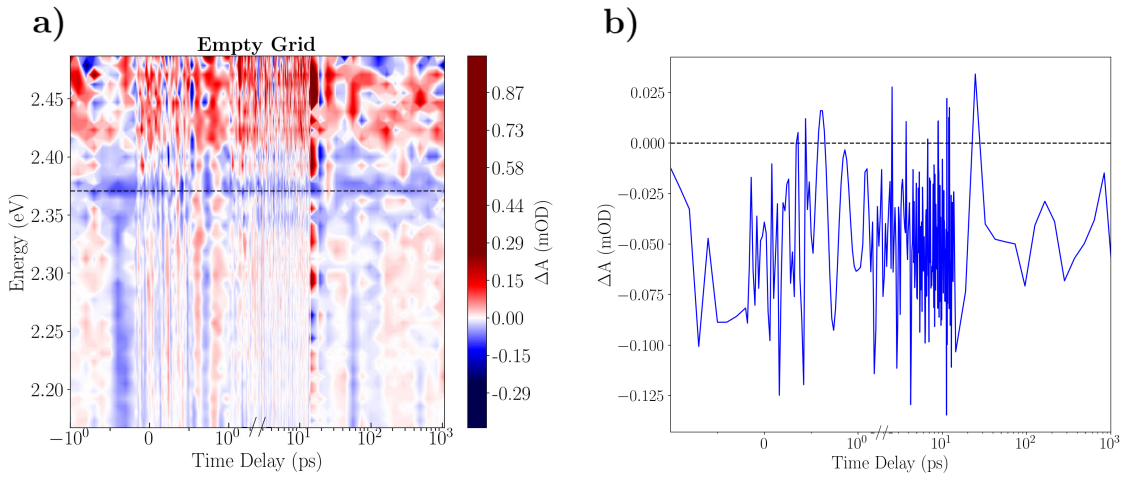

Figure 3.9: The empty grid transient absorption (ΔA) spectra are shown as a function of both time delay (ps) and energy (eV) in panel (a). In panel (b), a time trace is extracted from the 2D map at a fixed energy of 2.37 eV, displaying the ΔA signal as a function of time delay (ps) only. Both the 2D map and time trace are plotted in a linear-log_{10} scale, with the threshold between linear and logarithmic set at 1 ps along the time delay (x-axis).

3.3 Photoluminescence Measurements

Photoluminescence (PL) measurements were performed in the standard emission configuration, in which both samples and empty grid were excited with two distinct energies: 3.02 eV and 3.44 eV. The choice of 3.02 eV was dictated by the literature [112], while a preliminary excitation spectrum indicated greater emission at 3.44 eV.

For the 3.02 eV excitation, the emission spectrum (in wavelengths) was recorded from 430 nm to 700 nm, with 1 nm wavelength resolution. A total of 270 data points were acquired, each with an integration time of 0.2 s. For the 3.44 eV excitation, the emission spectrum was recorded (in wavelengths) from 380 nm to 690 nm, again with 1 nm wavelength resolution. A total of 310 data points were acquired, each having an integration time of 0.2 s.

One problem that arose during the measurements was the incompatibility between the sample compartment of the PL setup and our sample holder. To perform the measurements, the sample holder was manually adjusted in the sample chamber every time the sample had to be changed. This adjustment resulted in a loss of reproducibility of the measurements.

3.4 Photoluminescence (PL) Analysis & Results

The acquired emission spectra were imported into a Jupyter notebook for analysis using Python scripts. The spectra were first normalized to their integrated area. Then, the signal from the empty grid was subtracted for two reasons: first, it isolates the PL of the sample by removing any potential contributions from the

substrate, and second, it eliminates artifacts that appear in both the sample and empty grid spectra, specifically peaks associated with stray light scattering within the experimental setup.

After normalizing the spectra and isolating the sample signal, the emission data were converted from nanometers (nm) to electron volts (eV) using.

$$E\,(\mathrm{eV}) = \frac{hc}{e\lambda}, \tag{3.12}$$

where E is the photon energy in electron volts (eV), h is Planck's constant ($6.626 \times 10^{-34}\,\mathrm{J \cdot s}$), c is the speed of light in a vacuum ($2.998 \times 10^{8}\,\mathrm{m/s}$), e is the elementary charge ($1.602 \times 10^{-19}\,\mathrm{C}$), and λ is the wavelength in meters (m).

The PL peaks of the two samples were fitted using Voigt functions, using the `scipy.special.voigt_profile` function within the SciPy library. The centroids were extracted from the fits and the potential blue-shifts were evaluated. The Voigt profile, a convolution of Gaussian and Lorentzian, is approximated computationally rather than expressed as an integral. It captures both inhomogeneous (Gaussian) and homogeneous (Lorentzian) broadening mechanisms.

The Voigt profile is defined as

$$V(x;\sigma,\gamma) = \int_{-\infty}^{+\infty} G(x';\sigma)L(x-x';\gamma)\,dx', \tag{3.13}$$

where the Gaussian component is

$$G(x;\sigma) = \frac{1}{\sigma\sqrt{2\pi}} \exp\left(-\frac{x^2}{2\sigma^2}\right), \tag{3.14}$$

and the Lorentzian component is

$$L(x;\gamma) = \frac{\gamma}{\pi(x^2+\gamma^2)}. \tag{3.15}$$

In these expressions, σ represents the standard deviation of the Gaussian function (related to inhomogeneous broadening), and γ is the Full-Width Half Maximum (FWHM) of the Lorentzian function (associated with homogeneous broadening).

Figure 3.10 shows the photoluminescence (PL) emission spectra for both MS0864 (15 nm core, blue trace) and MS0865 (9 nm core, red trace), plotted as a function of the energy in eV. The excitation energies used for the PL experiments were 3.02 eV (Figure 3.10 a) and 3.44 eV (Figure 3.10 b), and the emission was probed in

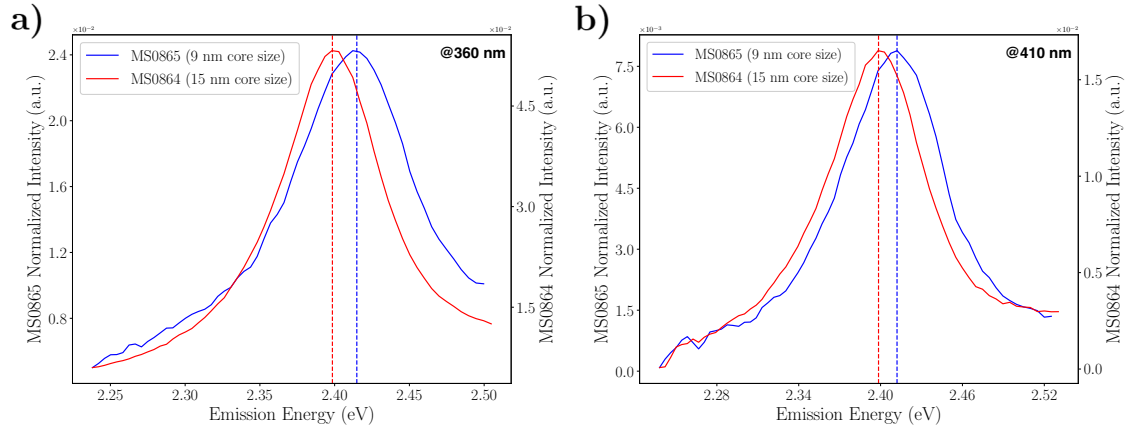

Figure 3.10: Photoluminescence peak emission spectra for MS0865 (9 nm core size, blue) and MS0864 (15 nm core size, red) under two different excitation energies: (a) 3.02 eV and (b) 3.44 eV. The emission energy (eV) is plotted along the x-axis, and the normalized intensity (a.u.) is plotted along the y-axes for each sample. The dashed vertical lines indicate the positions of the peak emission energies for both samples, illustrating the blue-shift observed for the smaller core size (MS0865) compared to the larger core size (MS0864).

the 2.22 eV - 2.54 eV range. Both panels, a and b, report a blue-shift in the PL emission peak upon decreasing the core size of the NPs from 15 nm to 9 nm.

To quantify this blue-shift, the centroids of both peaks for both excitation energies were calculated by fitting the emission peaks with a Voigt function, as seen in Equation 3.13. Figure 3.11 shows the results of the fit for MS0864 (red-dot traces in Figure 3.11, panels a-c) and MS0865 (blue-dot traces in Figure 3.11, panels b-d). Here the solid red and blue lines indicate the fitting functions, respectively. The error bars, obtained from the fit results, are displayed in three characteristic points: the tails and the central peak. An emission at $(2.397 \pm 3 \times 10^{-4})$ eV was found for MS0864 and $(2.410 \pm 5 \times 10^{-4})$ eV for MS0865 upon excitation at 3.02 eV. An emission at $(2.398 \pm 2 \times 10^{-4})$ eV was found for MS0864 and $(2.415 \pm 3 \times 10^{-4})$ eV for MS0865 upon excitation at 3.44 eV. Typically, PL emission peaks are expressed in terms of wavelength. Averaging together the results from both excitation energies, MS0864 and MS0865 PL emissions of approximately 517.15 $\pm$ 0.06 nm and 513.94 $\pm$ 0.09 nm were calculated. These results are in agreement with the literature [6]. The blue-shifts computed from the centroid values are: 13.74 $\pm$ 0.62 meV and 16.33 $\pm$ 0.37 meV, for 3.02 eV and 3.44 eV excitation energies, respectively.

3.5 Raman Measurements

Raman measurements were conducted at room temperature using the previously described micro-Raman spectrometer. Before each series of measurements, the system was calibrated and optimized to ensure high accuracy. Calibration was performed using a silicon standard to correct for any deviations or peak shifts due to instrument

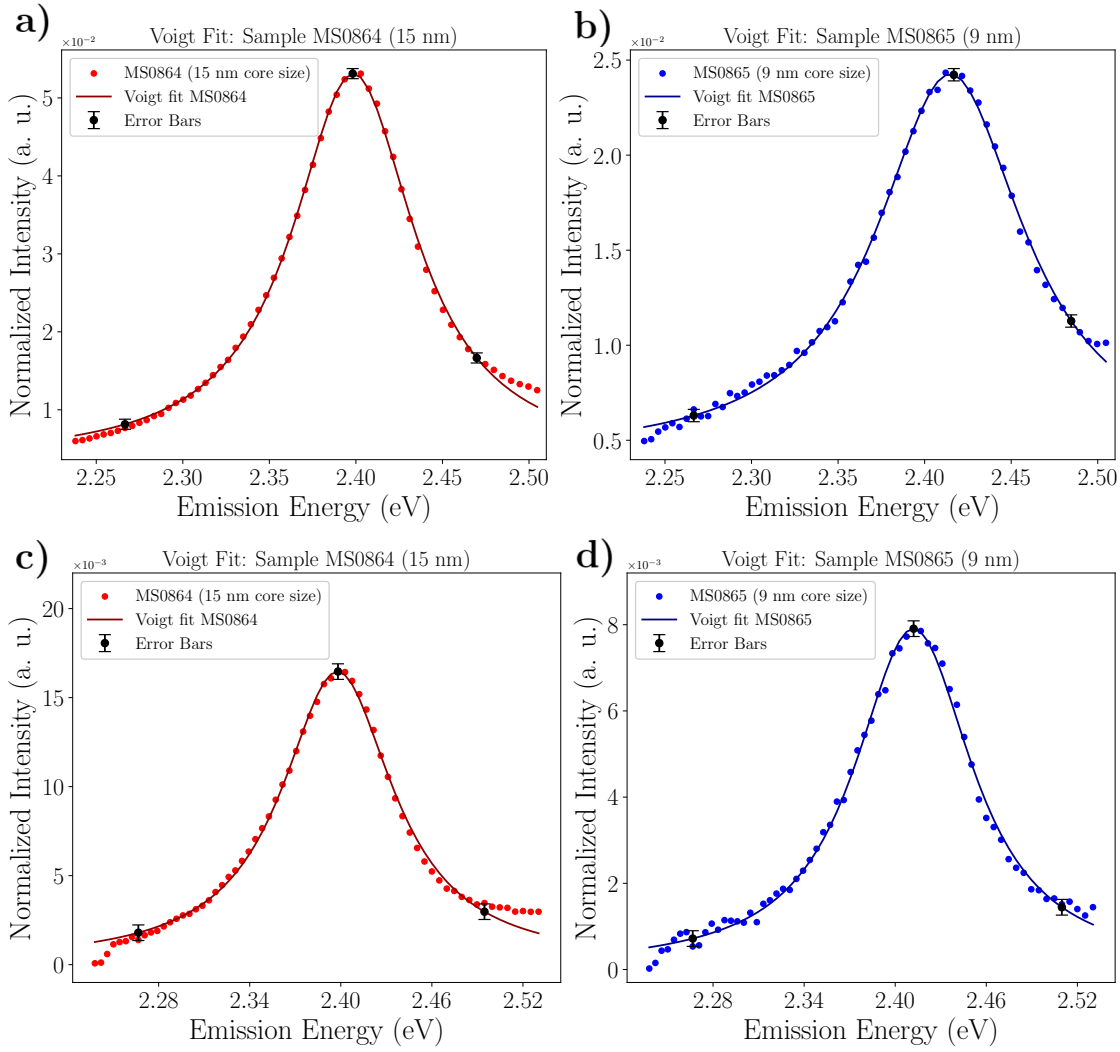

Figure 3.11: Voigt function fits of the emission peaks for both MS0864 and MS0865 with both 3.02 eV and 3.44 eV excitation energies. Panel a) and c) show the fit for the first sample under 3.02 eV and 3.44 eV of excitation energies, while panel b) and d) show the fits for the second sample.

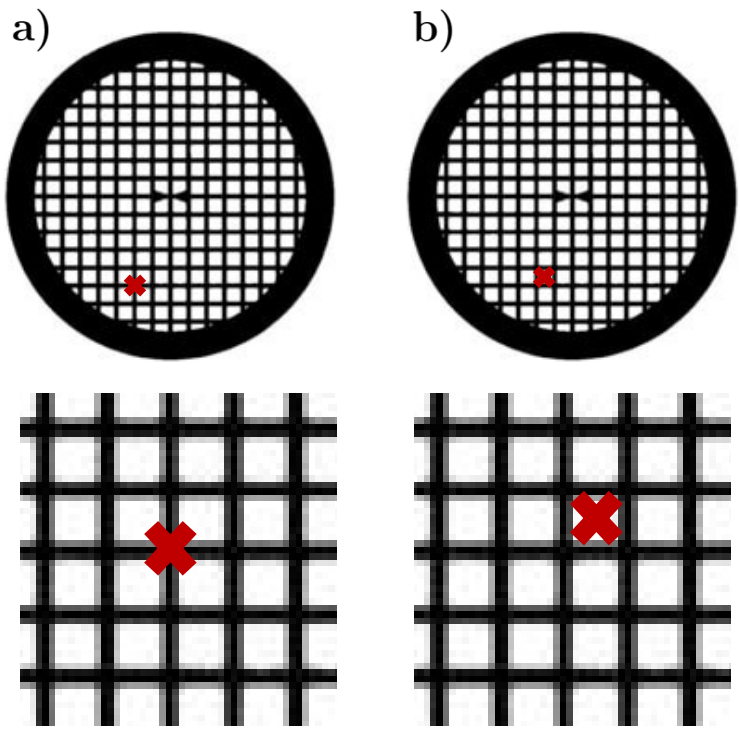

Figure 3.12: Schematic representation highlighting the areas referred to as Grid Holes (a) and Grid Intersections (b).

drift or environmental factors.

We employed the following excitation energies: 1.58 eV, 1.94 eV, 2.33 eV with the following objectives: 50× Long Working Distance and 100×. To prevent potential damage to the samples, the laser power was carefully regulated and kept below 1 mW during all measurements. It has been experimentally demonstrated that exceeding this power threshold could cause long-term damage to the TEM grid holes and to the carbon coating on the copper grid.

The Raman measurement strategy involved acquiring spectra at different points on the copper grid. In particular, the possibility to observe the laser spot on the sample, using the integrated Olympus BX34 microscope of the Horiba spectrometer, allowed the acquisition of spectra in precisely selected regions of the sample.

Different features and different ablation thresholds were observed depending on whether the Raman signal was acquired on a copper mesh intersection, or in one of the spaces of the grid, where only formvar stabilized with carbon was present. These two regions will be referred to as Grid Intersection and Grid Holes, as shown in Figure 3.12. The flexibility in controlling the laser power, achieved through remote adjustments using the Horiba LabSpec software, allowed precise management of the incident power. The change in objectives affected both the numerical aperture (NA) and the power density (irradiance) applied to the sample. With numerical apertures of 0.55 and 0.9 for the 50× and 100× objectives, respectively, the beam diameter D at the focal plane can be calculated as:

	2.33 eV	**1.94 eV**	**1.58 eV**
50× LWD (0.55)	3.358 mW/μm^2	2.101 mW/μm^2	1.542 mW/μm^2
100× (0.9)	8.991 mW/μm^2	5.626 mW/μm^2	4.129 mW/μm^2

Table 3.2: Maximum allowable irradiance for each objective and excitation energy used in Raman measurements on copper grid intersections.

$$D = 2w_0 = \frac{2\lambda}{\pi \times \mathrm{NA}},$$

where $w_0 = \frac{\lambda}{\pi \mathrm{NA}}$ is the beam waist radius and λ is the wavelength of the laser.

Knowing the beam diameter allows the calculation of the amount of power per unit area deposited onto the sample. The irradiance I (mW/μm^2) is given by

$$I = \frac{P}{\pi w_0^2},$$

where P is the laser power. The average maximum laser power output is 100 mW for 2.33 eV and 1.58 eV lasers, and 90 mW for the 1.94 eV laser. To prevent sample damage, the maximum allowable power was limited to 1 mW, which is approximately 1% of the average maximum power output when focusing on the copper grid intersections. For the grid holes, the power limit was reduced further to 0.1 mW, representing about 0.1% of the maximum power output. This careful reduction in power ensures the integrity of the sample during the Raman measurements.

From these values, Table 3.2 summarizes the maximum allowable irradiance for each objective and excitation radiation energy used for Raman measurements on the grid intersections. To obtain the maximum allowable irradiances for the grid holes, simply scale the reported values by a factor of ten.

When discussing power deposition on a material, fluence (J/cm^2) is typically used rather than irradiance (W/cm^2 = J/(s × cm^2)). To obtain the fluence, the irradiance must be multiplied by the sample's exposure time to the laser, which corresponds to the acquisition time of the measurement, *i.e.*, the interval during which a certain energy per unit area is deposited. This varies depending on the specific measurement and will be specified for each measurement described in the following.

Several signals were acquired at all three excitation energies, utilizing both the 100x and 50x LWD objectives on grid intersections and grid holes. The measurement parameters that yielded relevant results for this thesis (to be discussed in the next section) are presented below.

- Acquisition at 1.58 eV on a Grid Intersection, 100× objective, 1800 lines/mm

grating, 1% of maximum laser power, 30 seconds of acquisition time with 20 accumulations at a single point, and a spectral range from 30 to 600 cm^{-1}. For each acquisition, the fluence of the excitation radiation was 124 $mJ/\mu m^2$.

- Acquisition at 1.94 eV on a Grid Intersection, 50× LWD objective, 1800 lines/mm grating, 1% of maximum laser power, 40 seconds of acquisition time with 10 accumulations at a single point, and a spectral range from 40 to 1000 cm^{-1}. For each acquisition, the fluence of the excitation radiation was 84 $mJ/\mu m^2$.

- Acquisition at 2.33 eV on a Grid Intersection, 50× LWD objective, 600 lines/mm grating, 1% of maximum laser power, 5 seconds of acquisition time with 10 accumulations at a single point, and a spectral range from 24 to 5000 cm^{-1}. For each acquisition, the fluence of the excitation radiation was 17 $mJ/\mu m^2$.

Spectra from grid holes were also acquired but they did not yield results relevant to this thesis. Therefore, only the spectra that were subsequently analyzed are presented.

The combination of various laser sources, objectives, and the motorized sample stage enabled the probing of multiple points on the sample surface, focusing the laser on distinct areas and achieving a spectral resolution of approximately 1 cm^{-1}.

3.6 Raman Analysis & Results

As for the PL data, the Raman spectra were analysed post-measurement using Python scripts within Jupyter Notebook. The spectra were first normalized to their integrated area, followed by the subtraction of a background-like function for each trace. To achieve this, an appropriate analytical function was identified to model the background, using a fourth-order polynomial:

$$f(x) = ax^4 + bx^3 + cx^2 + dx + o$$

where a, b, c, d, and o are the fitting parameters.

Once the background correction was applied to both the sample and the empty grid spectra, the corrected empty grid signal was subtracted. This subtraction isolates the vibrational modes specifically associated with the $CsPbBr_3$ NPs.

The resulting spectra were then obtained as counts versus Raman shift. Initially expressed in cm^{-1}, the Raman shift was converted to meV using

$$E(J) = h \cdot c \cdot \Delta\nu, \tag{3.16}$$

where h is Planck's constant, 6.626×10^{-34} J·s, c is the speed of light, 2.998×10^8 m/s, and $\Delta\nu$ is the Raman shift in cm^{-1}. Therefore:

$$E(J) = (6.626 \times 10^{-34}\,\text{J·s}) \cdot (2.998 \times 10^{10}\,\text{cm/s}) \cdot \Delta\nu(\text{cm}^{-1}) = 1.986 \times 10^{-23} \cdot \Delta\nu(\text{cm}^{-1}).$$

by exploiting

$$1\,\mathrm{eV} = 1.602 \times 10^{-19}\,\mathrm{J}.$$

the following relation is obtained:

$$E(\mathrm{eV}) = \frac{1.986 \times 10^{-23}}{1.602 \times 10^{-19}} \cdot \Delta\nu(\mathrm{cm}^{-1}) = 1.2398 \times 10^{-4} \cdot \Delta\nu(\mathrm{cm}^{-1}). \tag{3.17}$$

Considering meV, the following compact formula is obtained for converting Raman shift values from cm^{-1} to energy in meV:

$$E\,(\mathrm{meV}) = 0.12398 \times \Delta\nu\,(\mathrm{cm}^{-1}). \tag{3.18}$$

The Raman analysis involved the use of the following excitation energies: 2.33 eV, 1.94 eV and 1.58 eV and objectives: 50 × LWD and 100 ×. Figure 3.13 shows the normalized Raman spectrum intensity (normalized by the integrated area of the traces) as a function of the Raman shift expressed in meV. This spectra were acquired using a 1.58 eV excitation energy and a 100× objective. MS0865, MS0864 and the empty grid are reported respectively in blue, red, and transparent grey. Two prominent features are present between 9 and 23 meV: a prominent peak around 18.5 meV and a significant contribution from diffuse scattering or copper oxide modes at the lower energy Raman shift. The observed mode at 18.5 meV corresponds to longitudinal optical (LO) phonon as reported in the literature [8, 113].

This was the only measurement that revealed the Raman signal of the perovskite $CsPbBr_3$@PPG-PEA supracrystals. Although measurements were performed using additional excitation energies at 2.33 eV and 1.94 eV, these spectra were dominated by photoluminescence tails that obscured the entire signal of the sample. Furthermore, amorphous carbon modes were observed without any Raman signal from the $CsPbBr_3$@PPG-PEA supracrystals at these excitation energies.

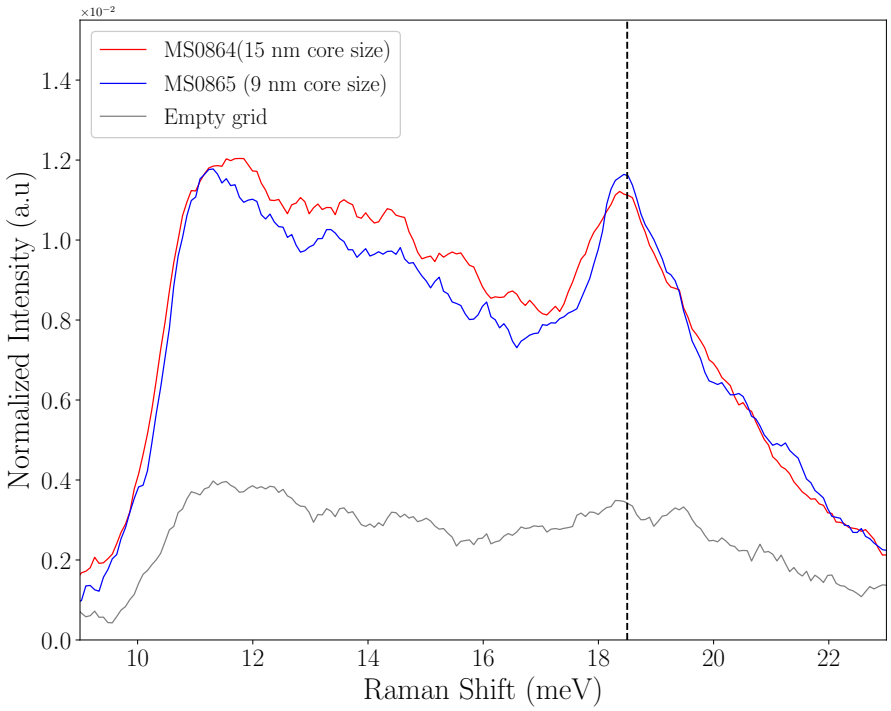

Figure 3.13: Raman spectra of MS0864 (red trace) and MS0865 (blue trace), with the contribution of the empty grid (grey) already subtracted. The intensity, normalized by the integrated area for each sample, is plotted as a function of the Raman shift (meV)

3.7 Discussion

Based on what I reported in the previous sections, I offer a possible strategy of interpretation of the experimental results.

Fluence dependence measurements, see Figure 3.2, revealed consistent linearity ranges, albeit with different slopes. The differences in the observed slopes of the minima and integrated area are mainly due to uncertainty in the selection of the scans with the highest signal-to-noise ratio. For low fluences, even small oscillations of the laser power significantly affect measurements reproducibility, complicating the acquisition of data necessary to improve the signal-to-noise ratio. Small variations in scan selection criterion affect the results, as shown by the high standard deviation and slope discrepancies, particularly for MS0864, where the signal-to-noise ratio was lower than for MS0865.

Focusing on MS0865, as shown in Figure 3.3 (b, c) and Figure 3.4 (a, c & b, d), a red-shift in the TA signal is observed when measuring the same sample on different surface spots (spot 1 and spot 2) characterized by a different heterogeneous morphological distribution at the mesoscale. In particular, the TAS signal shifts to low energies of about 60 meV when the superlattice packing increases. Other studies in the literature suggest that the transition from monolayers to multi-layered structures leads to a red-shift in the PL emission [114]. This shift occurs because increased packing reduces confinement along the direction perpendicular to the de-

position plane [114, 115]. PL red-shift due to lower confinement may also explain TA red-shift due to lower spacing between energy levels involved in the absorption mechanisms. Figure 3.14 illustrates this effect through a series of monodisperse $CsPbBr_3$ nanocubes, nanoplatelets, and nanosheets, synthesized using only oleylamine (OlAm) and oleic acid (OA) as ligands, as presented in the work by *L. Manna* [114]. Another possible explanation involves degradation and instability effects in perovskites under ultraviolet (UV) radiation and exposure to air. Previous research has shown that red-shifts in PL energy in UV-illuminated $CsPbBr_3$ NP films suggest modifications in radiative recombination pathways involving excitons and thermally activated centers [116]. *Li et al.* also demonstrated that larger NP units in $CsPbBr_3$ films exhibit less pronounced PL degradation [116].

The observed red-shift may be attributed to the combined effects of both UV illumination and air exposure, rather than UV illumination alone. In fact, the samples were exposed to air during measurements, having been removed from their nitrogen atmosphere. Air exposure has also been shown to impact the stability of $CsPbBr_3$ perovskites, as demonstrated by studies indicating the formation of trap states and photo-oxidation, which also cause red-shift and PL degradation [117]. It is important to point out that the experiments presented in this thesis were conducted by pumping at 3.02 eV, and the measurements on MS0865 spot 2 were taken last, making this dataset more susceptible to these effects. In the presented experiments, the observed red-shift can thus be attributed to a combination of confinement reduction and the effects of extended UV and air exposure.

The second main result comes from looking at the persistence of a tail of PB ($\Delta T/T > 0$) at low energies in MS0865 spot 2 (Figure 3.4 c-d). In MS0865 spot 2 the PB tail grows more prominently during the first few fs up to a maximum of 0.7 in difference transmission (Figure 3.4 c), while in MS0865 spot 1, it shows less intensity and grows up to 0.15 in difference transmission (Figure 3.4 a-b). This is possibly the first time this behaviour is seen in $CsPbBr_3$@PPG-PEA samples and it is certainly one of the starting points for further investigation on these systems.

As shown in the Figure 3.5, a, the differential absorption spectrum for a $CsPbBr_3$ films typically consists of three main features:

- A dominant positive PB signal ($\Delta T/T > 0$), possibly indicating the bleaching of band-to-band transitions caused by photocarriers filling the states at the edges of the valence and conduction bands, as reported in the literature [68, 111, 118, 119].

- A broad photoinduced absorption (PIA_1) feature ($\Delta T/T < 0$) above the bandgap, which has recently been attributed to photoinduced reflection in Lead Halide Perovskite (LHP) films, also observed in the NP samples. This probably corresponds to increased NP scattering from the photorefractive effect [118]. The difference between transient reflection and transmission spectra indicates significant photoinduced reflection changes, driven by alterations in the dielectric function, causing notable refractive index variations in high-index

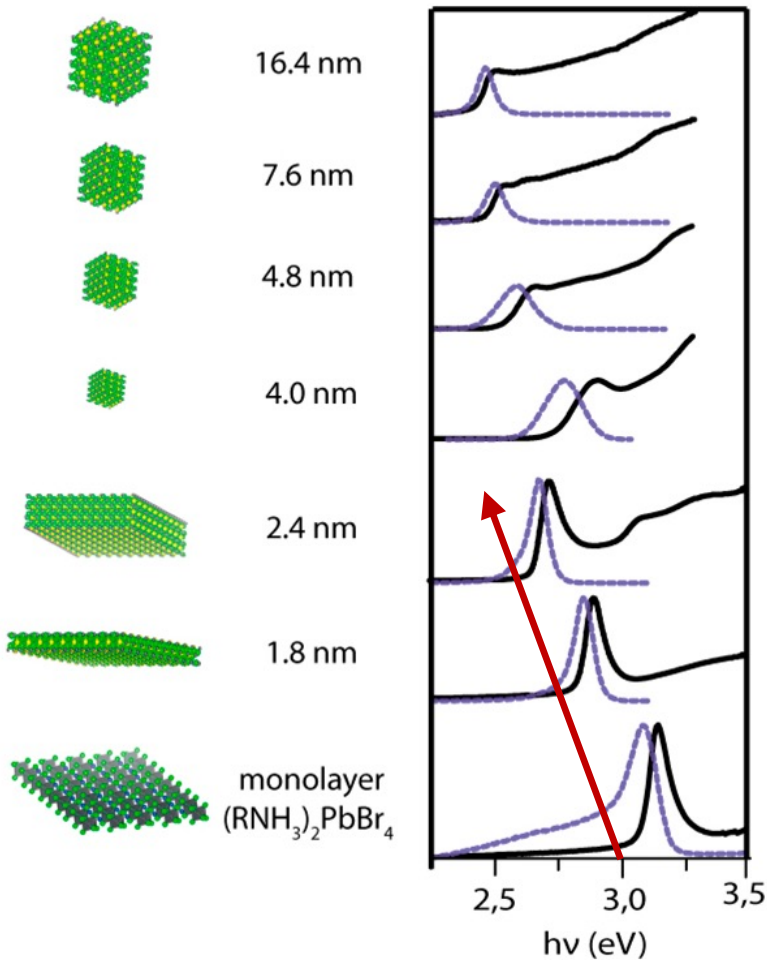

Figure 3.14: Image showing a series of monodisperse $CsPbBr_3$ nanocubes, nanoplatelets, and nanosheets, compared with a single monolayer of $(RNH_3)_2PbBr_4$ composition. The Absorbance is represented by a black solid line, and the Photoluminescence is shown as a blue dashed line in the corresponding spectra on the right. Image adapted from [114].

materials like lead halide perovskites (LHP) [118].

- A short-lived (less than 1 ps) PIA_2 feature ($\Delta T/T < 0$) at energies just below the band gap (2.3 eV - 2.38 eV). In the literature [70, 111, 118], this peak is attributed to two complementary mechanisms, illustrated in Figure 3.15. The first (Figure 3.15, a) is band gap renormalization, where high carrier densities temporarily reduce the band gap through many-body interactions, creating unoccupied states just below the ground state band gap. As hot carriers relax, these states are rapidly reoccupied. The second mechanism (Figure 3.15, b) is exciton-exciton interaction, where the presence of one exciton lowers the energy needed for the absorption of another, causing a red shift in exciton absorption energy [70].

Focusing on the spectral differences between MS0864 and MS0865, particularly on the short-lived (< 1 ps) PIA feature at energies just below the band gap (2.3eV to 2.38 eV), reveals another key finding. Looking at the spectral shapes of the $CsPbBr_3$

film (Figure 3.5, a) and MS0864 (Figure 3.5, b), an asymmetric positive-to-negative feature is observed, which should be centered at the excitonic peak energy [69]. This spectral shape is accompanied by a red-shift in the early times, consistent with the attractive interaction between excitons generated by the pump and probe beams. This phenomenon, known as the biexcitonic Stark effect, results from the Coulomb interaction of biexcitons, which, under dipole-dipole interaction, induce a Stark-like electric field that splits the energy levels like in Figure 3.15, b [69, 120, 121]. As the particle size decreases, an increase in exciton-exciton interaction due to confinement effects would be expected, yet the opposite is observed. Similarly, with a reduction in core size, band gap renormalization should increase (as calculated by Butkus *et al.* [111]), but the results show an opposite trend: this thesis highlights the absence of the PIA peak in MS0865 (smaller core size), a feature that, in contrast, is widely reported in the literature [67, 69, 111, 122]. Therefore, this phenomenon may be related to the ligand role. One qualitative explanation is that increasing NPs packing density, keeping the same ligands, could alter packing and contribute to exciton dissociation due to core size effects. Verifying this hypothesis requires further investigations.

Looking at the time constants in Table 3.1, a slower hot carrier (HC) cooling in smaller NCs can be attributed to the intrinsic hot phonon bottleneck which arises due to the limited availability of phonon modes in confined systems [5]. This effect explains the experimentally observed shorter time constants and thus faster relaxation dynamics in MS0864 (15 nm core size) with respect to MS0865 (9 nm core size) [5, 123, 124]. In general, the phonon bottleneck effect occurs when there is a mismatch between the rate at which carriers release energy and the ability of phonon modes to dissipate that energy. This effect can be viewed from two perspectives: i) In smaller NPs the limited phonon density of states (DOS) intensifies the bottleneck, trapping energy with the carriers for longer and slowing the cooling process [5, 123]. ii) In larger NPs, with a high phonons density of states, the interaction between phonons and charge carriers can lead to polaron formation [5, 68, 113, 123, 125]. In this case, the bottleneck is reinforced as polarons stabilize the carriers, further slowing the relaxation to the ground state. When the number of hot carriers increases, the polarons interact, stabilising the carriers and causing excess energy to remain trapped in the electronic states instead of dissipating in the lattice. This interaction slows the return to the fundamental state, increasing the cooling time (τ) [126]. This model has been supported by several studies on perovskite systems [64, 65, 82, 111, 127], with a particularly pronounced effect in inorganic perovskites such as $CsPbBr_3$

In this thesis, an ultrafast decay constant ($\tau_1 < 1$ ps) followed by a slower time constant has been reported. The ultrafast component is typically associated with hot carrier (HC) cooling via intraband relaxation, occurring within 1 ps due to carrier-carrier interactions and scattering. Beyond 1 ps, this mechanism fades, and a stronger bleaching signal emerges as the states fill [5, 70, 111, 122, 123, 125]. At longer times, other recombination pathways become dominant. Global lifetime analysis (GLA) provided τ_2 values of 659 ps, 456 ps, and 43 ps for MS0865 spot 1, MS0865 spot 2, and MS0864, respectively. These time constants are typically at-

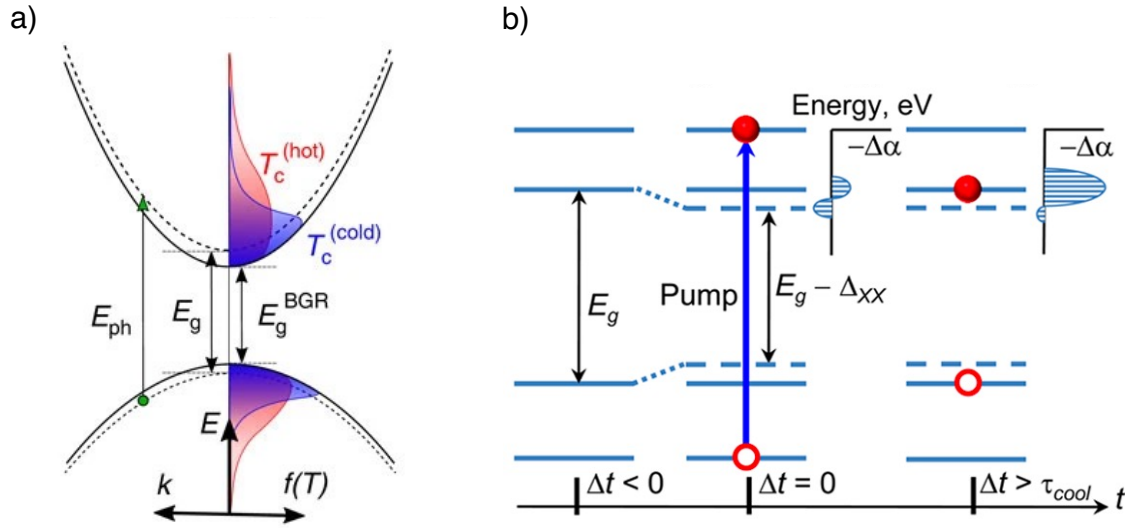

Figure 3.15: An explanation of PIA. (a) Schematic representation showing the relationship between carrier cooling and bandgap renormalization (BGR). Carriers are excited into (out of) the conduction (valence) bands and interact, leading to bandgap renormalization, which shifts the bandgap from E_g to E_g^{BGR}. "Hot" photoexcited carriers (red) with high temperatures initially occupy fewer states near the renormalized band edge, resulting in a photoinduced absorption (PIA). As the carrier temperature decreases (blue), the increased occupation of the renormalized states leads to a reduction in the PIA signal. (b) A schematic illustration of the transient absorption (TA) evolution during carrier intraband relaxation. Before excitation (left), the optical transition energies detected by the probe pulse are defined by single-exciton energies (solid lines). After a high−energy "hot" exciton is generated (middle), the transition energies "seen" by the probe pulse are modified by the exciton-exciton interaction (dashed lines). In the case of exciton-exciton attraction, the energy required to introduce a second exciton into the structure is reduced compared to that of the single exciton. This phenomenon, known as the "biexciton effect," results in a red-shift of the band-edge transition observed in early-time TA as a derivative-like feature, with photoinduced absorption (PA) at lower energy and a bleach at higher energy. As the carriers relax into the band-edge state (right), the PA feature is dominated by the bleach signal, which is due to the state-filling effect. The image in a) is adapted from Price et al. [118] and b) from Makarov et al. [70].

tributed to multi-exciton relaxation or recombination [125, 128], while other studies suggest that the second time constant (≈40 ps) may correspond to Auger recombination of multi-excitons [69, 70]. However, this statement requires further investigation into the relaxation pathways as a function of the fluence. This could motivate further studies on these samples. Although the intrinsic hot phonon bottleneck slows carrier dynamics in smaller structures, Figure 3.7 shows that the relaxation process in MS0865 (spots 1 and 2) appears to be nearly complete after 1 ns, whereas for MS0864, the dynamics remain active, as indicated by the non-zero transient absorption signal at 1 ns. Such long decay times in the literature are typically associated with single-exciton recombination [69, 124].

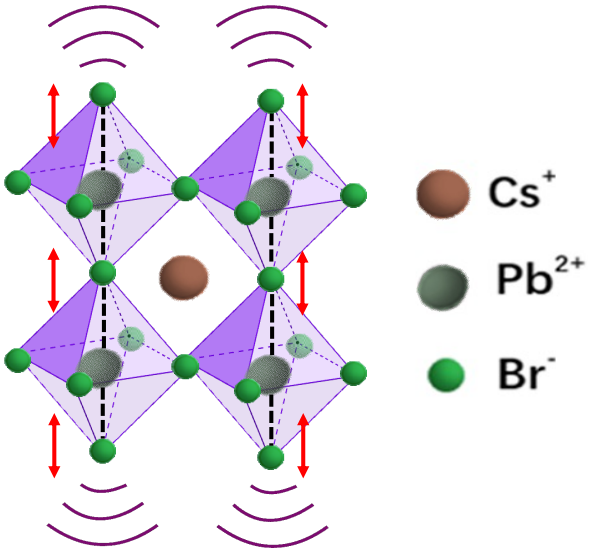

Figure 3.16: Schematic representation of the crystal structure of a $CsPbBr_3$ perovskite, illustrating the arrangement of Cs^+ (brown), Pb^{2+} (grey), and Br^- (green) ions. The purple octahedra represents the $PbBr_6$ units, with the red arrows indicating the LO vibrational mode related to the 18.5 meV Raman mode. The curved lines illustrate the vibrational waves propagating through the crystal lattice.

PL results in section 3.4 show emission energies coherent with the spectral ranges of the TAS signals, confirming the probing of the same electronic states. PL results suggest that the sample's photoluminescence emission varies with nanoparticle size, in agreement with the literature [7, 62, 114, 129, 130]. This feature could be ascribed to the effect of confinement. The energy gap ΔE for a particle in a low-dimensional semiconductor increases as the confinement length (a) decreases, following an inverse proportionality law, expressed as:

$$\Delta E \propto \frac{1}{a^2}.$$

This indicates that as the confinement length becomes smaller, the energy gap increases due to stronger confinement effects [131]. Typically, $CsPbBr_3$ NPs around 10 nm in size are in a weak confinement regime [5], since the exciton Bohr radius for $CsPbBr_3$ is smaller than 10 nm, being approximately 7 nm, as estimated within the effective mass approximation (EMA) by *Protesescu et al.* [7]. As the size decreases from 15 nm to 9 nm, approaching the exciton Bohr radius, the electron and hole wavefunctions become more confined. This leads to an increase in the confinement effect, resulting in a larger energy gap and a blue-shift in the emission spectrum [7].

The Raman results suggest the presence of a 18.5 meV mode which matches the energy of a Longitudinal Optical (LO) phonon of $CsPbBr_3$ observed in literature [8, 113]. This phonon introduces a distortion along the Pb-Br direction, elongating the octahedral structure on one side while shortening it on the other. Figure 3.16 shows a schematic representation of the longitudinal optical phonon propagating along

the Pb-Br direction. The Raman mode observed at 18.5 meV not only provides evidence for the presence of longitudinal optical phonons, but also enhances the understanding of electron-phonon interactions in perovskite nanocrystals $CsPbBr_3$. As demonstrated by *Cannelli et al.* this supports the formation of large polarons, which play a critical role in the relaxation dynamics of hot carriers [68, 92], as evidenced by the TAS results.

Together with the hot phonon bottleneck and confinement effects, these results provide a deeper understanding of the mechanisms governing carrier cooling and recombination dynamics in systems characterized by different heterogeneity at the mesoscale level and different core sizes at the single nanocrystal level. In-depth analysis of the present results is ongoing to corroborate the proposed scenario. Moreover, next planned experimental campaigns utilizing X-ray Absorption Spectroscopy and Ultrafast Imaging techniques shall provide additional insights into these processes and their influence on the performance of devices based on these materials.

Conclusions and Perspectives

The main goal of this work was to investigate how both variations in the core size of the nanoparticles and the heterogeneous morphological distribution of ligand-coated $CsPbBr_3$ nanoparticle supracrystals influence the photoinduced response of these systems. The ligand, 2-Ammonioethyl (hydroxypolypropyleneglycolyl, Mn=725) phosphate (PPG-PEA), was chosen because it not only stabilizes the perovskite core but also preserves the peculiar perovskite emissive properties [2]. Two samples with core sizes of 9 nm (MS0865) and 15 nm (MS0864) were deposited on TEM copper grids using the capillary tweezers method. TEM investigations revealed hints about the heterogeneous morphological distribution in the two samples, providing starting insights into their structural organization and packing density.

Based on these initial morphological considerations, Transient Absorption Spectroscopy (TAS) measurements were conducted using two comparative approaches:

1. Mesoscale heterogeneity dependence: same ligand, same core, different packing. In this analysis, TAS experiments were performed on two distinct surface spots of MS0865: MS0865 spot 1 and MS0865 spot 2. The key difference between them is that spot 1 has a 2D-like packing, while spot 2 exhibits a 3D-like arrangement of the supracrystal monolayer.

2. Core-size dependence: similar heterogeneity, same ligand, different core size. In this analysis, TAS experiments were conducted on two different samples: MS0864 and MS0865 spot 1. While both share the same overall heterogeneity, they differ in the core size of the individual nanoparticle units.

From the first analysis, TAS results show a red shift of $\approx$ 60 meV in the Difference Absorption (ΔA) signal by moving from spot 1 to spot 2. This reveals the impact of the heterogeneous morphological distribution and local packing on the $CsPbBr_3$@PPG-PEA photoinduced response. This result can be justified by considering the effects of confinement, which decrease when packing increases [114]. Moreover, the comparison between MS0865 spot 1 and MS0865 spot 2 revealed also the persistence of a broadband PB signal at wavelengths below the band gap in the multilayer sample. Further experiments are underway to understand this behavior.

From the second TAS analysis, a comparison between MS0865 and MS0864, supracrystals with different core sizes at the single nanoparticle level, reveals distinct

behaviors. MS0864, consistent with samples reported in the literature, exhibits an ultrafast photoinduced absorption (PIA) within the first 1 ps of pump-probe time delay, caused by exciton-exciton interactions [70]. In contrast, MS0865 does not display these features. This suggests the absence of a biexciton effect probably due to the interdigitation of ligands promoting exciton dissociation despite the higher expected binding energies.

Through TAS experiments, hot carrier relaxation mechanisms were also studied. From the time scales and relaxation pathways analysis, as the nanoparticle core decreases, from MS0864 to MS0865 (spot 1 e spot 2), the slow down of the relaxation constants can be explained in terms of the hot phonons bottleneck effect: the absence of enough phonons to balance the hot carriers slows down the relaxation dynamics [5, 123]. Moreover, two major time constants were retrieved, both triggered under optical pump excitation at 3.02 eV, but occurring on different timescales: an initial ultrafast decay (<1 ps) and a second, slower decay on longer timescales ($\approx$ 40 ps and $\approx$ 500 ps for MS0864 and MS0865, respectively). The former (τ_1) seems to be related to exciton-exciton interaction mechanisms [70]. The latter, τ_2, suggests the presence of different relaxation mechanisms in the two samples: the first might be related to exciton recombination via the Auger process [69, 70], and the second to exciton recombination or relaxation via phonon scattering at longer timescales [125]. Furthermore, different recovery mechanisms to the ground state were identified for the two samples: in both datasets of MS0865, the recovery is almost complete after 1 ns, while for MS0864, the ground-state recovery is not complete, as indicated by the presence of PB even at long times like 1 ns. This behaviour could be explained in terms of single exciton recombination [124, 125].

Photoluminescence (PL) and Raman spectroscopy techniques, provide key insights into the optical and vibrational degrees of freedom in the system. The photoluminescence emission found at 2.39 eV (15 nm core) and 2.41 eV (9 nm core) seems coherent with the spectral ranges of the TAS signals, thus suggesting the probing of the same electronic states. Moreover, the $\approx$ 16 meV blue shift in the emission suggests the presence of confinement effects, with smaller core sizes increasing the separation of energy levels [62, 132]. Raman spectroscopy identified a mode at 18.5 meV which suggests the presence of LO phonon propagating along Pb-Br directions [5, 8, 123]. This phonon is important for understanding the relaxation pathways of photoexcited carriers in those mechanisms involving the polaron formation [8, 68].

3.7.1 Perspectives

These results open several perspectives for future research:

- Further in-depth analysis as a function of fluence is needed to distinguish between Auger biexciton recombination and phonon scattering exciton relaxation or recombination;

- TAS experiments with higher signal-to-noise ratios and improved temporal resolution could provide more insight into the potential presence of coherent

responses;

- Variations in ligand size, confinement strength, and deposition methods could be explored to gain a deeper understanding of the role of heterogeneity;

- Correlative experimental strategies.

Reconnecting to the State of the Art, the initial morphological analysis of functionalized gold nanoparticle supracrystals introduced a novel approach to studying heterogeneity from a dynamic perspective. The goal was to understand how order/disorder correlations affect functional properties, such as electron-phonon coupling, using techniques like ultrafast small-angle electron diffraction. This thesis focused on transient absorption spectroscopy (TAS) as the first step in this investigation of a new class of materials, the ligand-coated $CsPbBr_3$ nanoparticle supracrystals. Future research will involve Time-Resolved X-ray Absorption and Ultrafast Imaging to further explore the role of heterogeneity in functional properties. The combination of these methods could provide a more comprehensive understanding of the electronic and structural dynamics governing the behaviour of photoexcited carriers. Time-resolved imaging techniques, such as Ultrafast Ptychography, allow direct visualization of nanoscale dynamics following early light-matter interactions [14]. These approaches are crucial for quantifying morphological heterogeneity and understanding how ligands influence the packing density that in turn affects the system's functional properties by influencing thermal and acoustic responses [11, 12]. The results of this thesis emphasise the complex interplay between ligand-ligand and ligand-core interactions, which contribute to the observed different heterogeneous morphological distributions and NP size-dependent signals. The capability to achieve a comprehensive understanding of the behaviour of photoexcited carriers in $CsPbBr_3$@PPG-PEAwould provide valuable information for the design of future devices based on these materials. The findings presented in this thesis not only contribute to a deeper understanding of $CsPbBr_3$@PPG$-$PEA materials but also try to provide a foundation for their application in various fields, ranging from optoelectronics to photovoltaics.

Bibliography

[1] Dmitri V. Talapin, Michael Engel, and Paul V. Braun. "Functional materials and devices by self-Assembly". In: *MRS Bulletin* 45.10 (2020), pp. 799–806. ISSN: 08837694. DOI: 10.1557/mrs.2020.252.

[2] Viktoriia Morad et al. "Designer phospholipid capping ligands for soft metal halide nanocrystals". In: *Nature* 626.7999 (2024), pp. 542–548. ISSN: 14764687. DOI: 10.1038/s41586-023-06932-6.

[3] Paul Alivisatos. "The use of nanocrystals in biological detection". In: *Nature biotechnology* 22.1 (2004), pp. 47–52.

[4] Jason J. Calvin et al. "Thermodynamic Investigation of Increased Luminescence in Indium Phosphide Quantum Dots by Treatment with Metal Halide Salts". In: *Journal of the American Chemical Society* 142.44 (2020), pp. 18897–18906. ISSN: 15205126. DOI: 10.1021/jacs.0c08954.

[5] Amrita Dey et al. "State of the Art and Prospects for Halide Perovskite Nanocrystals". In: *ACS Nano* 15.7 (2021), pp. 10775–10981. ISSN: 1936086X. DOI: 10.1021/acsnano.0c08903.

[6] Maksym V Kovalenko, Loredana Protesescu, and Maryna I Bodnarchuk. "Properties and potential optoelectronic applications of lead halide perovskite nanocrystals". In: *Science* 358.6364 (2017), pp. 745–750.

[7] Loredana Protesescu et al. "Nanocrystals of Cesium Lead Halide Perovskites (CsPbX3, X = Cl, Br, and I): Novel Optoelectronic Materials Showing Bright Emission with Wide Color Gamut". In: *Nano Letters* 15.6 (2015), pp. 3692–3696. ISSN: 15306992. DOI: 10.1021/nl5048779.

[8] Oliviero Cannelli et al. "Quantifying photoinduced polaronic distortions in inorganic lead halide perovskite nanocrystals". In: *Journal of the American Chemical Society* 143.24 (2021), pp. 9048–9059.

[9] Giulia Grancini et al. "Hot exciton dissociation in polymer solar cells". In: *Nature materials* 12.1 (2013), pp. 29–33.

[10] Claudio Giannetti et al. "Ultrafast optical spectroscopy of strongly correlated materials and high-temperature superconductors: a non-equilibrium approach". In: *Advances in Physics* 65.2 (2016), pp. 58–238.

[11] Giulia Fulvia Mancini et al. "Order/disorder dynamics in a dodecanethiol-capped gold nanoparticles supracrystal by small-angle ultrafast electron diffraction". In: *Nano letters* 16.4 (2016), pp. 2705–2713.

[12] Giulia Fulvia Mancini et al. “Local photo-mechanical stiffness revealed in gold nanoparticles supracrystals by ultrafast small-angle electron diffraction”. In: *Structural Dynamics* 6.2 (2019).

[13] Arne Thomas. “Functional materials: From hard to soft porous frameworks”. In: *Angewandte Chemie - International Edition* 49.45 (2010), pp. 8328–8344. ISSN: 14337851. DOI: 10.1002/anie.201000167.

[14] Robert M Karl Jr et al. “Full-field imaging of thermal and acoustic dynamics in an individual nanostructure using tabletop high harmonic beams”. In: *Science advances* 4.10 (2018), eaau4295.

[15] Michael A. Boles, Michael Engel, and Dmitri V. Talapin. “Self-assembly of colloidal nanocrystals: From intricate structures to functional materials”. In: *Chemical Reviews* 116.18 (2016), pp. 11220–11289. ISSN: 15206890. DOI: 10.1021/acs.chemrev.6b00196.

[16] Kyle J.M. Bishop et al. “Nanoscale forces and their uses in self-assembly”. In: *Small* 5.14 (2009), pp. 1600–1630. ISSN: 16136810. DOI: 10.1002/smll.200900358.

[17] Stephan Förster and Matthias Konrad. “From self-organizing polymers to nano- and biomaterials”. In: *Journal of Materials Chemistry* 13.11 (2003), pp. 2671–2688. ISSN: 09599428. DOI: 10.1039/b307512p.

[18] Hiroyasu Furukawa et al. “The chemistry and applications of metal-organic frameworks”. In: *Science* 341.6149 (2013). ISSN: 10959203. DOI: 10.1126/science.1230444.

[19] Robert J. Macfarlane et al. “Assembly and organization processes in DNA-directed colloidal crystallization”. In: *Proceedings of the National Academy of Sciences of the United States of America* 106.26 (2009), pp. 10493–10498. ISSN: 00278424. DOI: 10.1073/pnas.0900630106.

[20] Dmytro Nykypanchuk et al. “DNA-guided crystallization of colloidal nanoparticles”. In: *Nature* 451.7178 (2008), pp. 549–552. ISSN: 14764687. DOI: 10.1038/nature06560.

[21] Ashish A. Kulkarni et al. “Archimedean lattices emerge in template-directed eutectic solidification”. In: *Nature* 577.7790 (2020), pp. 355–358. ISSN: 14764687. DOI: 10.1038/s41586-019-1893-9. URL: http://dx.doi.org/10.1038/s41586-019-1893-9.

[22] Yiyong Mai and Adi Eisenberg. “Self-assembly of block copolymers”. In: *Chemical Society Reviews* 41.18 (2012), pp. 5969–5985. ISSN: 14604744. DOI: 10.1039/c2cs35115c.

[23] Fan Hong et al. *DNA Origami: Scaffolds for Creating Higher Order Structures*. Vol. 117. 20. 2017, pp. 12584–12640. ISBN: 1258412640. DOI: 10.1021/acs.chemrev.6b00825.

[24] Paul W.K. Rothemund. “Folding DNA to create nanoscale shapes and patterns”. In: *Nature* 440.7082 (2006), pp. 297–302. ISSN: 00280836. DOI: 10.1038/nature04586.

[25] Jason J. Calvin, Amanda S. Brewer, and A. Paul Alivisatos. “The role of organic ligand shell structures in colloidal nanocrystal synthesis”. In: *Nature Synthesis* 1.2 (2022), pp. 127–137. ISSN: 27310582. DOI: 10.1038/s44160-022-00025-4.

[26] Michael A Boles et al. “The surface science of nanocrystals”. In: *Nature Materials* 15.3 (2016), p. 364. ISSN: 14764660. DOI: 10.1038/nmat4578.

[27] Hyeonjun Lee et al. “Ligands as a universal molecular toolkit in synthesis and assembly of semiconductor nanocrystals”. In: *Chemical Science* 11.9 (2020), pp. 2318–2329. ISSN: 20416539. DOI: 10.1039/c9sc05200c.

[28] Emily a Weiss. “the Growth , Surface Structure , and Redox”. In: *Accounts of chemical research* XXX.Xx (2013), p. x.

[29] Yongwook Kim et al. “Bright and Uniform Green Light Emitting InP/ZnSe/ZnS Quantum Dots for Wide Color Gamut Displays”. In: *ACS Applied Nano Materials* 2.3 (2019), pp. 1496–1504. ISSN: 25740970. DOI: 10.1021/acsanm.8b02063.

[30] Yu Ho Won et al. “Highly efficient and stable InP/ZnSe/ZnS quantum dot light-emitting diodes”. In: *Nature* 575.7784 (2019), pp. 634–638. ISSN: 14764687. DOI: 10.1038/s41586-019-1771-5. URL: http://dx.doi.org/10.1038/s41586-019-1771-5.

[31] 2 Abhishek Swarnkar, 1 et al. “that generally depends on the asperity size and stress drop and on the resistance of the matrix. This effective radius R”. In: *Science* 354.6308 (2016), pp. 92–96.

[32] Woon Seok Yang et al. “Iodide management in formamidinium-lead-halide-based perovskite layers for efficient solar cells”. In: *Science* 356.6345 (2017), pp. 1376–1379. ISSN: 10959203. DOI: 10.1126/science.aan2301.

[33] Alexander L. Efros and David J. Nesbitt. “Origin and control of blinking in quantum dots”. In: *Nature Nanotechnology* 11.8 (2016), pp. 661–671. ISSN: 17483395. DOI: 10.1038/nnano.2016.140.

[34] Gangcheng Yuan et al. “Two Mechanisms Determine Quantum Dot Blinking”. In: *ACS Nano* 12.4 (2018), pp. 3397–3405. ISSN: 1936086X. DOI: 10.1021/acsnano.7b09052.

[35] Zhaochuan Fan and Michael Grünwald. “Orientational Order in Self-Assembled Nanocrystal Superlattices”. In: *Journal of the American Chemical Society* 141.5 (2019), pp. 1980–1988. ISSN: 15205126. DOI: 10.1021/jacs.8b10752.

[36] Justin C. Ondry et al. “Colloidal Synthesis Path to 2D Crystalline Quantum Dot Superlattices”. In: *ACS Nano* 15.2 (2021), pp. 2251–2262. ISSN: 1936086X. DOI: 10.1021/acsnano.0c07202.

[37] Kim De Nolf et al. “Controlling the size of hot injection made nanocrystals by manipulating the diffusion coefficient of the solute”. In: *Journal of the American Chemical Society* 137.7 (2015), pp. 2495–2505. ISSN: 15205126. DOI: 10.1021/ja509941g.

[38] Aizhao Pan et al. “Insight into the Ligand-Mediated Synthesis of Colloidal CsPbBr3 Perovskite Nanocrystals: The Role of Organic Acid, Base, and Cesium Precursors”. In: *ACS Nano* 10.8 (2016), pp. 7943–7954. ISSN: 1936086X. DOI: 10.1021/acsnano.6b03863.

[39] Michael A. Boles and Dmitri V. Talapin. “Many-Body Effects in Nanocrystal Superlattices: Departure from Sphere Packing Explains Stability of Binary Phases”. In: *Journal of the American Chemical Society* 137.13 (2015), pp. 4494–4502. ISSN: 15205126. DOI: 10.1021/jacs.5b00839.

[40] Zewei Quan et al. “Energy landscape of self-assembled superlattices of PbSe nanocrystals”. In: *Proceedings of the National Academy of Sciences of the United States of America* 111.25 (2014), pp. 9054–9057. ISSN: 10916490. DOI: 10.1073/pnas.1408835111.

[41] A. Antanovich et al. “A strain-induced exciton transition energy shift in CdSe nanoplatelets: The impact of an organic ligand shell”. In: *Nanoscale* 9.45 (2017), pp. 18042–18053. ISSN: 20403372. DOI: 10.1039/c7nr05065h.

[42] Junsang Cho et al. “Influence of ligand shell ordering on dimensional confinement of cesium lead bromide (CsPbBr3) perovskite nanoplatelets”. In: *Journal of Materials Chemistry C* 5.34 (2017), pp. 8810–8818. ISSN: 20507526. DOI: 10.1039/c7tc02194a.

[43] Kira E. Hughes et al. “Effects of Surface Chemistry on the Photophysics of Colloidal InP Nanocrystals”. In: *ACS Nano* 13.12 (2019), pp. 14198–14207. ISSN: 1936086X. DOI: 10.1021/acsnano.9b07027.

[44] David P. Nenon et al. “Design Principles for Trap-Free CsPbX 3 Nanocrystals: Enumerating and Eliminating Surface Halide Vacancies with Softer Lewis Bases”. In: *Journal of the American Chemical Society* 140.50 (2018), pp. 17760–17772. ISSN: 15205126. DOI: 10.1021/jacs.8b11035.

[45] Jakob C. Dahl et al. “Elucidating the Weakly Reversible Cs-Pb-Br Perovskite Nanocrystal Reaction Network with High-Throughput Maps and Transformations”. In: *Journal of the American Chemical Society* 142.27 (2020), pp. 11915–11926. ISSN: 15205126. DOI: 10.1021/jacs.0c04997.

[46] Justin C Ondry et al. “Colloidal synthesis path to 2D crystalline quantum dot superlattices”. In: *ACS nano* 15.2 (2020), pp. 2251–2262.

[47] Jianbo Gao et al. “Ultrahigh hot carrier transient photocurrent in nanocrystal arrays by Auger recombination”. In: *Nano letters* 19.7 (2019), pp. 4804–4810.

[48] Jin Young Kim et al. “Two-dimensional nanoparticle supracrystals: a model system for two-dimensional melting”. In: *Nano letters* 16.2 (2016), pp. 1352–1358.

[49] Franziska Krieg et al. “Colloidal CsPbX3 (X = Cl, Br, I) Nanocrystals 2.0: Zwitterionic Capping Ligands for Improved Durability and Stability”. In: *ACS Energy Letters* 3.3 (2018), pp. 641–646. ISSN: 23808195. DOI: 10.1021/acsenergylett.8b00035.

[50] Franziska Krieg et al. “Stable ultraconcentrated and ultradilute colloids of CsPbX3 (X = Cl, Br) nanocrystals using natural lecithin as a capping ligand”. In: *Journal of the American Chemical Society* 141.50 (2019), pp. 19839–19849. ISSN: 15205126. DOI: 10.1021/jacs.9b09969.

[51] Franziska Krieg et al. “Monodisperse Long-Chain Sulfobetaine-Capped CsPbBr3 Nanocrystals and Their Superfluorescent Assemblies”. In: *ACS Central Science* 7.1 (2021), pp. 135–144. ISSN: 23747951. DOI: 10.1021/acscentsci.0c01153.

[52] Von H L Wells. “Uber die Casium-und Kalium-Blei halogenide”. In: *Zeitschrift für anorganische und allgemeine Chemie* 3 (1827), pp. 195–210.

[53] W A Wooster and CHR KN M. “Crystal Structure and Photoconductivity of Caesium Plumbohalides Nuclear Magnetic Resonance in ˜-Brass”. In: *Proc. Arner. Acad* 93.1955 (1936), p. 131.

[54] Shunsuke Hirotsu et al. *Hirotsu1974.Pdf*. 1974. URL: http://journals.jps.jp/doi/abs/10.1143/JPSJ.37.1393.

[55] T. Lanigan-Atkins et al. "Two-dimensional overdamped fluctuations of the soft perovskite lattice in CsPbBr3". In: *Nature Materials* 20.7 (2021), pp. 977–983. ISSN: 14764660. DOI: 10.1038/s41563-021-00947-y.

[56] Akihiro Kojima et al. "Organometal halide perovskites as visible-light sensitizers for photovoltaic cells". In: *Journal of the american chemical society* 131.17 (2009), pp. 6050–6051.

[57] Joseph S Manser, Jeffrey A Christians, and Prashant V Kamat. "Intriguing optoelectronic properties of metal halide perovskites". In: *Chemical reviews* 116.21 (2016), pp. 12956–13008.

[58] Samuel D Stranks et al. "Electron-hole diffusion lengths exceeding 1 micrometer in an organometal trihalide perovskite absorber". In: *Science* 342.6156 (2013), pp. 341–344.

[59] T Umebayashi et al. "Electronic structures of lead iodide based low-dimensional crystals". In: *Physical Review B* 67.15 (2003), p. 155405.

[60] Michael A Becker et al. "Bright triplet excitons in caesium lead halide perovskites". In: *Nature* 553.7687 (2018), pp. 189–193.

[61] Dane W de Quilettes et al. "Impact of microstructure on local carrier lifetime in perovskite solar cells". In: *Science* 348.6235 (2015), pp. 683–686.

[62] Silvia G Motti et al. "CsPbBr3 nanocrystal films: Deviations from bulk vibrational and optoelectronic properties". In: *Advanced Functional Materials* 30.19 (2020), p. 1909904.

[63] Anirban Dutta et al. "Near-unity photoluminescence quantum efficiency for all CsPbX3 (X= Cl, Br, and I) perovskite nanocrystals: a generic synthesis approach". In: *Angewandte Chemie International Edition* 58.17 (2019), pp. 5552–5556.

[64] Ye Yang et al. "Observation of a hot-phonon bottleneck in lead-iodide perovskites". In: *Nature Photonics* 10.1 (2016), pp. 53–59. ISSN: 17494893. DOI: 10.1038/nphoton.2015.213.

[65] Jianhui Fu et al. "Hot carrier cooling mechanisms in halide perovskites". In: *Nature communications* 8.1 (2017), pp. 1–9.

[66] Mingjie Li et al. "Slow cooling and highly efficient extraction of hot carriers in colloidal perovskite nanocrystals". In: *Nature Communications* 8 (2017). URL: https://api.semanticscholar.org/CorpusID:1535796.

[67] Navendu Mondal and Anunay Samanta. "Complete ultrafast charge carrier dynamics in photo-excited all-inorganic perovskite nanocrystals (CsPbX3)". In: *Nanoscale* 9.5 (2017), pp. 1878–1885. ISSN: 20403372. DOI: 10.1039/c6nr09422h.

[68] Kiyoshi Miyata et al. "Large polarons in lead halide perovskites". In: *Science advances* 3.8 (2017), e1701217.

[69] J. Aneesh et al. "Ultrafast Exciton Dynamics in Colloidal CsPbBr3 Perovskite Nanocrystals: Biexciton Effect and Auger Recombination". In: *Journal of Physical Chemistry C* 121.8 (2017), pp. 4734–4739. ISSN: 19327455. DOI: 10.1021/acs.jpcc.7b00762.

[70] Nikolay S. Makarov et al. "Spectral and Dynamical Properties of Single Excitons, Biexcitons, and Trions in Cesium-Lead-Halide Perovskite Quantum Dots". In: *Nano Letters* 16.4 (2016), pp. 2349–2362. ISSN: 15306992. DOI: 10.1021/acs.nanolett.5b05077.

[71] Verena A Hintermayr et al. "Accelerated carrier relaxation through reduced coulomb screening in two-dimensional halide perovskite nanoplatelets". In: *ACS nano* 12.10 (2018), pp. 10151–10158.

[72] Junsheng Chen et al. "Cation-dependent hot carrier cooling in halide perovskite nanocrystals". In: *Journal of the American Chemical Society* 141.8 (2019), pp. 3532–3540.

[73] Jun Yin et al. "Tuning hot carrier cooling dynamics by dielectric confinement in two-dimensional hybrid perovskite crystals". In: *ACS nano* 13.11 (2019), pp. 12621–12629.

[74] Gurpreet Kaur et al. "Polaron-mediated slow carrier cooling in a type-1 3D/0D CsPbBr3@ Cs4PbBr6 core–shell perovskite system". In: *The Journal of Physical Chemistry Letters* 10.18 (2019), pp. 5302–5311.

[75] Riley E Brandt et al. "Searching for defect-tolerant photovoltaic materials: combined theoretical and experimental screening". In: *Chemistry of Materials* 29.11 (2017), pp. 4667–4674.

[76] Dane W Dequilettes et al. "Charge-carrier recombination in halide perovskites: Focus review". In: *Chemical reviews* 119.20 (2019), pp. 11007–11019.

[77] Sudipta Seth et al. "Tackling the defects, stability, and photoluminescence of CsPbX3 perovskite nanocrystals". In: *ACS Energy Letters* 4.7 (2019), pp. 1610–1618.

[78] Junzhi Ye et al. "Defect passivation in lead-halide perovskite nanocrystals and thin films: toward efficient LEDs and solar cells". In: *Angewandte Chemie* 133.40 (2021), pp. 21804–21828.

[79] David P Nenon et al. "Design principles for trap-free CsPbX3 nanocrystals: enumerating and eliminating surface halide vacancies with softer Lewis bases". In: *Journal of the American Chemical Society* 140.50 (2018), pp. 17760–17772.

[80] Tyler JS Evans et al. "Competition between hot-electron cooling and large polaron screening in CsPbBr3 perovskite single crystals". In: *The Journal of Physical Chemistry C* 122.25 (2018), pp. 13724–13730.

[81] Hélène Seiler et al. "Two-dimensional electronic spectroscopy reveals liquid-like lineshape dynamics in CsPbI3 perovskite nanocrystals". In: *Nature communications* 10.1 (2019), p. 4962.

[82] Giovanni Batignani et al. "Probing femtosecond lattice displacement upon photo-carrier generation in lead halide perovskite". In: *Nature communications* 9.1 (2018), p. 1971.

[83] Wei Zhao et al. "Coherent exciton-phonon coupling in perovskite semiconductor nanocrystals studied by two-dimensional electronic spectroscopy". In: *Applied Physics Letters* 115.24 (2019).

[84] Nuri Yazdani et al. "Coupling to octahedral tilts in halide perovskite nanocrystals induces phonon-mediated attractive interactions between excitons". In: *Nature Physics* 20.1 (2024), pp. 47–53.

[85] Benjamin Abécassis. "Three-dimensional self assembly of semiconducting colloidal nanocrystals: from fundamental forces to collective optical properties". In: *ChemPhysChem* 17.5 (2016), pp. 618–631.

[86] Dmitry Baranov et al. "Investigation into the photoluminescence red shift in cesium lead bromide nanocrystal superlattices". In: *The journal of physical chemistry letters* 10.3 (2019), pp. 655–660.

[87] Gabriele Rainò et al. "Superfluorescence from lead halide perovskite quantum dot superlattices". In: *Nature* 563.7733 (2018), pp. 671–675. ISSN: 14764687. DOI: 10.1038/s41586-018-0683-0. arXiv: 1804.01873. URL: http://dx.doi.org/10.1038/s41586-018-0683-0.

[88] Yu Tong et al. "Spontaneous Self-Assembly of Perovskite Nanocrystals into Electronically Coupled Supercrystals: Toward Filling the Green Gap". In: *Advanced Materials* 30.29 (2018), pp. 1–7. ISSN: 15214095. DOI: 10.1002/adma.201801117.

[89] Chun Zhou et al. "Cooperative excitonic quantum ensemble in perovskite-assembly superlattice microcavities". In: *Nature Communications* 11.1 (2020), p. 329.

[90] David Vila-Liarte et al. "Templated-Assembly of CsPbBr3 Perovskite Nanocrystals into 2D Photonic Supercrystals with Amplified Spontaneous Emission". In: *Angewandte Chemie International Edition* 59.40 (2020), pp. 17750–17756.

[91] Rohit P Prasankumar and Antoinette J Taylor. *Optical techniques for solid-state materials characterization*. CRC press, 2016.

[92] Oliviero Cannelli. *Photo-and thermally-induced electronic and structural dynamics in perovskites and transition metal oxides*. Tech. rep. EPFL, 2021.

[93] Andreas Mann et al. "Probing the coupling between a doublon excitation and the charge-density wave in TaS 2 by ultrafast optical spectroscopy". In: *Physical Review B* 94.11 (2016), p. 115122.

[94] Fabio Novelli et al. "Witnessing the formation and relaxation of dressed quasi-particles in a strongly correlated electron system". In: *Nature communications* 5.1 (2014), p. 5112.

[95] Edoardo Baldini. *Nonequilibrium dynamics of collective excitations in quantum materials*. Springer, 2018.

[96] Daniele Fausti et al. "Light-induced superconductivity in a stripe-ordered cuprate". In: *science* 331.6014 (2011), pp. 189–191.

[97] Matteo Mitrano et al. "Possible light-induced superconductivity in K3C60 at high temperature". In: *Nature* 530.7591 (2016), pp. 461–464.

[98] Jagdeep Shah. *Ultrafast spectroscopy of semiconductors and semiconductor nanostructures*. Vol. 115. Springer Science & Business Media, 2013.

[99] Peter T Landsberg. *Recombination in semiconductors*. Cambridge University Press, 2003.

[100] GC Cho, W Kütt, and H Kurz. "Subpicosecond time-resolved coherent-phonon oscillations in GaAs". In: *Physical review letters* 65.6 (1990), p. 764.

[101] Filippo Glerean et al. "Quantum model for impulsive stimulated Raman scattering". In: *Journal of Physics B: Atomic, Molecular and Optical Physics* 52.14 (2019), p. 145502.

[102] R Merlin. "Generating coherent THz phonons with light pulses". In: *Solid state communications* 102.2-3 (1997), pp. 207–220.

[103] Cristian Manzoni and Giulio Cerullo. "Design criteria for ultrafast optical parametric amplifiers". In: *Journal of Optics* 18.10 (2016), p. 103501.

[104] Simone Restelli et al. "Studio delle proprietà funzionali di nanoparticelle e film sottili di ossidi con struttura spinello tramite tecniche statiche e time-resolved". In: (2024).

[105] Ursula Keller and R Paschotta. *Ultrafast lasers*. Springer, 2021.

[106] Eric Jones, Travis Oliphant, Pearu Peterson, et al. "SciPy: Open source scientific tools for Python". In: (2001).

[107] Chavdar Slavov, Helvi Hartmann, and Josef Wachtveitl. "Implementation and evaluation of data analysis strategies for time-resolved optical spectroscopy". In: *Analytical chemistry* 87.4 (2015), pp. 2328–2336.

[108] Ivo HM van Stokkum, Delmar S Larsen, and Rienk Van Grondelle. "Global and target analysis of time-resolved spectra". In: *Biochimica et Biophysica Acta (BBA)-Bioenergetics* 1657.2-3 (2004), pp. 82–104.

[109] Fredric J Harris. "On the use of windows for harmonic analysis with the discrete Fourier transform". In: *Proceedings of the IEEE* 66.1 (1978), pp. 51–83.

[110] Julius O Smith. *Mathematics of the discrete Fourier transform (DFT): with audio applications*. Julius Smith, 2007.

[111] Justinas Butkus et al. "The Evolution of Quantum Confinement in CsPbBr3 Perovskite Nanocrystals". In: *Chemistry of Materials* 29.8 (2017), pp. 3644–3652. ISSN: 15205002. DOI: 10.1021/acs.chemmater.7b00478.

[112] Vikash Kumar Ravi et al. "Excellent green but less impressive blue luminescence from CsPbBr3 perovskite nanocubes and nanoplatelets". In: *Nanotechnology* 27.32 (2016), p. 325708.

[113] Xiangzhou Lao et al. "Anomalous temperature-dependent exciton–phonon coupling in cesium lead bromide perovskite nanosheets". In: *The Journal of Physical Chemistry C* 123.8 (2019), pp. 5128–5135.

[114] Guilherme Almeida et al. "Role of acid–base equilibria in the size, shape, and phase control of cesium lead bromide nanocrystals". In: *ACS nano* 12.2 (2018), pp. 1704–1711.

[115] Violette Steinmetz et al. "Anisotropic shape of CsPbBr 3 colloidal nanocrystals: from 1D to 2D confinement effects". In: *Nanoscale* 12.36 (2020), pp. 18978–18986.

[116] Ji Li et al. "Ultraviolet light induced degradation of luminescence in CsPbBr3 perovskite nanocrystals". In: *Materials Research Bulletin* 102.February (2018), pp. 86–91. ISSN: 00255408. DOI: 10.1016/j.materresbull.2018.02.021.

[117] Vandana Nagal et al. " CsPbBr 3 Nanoplatelets: Synthesis and Understanding of Ultraviolet Light-Induced Structural Phase Change and Luminescence Degradation ". In: *ECS Journal of Solid State Science and Technology* 10.9 (2021), p. 096002. ISSN: 2162-8769. DOI: 10.1149/2162-8777/ac2078.

[118] Michael B Price et al. "Hot-carrier cooling and photoinduced refractive index changes in organic–inorganic lead halide perovskites". In: *Nature communications* 6.1 (2015), p. 8420.

[119] Joseph S Manser and Prashant V Kamat. "Band filling with free charge carriers in organometal halide perovskites". In: *Nature Photonics* 8.9 (2014), pp. 737–743.

[120] Patanjali Kambhampati. "Hot exciton relaxation dynamics in semiconductor quantum dots: radiationless transitions on the nanoscale". In: *The Journal of Physical Chemistry C* 115.45 (2011), pp. 22089–22109.

[121] Patanjali Kambhampati. "Unraveling the structure and dynamics of excitons in semiconductor quantum dots". In: *Accounts of chemical research* 44.1 (2011), pp. 1–13.

[122] Chengqiang Wang et al. "Ultrafast transient absorption spectroscopy of 14 and 2.1 nm CsPbBr3 nanoparticles: Free carrier vs exciton". In: *Applied Physics Letters* 124.8 (2024). ISSN: 00036951. DOI: 10.1063/5.0187197.

[123] Mingjie Li et al. "Slow hot-carrier cooling in halide perovskites: prospects for hot-carrier solar cells". In: *Advanced Materials* 31.47 (2019), p. 1802486.

[124] Anirban Mondal et al. "Ultrafast exciton many-body interactions and hot-phonon bottleneck in colloidal cesium lead halide perovskite nanocrystals". In: *Physical Review B* 98.11 (2018), p. 115418.

[125] Matthew N. Ashner et al. "Size-dependent biexciton spectrum in cspbbr3 perovskite nanocrystals". In: *ACS Energy Letters* 4.11 (2019), pp. 2639–2645. ISSN: 23808195. DOI: 10.1021/acsenergylett.9b02041.

[126] Thomas R Hopper et al. "Ultrafast intraband spectroscopy of hot-carrier cooling in lead-halide perovskites". In: *ACS energy letters* 3.9 (2018), pp. 2199–2205.

[127] Jianfeng Yang et al. "Acoustic-optical phonon up-conversion and hot-phonon bottleneck in lead-halide perovskites". In: *Nature communications* 8.1 (2017), p. 14120.

[128] Navendu Mondal and Anunay Samanta. "Complete ultrafast charge carrier dynamics in photo-excited all-inorganic perovskite nanocrystals (CsPbX3)". In: *Nanoscale* 9.5 (2017), pp. 1878–1885. ISSN: 20403372. DOI: 10.1039/c6nr09422h.

[129] Michael C Brennan, Jessica Zinna, and Masaru Kuno. "Existence of a size-dependent Stokes shift in CsPbBr3 perovskite nanocrystals". In: *ACS Energy Letters* 2.7 (2017), pp. 1487–1488.

[130] Jinjin Wang et al. "Photo-Physical Properties of CsPbBr3 Nanocrystals Adjusted by a Weak Quantum Confinement Effect". In: *The Journal of Physical Chemistry C* 127.27 (2023), pp. 13081–13087.

[131] John H Davies. *The physics of low-dimensional semiconductors: an introduction*. Cambridge university press, 1998.

[132] Loredana Protesescu et al. "Monodisperse Formamidinium Lead Bromide Nanocrystals with Bright and Stable Green Photoluminescence". In: *Journal of the American Chemical Society* 138.43 (2016), pp. 14202–14205. ISSN: 15205126. DOI: 10.1021/jacs.6b08900.

Acknowledgements

To conclude this work, I would like to take a moment to express my gratitude to all the people who have been with me along the way.
First, my deepest thanks go to my supervisor, Prof. Giulia Fulvia Mancini, for providing me with the opportunity to grow both personally and professionally. Her guidance, the opportunities she offered, and her professionalism have opened new perspectives in my life. I am especially grateful to her for granting me access to the instrumentation and facilitating collaborations between the Department of Physics, the Department of Physical Chemistry, and ETH Zurich for the sample provisions.
I would also like to extend my sincere thanks to Dr. Simone Restelli for his close supervision throughout this journey. His efforts to share his wealth of knowledge and experience contributed significantly to my growth. With his friendliness and patience, I never felt alone in my research journey.
I am also grateful to those who supported me in the lab work: Dr. Fabiola Faini and Dr. Benedetta Albini, whose help was crucial. Special thanks also go to the members of the LUXEM team: Nicola, Claudia, Domenico, and Carmelo, with whom it is a pleasure to share the research spaces. I am thankful for the kindness, patience, and constant availability they have with me. I really appreciate it.
I would also like to thank Gabriele Giunta and Claudio Scagliotti for creating the custom-made mechanical components, such as the sample holder and sample chamber, which were essential for my experiments.
Furthermore, I extend my gratitude to all my friends and colleagues in the Department of Physics. Every moment we spend together is a source of motivation.
On a personal note, I would like to thank my parents for their constant support, even from a distance. I know I am always in your thoughts. Finally, I would like to thank Alessia for still being here, by my side, "*mignolo nel mignolo*".

Pavia, 18 October 2024
A.E. Mazzarone